BIOCORROSION OF 1018 STEEL IN SULFIDE RICH MARINE ENVIRONMENTS; A CORRELATION BETWEEN STRAIN AND CORROSION USING ELECTRON BACKSCATTER DIFFRACTION

by

Joshua Daniel Martin

A thesis submitted in partial fulfillment
of the requirements for the degree

of

Master of Science

in

Chemical Engineering

MONTANA STATE UNIVERSITY
Bozeman, Montana

May, 2014

©COPYRIGHT

by

Joshua Daniel Martin

2014

All Rights Reserved

TABLE OF CONTENTS

TABLE OF CONTENTS CONTINUED

TABLE OF CONTENTS CONTINUED

LIST OF TABLES

Figure Page

LIST OF FIGURES

Figure Page

LIST OF FIGURES CONTINUED

Figure Page

LIST OF FIGURES CONTINUED

Figure Page

LIST OF FIGURES CONTINUED

Figure Page

LIST OF FIGURES CONTINUED

Figure Page

LIST OF FIGURES CONTINUED

Figure Page

LIST OF FIGURES CONTINUED

Figure Page

LIST OF FIGURES CONTINUED

Figure Page

LIST OF FIGURES CONTINUED

Figure Page

LIST OF FIGURES CONTINUED

Figure Page

LIST OF FIGURES CONTINUED

Figure Page

ABSTRACT

Microbially induced corrosion (MIC) of steel due to the presence of sulfide is a leading cause of pit formation of carbon steel in fuel-seawater environments. While extensively studied, the exact causes of pitting corrosion in naval fuel tanks when exposed to MIC in the presence of fuel and seawater are not completely understood. This thesis focuses on the role that cold-rolling of carbon steel plays on corrosion while subjected to sulfidogenic, suboxic corrosive environments. Particularly, the effects of microscopic residual strain found within 1018 steel on the anodic dissolution of the metal is studied in different MIC sulfide environments using EBSD, AFM, FE-SEM, EDX, and electrochemistry. It is found that regions of increased plastic deformation of the crystalline lattice as a result of cold rolling correlate to an increase in anodic dissolution rates of 1018 steel coupons cut parallel to rolling direction. Image overlay provides a verification of the location of corrosion of samples to the same locations found in EBSD mapping taken prior to corrosion, ensuring the predictive value of EBSD analysis in establishing locations of accelerated corrosion. The effect of different corrosion environments on the corrosion rate of steel is measured through electrochemistry. Values obtained through these measurements are applied using mechanochemical theories to predict the localized dissolution rate of the steel due to strain using computational methods. Mechanochemical analysis of the strained areas results in predicted corrosion rates within an order of magnitude of the corrosion rates measured using AFM for the exposed time period at the same locations. Areas exhibiting increased corrosion rates occur in areas exhibiting increased strain as measured by EBSD analysis. Further electrochemical results show an increase in corrosion rates for suboxic sulfide rich systems containing low levels of oxygen, when compared to anaerobic sulfide environments. Variations in corrosion current density as a function of oxygen presence, as measured by electrochemistry, accurately predict variations in mechanochemical corrosion rates of strained areas well within an order of magnitude. Results from this study support the use of EBSD as a means to further the understanding of pitting corrosion as a function of material properties.

INTRODUCTION

Background and Motivation

The anaerobic corrosion of steel by microorganisms has been a key topic in corrosion research for several decades[1], and is of particular importance in systems involving the interaction of petroleum based fuels and steel exposed to marine environments. Some of the most common examples of this type of corrosion include the corrosion of steel tanks filled with fuel and seawater while acting as ballast on naval fuel ships[2, 3] as well as the corrosion of steel pipelines used for oil transport[4]. The primary motivation for this project is a result of the costly maintenance and repair required to prevent corrosion of fuel tanks on naval ships. Funding provided by the Office of Naval Research's MURI program has linked several universities together to study the fundamental processes involved in the corrosion of steel in fuel seawater environments including the physical, chemical, and biological nature of the corrosion processes occurring within these fuel tanks.

Fundamental Corrosion Concepts

The corrosion of steel in an anaerobic electrolytic environment occurs by a series of oxidation-reduction, also known as redox, reactions at the surface of the steel as well as in the aqueous electrolytic environment. For corrosion to occur there needs to be an electron donor as well as an electron acceptor to facilitate the flow of electrons required to cause the redox reactions to proceed. Corrosion proceeds through both

electrochemical and chemical reactions in the presence of a corroding surface. Electrochemical reactions include half-cell reactions involving (1) oxidation reactions, also known as anodic reactions, and (2) complimentary reduction reactions, also known as cathodic reactions. An example of an anodic reaction is the dissolution of metal ions resulting in excess electron on the corroding metal, while during cathodic reactions these excess electrons are taken across the double layer formed on the corroding metal by cathodic reactants including dissolved oxygen and H^+ ions. Furthermore, dissolved anions and cations located in the electrolyte react among themselves to produce corrosion products that become deposited on the surface of the corroding material. This deposition leaves behind an assortment of compounds on the surface of the material as evidence of the corrosion process. Identification of these compounds, together with the *in-situ* electrochemical measurements, gives clues about the electrochemical reactions that took place during corrosion. Sometimes this process occurs between two different types of metal, a type of corrosion termed galvanic corrosion. During galvanic corrosion one of the types of metal acts as the electron donor (anode) while the other metal acts as the electron acceptor (cathode)[5]. Corrosion can also occur on the same piece of metal, where one portion of the metal acts as an anode, while another acts as a cathode. During electrochemical corrosion of steel the iron atoms can dissolve from the surface of the steel into the surrounding solution, thus making the iron act as the anode. The dissolved iron ions (cations) in the aqueous environment can also deposit on the surface of the steel after combining with other ions (anions), such as sulfide and

hydroxide ions, leaving behind solid deposits. The anodic dissolution of a metal is characterized by the general reaction mechanism given as[6]

Eqn. 1 $M_{(solid)} \rightarrow n e^- + M^{n+}_{(aq)}$

where M represents an atom of the metal undergoing corrosion, and *n* represents the number of electrons left behind on the surface during the oxidation part of the redox reaction. In the case of iron corrosion, under standard thermodynamical conditions the anodic produces a double layer potential (E^o) measured relative to the standard hydrogen electrode (SHE) of the reaction is given as[7]

Eqn. 2 $Fe_{(solid)} \rightarrow 2e^- + Fe^{2+}_{(aq)}$ $E^o = 0.44$ Volts.

The cathodic reaction occurs on the surface of the corroding metal and involves transport of electrons across the double layer potential on the metal surface, which eventually results in deposition of a metal oxide, or metal sulfide compounds as a result of the chemical reactions taking place in the liquid. The nature of these compounds depends on whether or not the system is aerobic or anaerobic. In the absence of oxygen in an aqueous solution, the cathodic reaction is

Eqn. 3 $2H^+_{(aq)} + 2e^- \rightarrow H_{2(gas)}$ $E^o = 0$ Volts

which gives the overall oxidation-reduction reaction as

Eqn. 4 $2H^+_{(aq)} + Fe_{(s)} \rightarrow Fe^{2+} + H_{2(gas)}$.

The presence of microbes has deleterious effects on corrosion known as microbially induced corrosion (MIC), which in some cases contributes to the anaerobic corrosion of steel. The anaerobic corrosion of steel due to the presence of sulfate

reducing bacteria (SRB) is a common form of anaerobic MIC, and it is a complex process that has been shown to proceed by varying mechanisms dependent on the chemical makeup of the corrosive solution[8]. Despite the different specific mechanisms of anaerobic corrosive systems involving SRB, the most important component of this type of MIC is the reduction of sulfate to sulfide. Experiments previously performed show that a strong influence of sulfide produced by SRB act as the key agent in iron attack in marine environments[8-9]. A sequence of reactions has been developed from experiments involving the cathodic depolarization during the biocorrosion of steel by SRB where sulfur acts as the anaerobic electron carrier[10,11]. The end result of the oxidation-reduction reactions is the formation of iron sulfide (FeS) on the surface of the steel due to the dissolution of elemental iron (Fe) from the steel to form divalent iron (Fe^{2+}) and the combination of this divalent iron with aqueous sulfide (S^{2-}) from the solution.

Sulfate reduction by the *Desulfovibrio* class of bacteria often occurs through a two-step process[12], by which sulfate is first activated by ATP to form adenosine phosphosulphate (APS), which is reduced to sulfite, and then to sulfide. The net reaction for all processes involved is shown below, and the corrosion potential for the entire process is around E^o=-0.700 $Volts_{(SCE)}$ [13] or E^o=-0.459 $Volts_{(SHE)}$), and the overall reaction equation becomes[14].

Eqn. 5 $4Fe+SO_4^{2-}+4H_2O \rightarrow FeS + 3Fe^{2+} + 8OH^-$ E^o=-0.459 $Volts_{(SHE)}$

Pitting of the steel is a common result of SRB induced corrosion. A general understanding of the mechanisms by which pitting occurs on the surface of steel during

corrosion has come from studies focused largely on the chemical makeup of impurities found in the steel. For example, experiments have shown that pit initiation occurs in the steel located directly adjacent to manganese sulfide (MnS) inclusions[15]. Analysis of corrosion that has been induced in steel due to the presence of MnS for different types of steels has been employed by means of general electrochemistry[15], scanning vibrating electrode technique (SVET)[16], and scanning Auger microscope (SAM)[17]. Other investigations have shown that nonspecific pitting correlates to grain orientation[18], while increased grain boundary attack has been shown to correlate to increased misorientation of the iron lattice at those boundaries[19]. These experiments support the idea that the material properties of the steel help to govern the anodic dissolution of the steel during corrosion.

Electrochemistry

The use of electrochemical techniques gives quantifiable data regarding the chemical processes taking place during exposure of steel in a corrosive environment. The principles of electrochemistry are based upon fundamental thermodynamic concepts that were developed in the second half of the 1800's, and are still valid in the evaluation of corrosion processes today[4,20]. Perhaps the most important equation developed for the analysis of electrochemical processes is the Nernst equation, which was developed through rearrangement of thermodynamic Gibbs free energy relations as demonstrated here for an isobaric, isothermal electrochemical cell.[7]

Beginning with Gibbs free energy:

Eqn. 6 $$\Delta G = \sum \nu_i \mu_i = -n_e F E$$

and

Eqn. 7 $$\mu_i = \mu_i{}^o + RT \ln a_i$$

Where ΔG is the change in Gibbs free energy, ν_i is the molar stoichiometric multiplier, $\mu_i$is the chemical potential of component i, F is Faraday's constant (96,486 C mol^{-1}), $n_e$is the number of electrons being transferred in the reaction, *E* is the electrode potential (volts), R is the universal gas constant (8.314 Joule $mol^{-1}K^{-1}$), and T is absolute temperature (Kelvin). In all the equations listed, the standard state of a function is denoted by the superscript ^{o}, which were obtained at T=298K. Thus a change in Gibbs free energy is given by,

Eqn. 8 $$\Delta G - \Delta G^o = \sum \nu_i (\mu_i - \mu_i{}^o) = RT \sum \nu_i (ln\ a_i)_i$$

where a_i represents concentration of component i. Substitution for $\Delta G - \Delta G^o$ from the first equation, and rearrangement for E yields;

Eqn. 9 $$E = E^o - \frac{RT}{nF} \ln(\prod a_i{}^{\nu_i})$$

which further translates to the most common form of the Nernst Equation used in electrochemical corrosion[5, 20].

Eqn. 10- Nernst Equation: $$E = E^o - \frac{RT}{nF} \log\left[\frac{[Ox]}{[Red]}\right]$$

From the Nernst equation, the potential of an electrode due to aqueous metal ion concentration is given as:

Eqn. 11 $$E = E^o + \frac{RT}{nF} \log[M^{n+}]$$

At thermodynamic equilibrium, all of the electrochemical redox reactions that take place on the surface of the corroding metal, and hence all of the potentials (E) involved in the anodic and cathodic processes approach the same value by adjusting the dissolved ions in the solution. These adjustments often involve the change in concentration of the metal (M^{n+}) cation as well as through changes in pH of the solution. This common potential is sometimes referred to as the open circuit potential. One of the electrochemical techniques commonly used to acquire values of E for an electrochemical system is through the measurement of open circuit potentials of an electrochemical cell.

The equations listed above allow for not only a quantitative analysis of the electrochemical system, but they also provide information of *in-situ* development of the electrochemical process during corrosion. Observation of open circuit potentials provides information about the change in electrode potential in the system. Utilizing iron as the metal being observed in **Eq.11** gives the following simplified equation for the electrochemical system monitored in the experiments of this project:

Eq.12 $$E = E^{o}{}_{Fe/Fe^{2+}} - \frac{RT}{nF}\log\,[Fe^{2+}]$$

In these equations $[Fe^{2+}]$ represents the molar concentrations of Fe^{2+} ions. By using the standard potential of iron oxidation (i.e. $2e^{-} + Fe^{2+}{}_{(aq)} \rightarrow Fe$), E^{o} =-0.44 Volts, and substituting for the constants R,T,n, and F, **Eq.12** becomes;

Eq.13 $$E = -0.44 + 0.0296 * \log\,[Fe^{2+}]$$

where a given increase in Fe^{2+} concentration would thus lead to an increase in the electrode potential of the system. Using similar thermodynamic analysis for H^+ and dissolved O_2 reductions, the governing equations for the two reactions become:

for hydrogen

Eq.14 $$E = -0.0296 * \log\left[pH_{2\,gas}\right] - 0.0591 * pH$$

and for oxygen

Eq.15 $$E = 1.229 + 0.0148 * \log\left[pO_{2\,gas}\right] - 0.0591 * pH$$

where pH_2 and pO_2 refer to the partial pressure of H_2 and O_2 molecules in gas phase in thermodynamical equilibrium with their dissolved species in the aqueous medium (i.e. pH_2=1 means one atmosphere of hydrogen gas). For example, at ambient conditions pO_2~1/5 which is equivalent to ~8.5 mg per liter dissolved oxygen in the aqueous phase. A very important result comes from analysis of these equations, particularly the equation concerning oxygen, **Eq.15** in that a very small concentration of trace amount of O_2 contributes greatly in changing the open circuit potential. These equations are very sensitive to subtle changes in either potential, or concentration. In general it is safe to say that these equations are very sensitive to subtle changes in concentration. For example, if a system is initially purely anaerobic and a small amount of oxygen is added to that system, the deviation from the original potential of the electrode increases substantially. To further illustrate this, calculations show that in order to have our resting potential of -0.44 V the thermodynamic equations require dissolved oxygen concentrations of much less than 1 part per trillionth. This level of O_2 concentration is

not measureable with current sensor technologies, but its effect is easily measured by the standard electrochemical techniques. This is one of the reasons to use electrochemical measurements to describe some of the experiments performed in this project.

The information from these equations also becomes useful in understanding the corrosion processes which take place during the exposure period through the analysis of open-circuit potentials. Corrosion deposits can be inferred from the open circuit potentials of the experiment through use of Pourbaix diagrams[21]. These diagrams show the relationship between pH and electrode potential of a system. The lines of the plots, much like those shown on many phase diagrams, are developed by plotting the equilibrium potential of two phases of a system, as a function of pH. For the purpose of this study, the use of the equations given above were used to create a Pourbaix diagram for a system that could theoretically contain Fe, Fe^{2+}, Fe^{3+}, and only some of the many forms of FeS including Mackinawite and Greigite (see appendix Figure 1). An understanding of these diagrams gives a better knowledge of the likely corrosion deposits that will form on the surface of the metal during the corrosion process. This is important in this project due to the possibly passivating effect that certain iron sulfides tend to have when formed on the surface of the steel, and more importantly the inhibiting effect (preventing ion and electron transfer across the protective layer) they can have on the corrosion rate of the steel coupon.

Corrosion currents and rates are calculated from electrochemical data through the utilization of electrochemical potential values, and resistivity values obtained from polarization resistance measurements. The governing equation used for these calculations has a form similar to the Arrhenius equation that is more commonly used in chemical kinetics. The following corresponding equation is known as the Butler-Volmer equation and is given below[10].

Eqn. 16 Butler-Volmer Equation: $i = i_o(e^{\frac{\Delta\varphi}{\alpha}} - e^{-\frac{\Delta\varphi}{\beta}})$

where $\Delta\varphi$ the overpotential which is equal to the change in electrode potential (E) from its equilibrium value (i.e. open circuit potential). The i_o refers to the corrosion current density, α and β are given by $\alpha = \frac{RT}{\gamma nF}$ and $\beta = \frac{RT}{\acute{\gamma} nF}$ where γ and γ′ are called electron transfer coefficients for anodic and cathodic processes, respectively, which in practice vary from 0.3 to 0.7, the rest of the parameters are known constants in that R is the gas constant, T is the absolute temperature, n is the number of electrons transferred per reaction (in our case n=2), and F is the Faraday constant. Therefore, in practice, the α and β need to be determined experimentally, their values vary in mV between 18 mV α (or β) < 43 mV. Below we give a method of determining their value under limited conditions which, however, does apply in this work. The Butler-Volmer equation (Equation 16) has two components which can be written as $i = i_a - i_c$ where i_a is called anodic current density and is given by

Eqn. 17 $i_a = i_o e^{\frac{\Delta\varphi}{\alpha}}$

and i_c is the corresponding cathodic corrosion rate given by,

Eqn. 18 $$i_c = i_o e^{-\frac{\Delta\varphi}{\beta}}$$

However, conventionally these components are written as $i_a = i_o 10^{\frac{\Delta\varphi}{b_a}}$ and $i_c = i_o 10^{-\frac{\Delta\varphi}{b_c}}$ the total current density measured becomes

Eqn. 18' $i = i_a - i_c = i_o(10^{\frac{\Delta\varphi}{b_a}} - 10^{-\frac{\Delta\varphi}{b_c}})$ where

$b_a = 2.303\alpha$ and $b_c = 2.303\beta$ where 2.303=Ln10. The values of b_a and b_c for n=2 varies from 40 mV to 100 mV due to uncertainties in the charge transfer coefficients γ and γ'.

The corrosion rate at equilibrium is determined by the corrosion current density i_o , however, it is not trivial to determine this value accurately without the knowledge of b_a and b_c. This is typically done by finding accurately the intersections of the slopes in Log *i* vs $\Delta\varphi$ plots of anodic and cathodic Tafel plots when the $\Delta\varphi$ values are comparable to or greater than b_a and b_c values which are typically of the orders of ~100 mV. However, in our measurements the current vs. $\Delta\varphi$ deviate from Equation 18' at around 10-15 mV due to limitations imposed on the current from the diffusion dominated ion transfers across the double layer potential on the surface hence exponential dependence does not apply. In this work determination of corrosion rates utilize the polarization resistivity, R , which can be determined from the linear variation of the current vs. $\Delta\varphi$ in the range -5mV< $\Delta\varphi$ <5mV. This is because when $\Delta\varphi \ll \alpha$ and β the equation can be expanded into a Taylor's series of first order and current then becomes

Eqn 19. $$i \cong i_o\left(1+\frac{\Delta\varphi}{\alpha}-1+\frac{\Delta\varphi}{\beta}\right)=i_o\left(\frac{\alpha+\beta}{\alpha\beta}\right)\Delta\varphi=\frac{\Delta\varphi}{R}$$

where R is given by

Eqn 20. $$R=\frac{1}{i_o}\,\frac{\alpha\beta}{\alpha+\beta}=\frac{1}{i_o}\,\frac{b_a b_c}{2.303\,(b_a+b_c)}$$

where we used $b_a = 2.303\alpha$ and $b_c = 2.303\beta$ relationships. Because of the linear relation $\Delta\varphi \cong R\ i$ it is trivial to determine the polarization resistivity R from the slope of the $\Delta\varphi$ vs. i measurement near the origin (near $\Delta\varphi \approx 0$) hence from Equation 20 we can determine the corrosion current densityi_o. However, as mentioned above the uncertainties in the charge transfer coefficient we decided to use the average value[10] that is often used γ=γ′=0.5 [22,23] ; this immediately yields $b_a = b_c = 0.059$ Volts, a value that was used to determine the corrosion current density hence the corrosion rates via.

Eqn 21. $$i_o=\frac{1.28\times10^{-2}}{R}$$

where resistivity is given in Ohm-cm^2 the current density is given in Amp/cm^2. The values for $i_o$obtained this way are accurate to within ~25% of the correct value. It is trivial to obtain the corrosion rates once the value for i_o is determined. Remember the current is nothing but charge flowing from the metal per unit time (C/s). Also we know that for every 2e (or 2x1.6x10^{-19} Coulomb) of charge one Fe^{2+} is removed from the clean Fe surface and deposited as sulfide or oxide on the surface. The corrosion rate τ of Fe can then be determined simply by

Eqn 22.

$$\tau=\frac{i_o\,M_{Fe}}{2\,e\,\rho}=3.68\times10^{-5}\,i_o\,\left({}^{cm}/_{s}\right)=1.16\times10^{4}\,i_o\,\left({}^{mm}/_{year}\right)$$

where M_{Fe}=9.30x10^{-23} g (Atomic mass of Fe), e=1.6x10^{-19} C (electron charge), r=7.87 g/cm^3 (the density of Fe), i_o is the corrosion current density (in A/cm^2) determined from Equation 22. As one can see for the corrosion current density of $i_o = 10^{-6}\, {}^{A}/_{cm^2} = 1\ \mu A/cm^2$ the corrosion rate is about 1.16x10^{-2} mm/year. Typically corrosion rates 0.2 mm/year and more would be considered serious.

Mechanochemistry

T.P. Hoar was one of the first to theorize the interdependence of the dissolution of a material based on the "mechanically induced movement of the surface metal atoms[24]" through experimentation. A term which he went on to define as the mechano-chemical effect was coined to describe this process. This term was later shortened to mechanochemical in the literature[25] and will be used here to describe this type of phenomena. Hoar later went on to lay the ground work for demonstrating the possibility of this type of chemical process using austenitic stainless steels[26], and from this work developed a working theory for the propagation of stress corrosion cracking of these steels in the presence of chloride solutions at elevated temperatures through anodic dissolution of the steel due to mechanochemical induced effects.

In the late 1960's E.M. Gutman furthered the theory established by Hoar by developing the thermodynamic equations relating to this type of anodic dissolution[27]. Building on the experimental work performed by other groups at the time[28 29], Gutman demonstrated that there exists a relationship between plastic strain and density of mobile dislocations of a material given by the equation

Eqn. 23 $N=\alpha(\varepsilon-\varepsilon_0)=\alpha\Delta\varepsilon$

where N is the density of mobile dislocations, α is a constant, ε is the plastic strain, and ε_0 is the strain amount that corresponds to the elastic limit. The constant α varies from material to material, and is used to describe the mobile dislocation density as a function of strain. Based on empirical results this value is often on the order of magnitude of $10^{11}cm^{-1}$ for elements such as nickel and iron[30]. For this study, α will be equal to $1.6*10^{11}$ cm^{-1}, which has been used for steel in similar studies[31]. Using the assumption of constant stress (τ) and constant temperature, an approximation of the chemical potential μ is given by

Eqn. 24 $\mu=\tau\frac{1}{\alpha}$

which most importantly gives the correlation that as stress applied to a material increases, the chemical potential of that material increases as well. The regulatory factor which establishes the amount of increase in chemical potential is governed by the constant α. Further analysis of this equation brings to attention the fact that, under isobaric and isothermal conditions, the chemical potential μ is in fact the Gibbs free energy of the system.

The importance of these concepts becomes apparent when considering both the macroscopic stresses acting upon a metal pipe carrying a pressurized fluid capable of corroding the steel, as well as on the microscopic scale when considering the various strains induced upon individual grains of a metal due metallurgical processing of the metal, this strain is called *residual strain* (to differentiate it from the strain due to

external stress). The concept of stress corrosion cracking due to grain properties of the steel has been experimentally demonstrated[32], with the ultimate conclusion that grain texture has a major effect on the ability of a pipeline to corrode. Experiments performed by other groups have also found a correlation for the increased corrosion rate found at the tip of a crack due to the proposed stress at the propagating crack tip [33,34]; which was explained through various types of computer modelling and finite-element analysis. The accelerated anodic dissolution rate due to the measured localized iron lattice strain of 1018 steel using EBSD analysis for high strained areas has not yet been demonstrated in environments containing sulfate reducing bacteria. The primary focus of this project was to demonstrate the relationship of anodic dissolution at locations of high residual strain (increased plastic deformation) in 1018 steel generated during its metallurgical preparation by exposing the metal to various corrosive microbial environments. The areas that were strained will be identified by means of EBSD and will be marked on the polished clean surface in order to locate them after coupons were exposed to corrosive environments. These areas, then, will be imaged by atomic and electron microscopy to assess the differential corrosion processes.

MATERIALS AND METHODS

Metal

The material investigated was industry standard AISI 1018 steel that has been cold rolled during post processing. Two types of square steel coupons of dimension 1.25 cm by 1.25 cm by 1 mm were analyzed. The first type had been cut in the direction perpendicular to the cold-rolling direction, and the other type had been cut parallel to

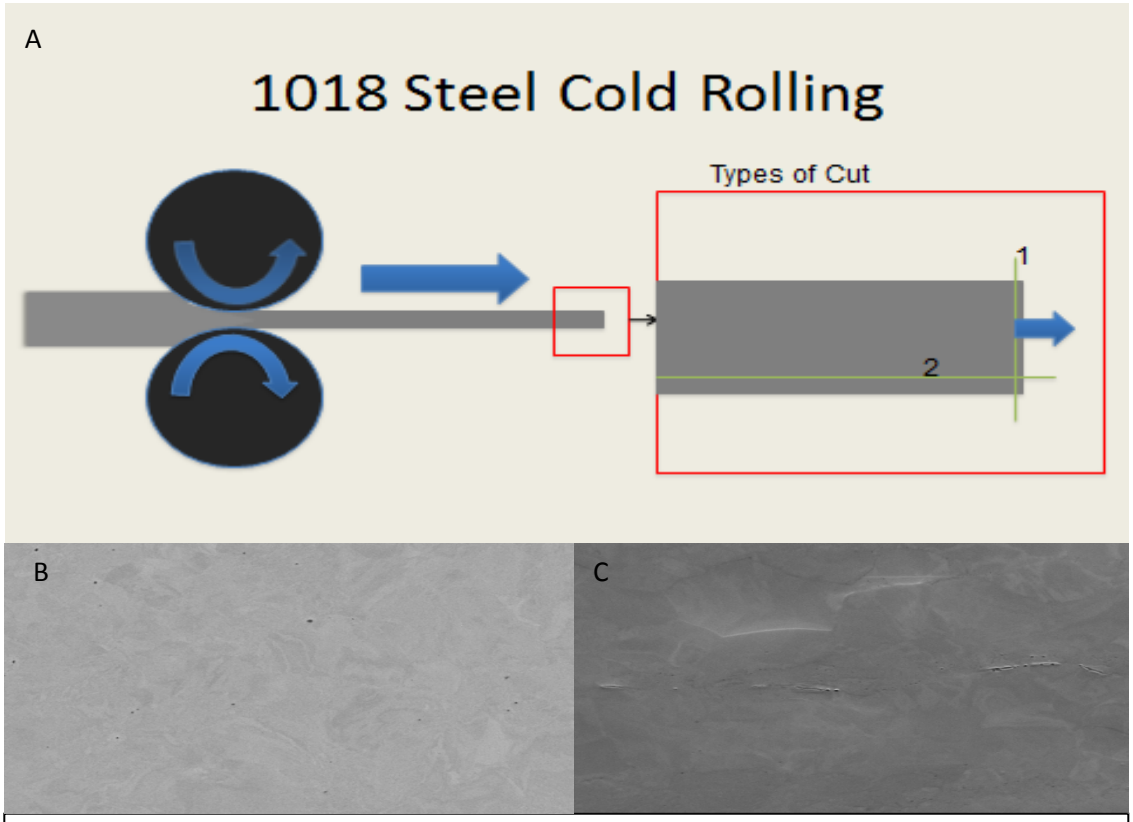

Figure 1. A) Illustration of cutting and polishing direction of the carbon steel rod in relation to cold-rolling direction of steel. The number panel A1 shows a perpendicular cut, and the panel A2 shows a parallel cut. B) An image of a polished perpendicular cut coupon surface. C) An image of a polished parallel cut coupon surface.

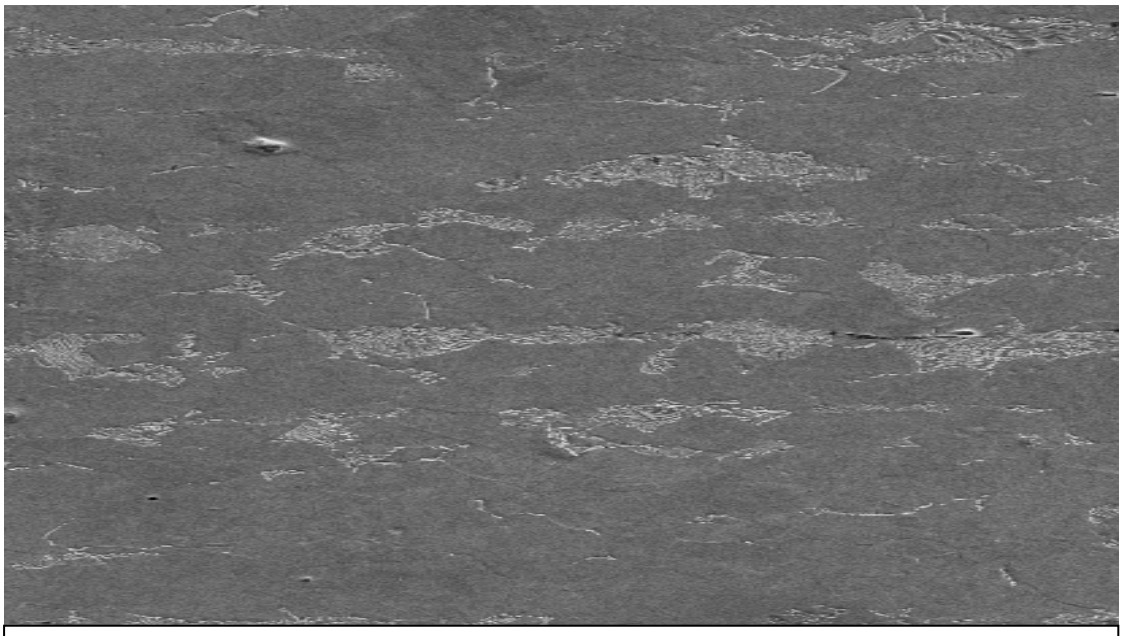

Figure 2. FEM image of a 1018 steel coupon cut and polished parallel to rolling direction after corrosion. Note the presence of elongated pearlite banding (light colored) that runs horizontally from the left side to the right side of the image.

rolling direction as shown in Figure 1. The structural differences that are of primary concern between the two orientations are the shape and orientation of inclusions within the bulk metal, and the shape and orientation of the pearlite phase. The FE-SEM image shown in Figure 2 illustrates the elongated shape of the pearlite phases as a result of the rolling process on a coupon cut parallel to the rolling direction.

X-Ray Florescence

The chemical makeup of the steel was further analyzed using x-ray florescence (XRF) to verify the elements present in the material. Ten coupons of each orientation were measured, and the averaged values were calculated and entered into Table 1.

	Al	Bal	Si	S	Cr	Mn	Fe	Ni	Cu
Round	0.8202	4.031	1.45	0.033	0.047	0.753	92.97	0.04	0.114
Perpendicular	0.8583	4.223	1.09	0.091	0.14	0.784	92.16	0.13	0.215
Parallel	0.8959	4.263	1.13	0.09	0.157	0.788	91.95	0.13	0.224

Table 1. Chemical analysis of polished coupons: Round coupon is also a perpendicular cut, and the mean weight percent of each entry shows the weight % of that element.

The Al and Si entries may have contributions from the polishing agents used in polishing the coupons. Round coupons were a different stock of 1018 steel purchased separate from the square coupons.

Naval Fuels

As part of current governmental agreements and ordinances, the US Navy is currently set to increase the amount of biofuels used in their fleet in the future. An understanding of fouling biofuels and their effects on corrosion, compared to the already used hydrocarbons, is required prior to full-scale use of these biofuels in active military ships. Four different fuels provided by the US Navy were used as hydrocarbon sources for experiments related to the use of fuel tanks as ballast tanks on naval ships. These four fuels are: JP5, JP5-Camelina and F76, and Fischer-Trope F76 (which will be referred to as FT-F76). Both JP5 and JP5-Camelina have potential correlations to jet fuels used by the Navy, while F76 and FT-F76 are more readily used as marine diesel fuel. JP5 is a known fuel for use in many jets, particularly in the US navy. JP5-Camelina is a biodiesel currently being developed from the seeds of the Camelina plant. Exact formulas for some of these fuels was unknown to our research due to the confidentiality

needed by the US Navy, however JP5 and JP5-Camelina are known to be hydrocarbons of lower carbon content similar to other gasoline, while F76 and FTF-76 are higher carbon hydrocarbons most similar to diesel motor fuels.

Analytical Methods Overview

To reinforce the fundamental ideas formulated for this project, a series of analytical methods were used to determine the effects of strain on the corrosion rate of steel. A general flow of how the analysis of the coupons and their corrosive environment was performed is shown in Figure 3. The analyzed coupon is exposed to a corrosive environment where we were able to measure the oxygen concentration of the fluid as a function of depth. The use of scanning electron microscopy was then used to

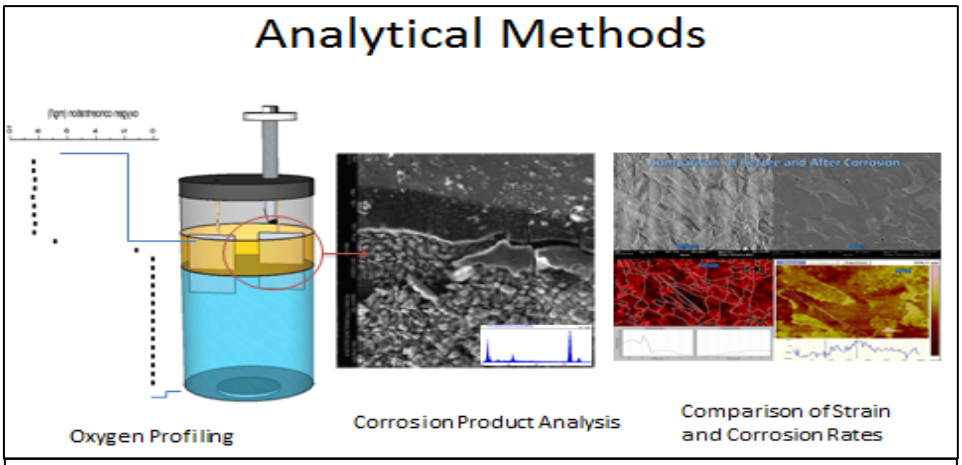

Figure 3. Illustration of the primary analytical processes utilized including A) Oxygen Measurements, B) FE-SEM imaging and chemical analysis, and C) Comparison of FE-SEM imagery, EBSD structure analysis, and AFM surface analysis of the sample.

image the samples, as well as obtain chemical data about the corrosion products deposited on the surface. The coupon was then stripped of its corrosion deposits, and a final analysis could then be performed which compared the effects of corrosion at the same location that was previously imaged before the sample was exposed to the corrosive environment, which enabled us to compare the same location before and after corrosion.

Electron Backscatter Diffraction

Background and History

Electron backscatter diffraction (EBSD) was first discovered in the late 1920's by Kikuchi, while studying the results of tilting a piece of mica while it is exposed to an incident electron beam [35]. The resultant bands that are formed upon an electron detector due to the diffraction of electrons from the surface of the material were termed Kikuchi bands, and are the fundamental information needed to obtain crystalline orientation information and phase identification by means of Electron Backscatter Diffraction (EBSD). The process initially involved manually analyzing each Kikuchi pattern by hand, and making further calculations about the material from each individual pattern. Automatic Kikuchi detection software now enables the analysis of Kikuchi patterns at extremely fast rates (in terms of milliseconds per pattern), enabling users to analyze larger areas of material in less amount of time.

Kikuchi Pattern Analysis

The fundamental theories and calculations for establishing crystalline lattice orientation take advantage of a Hough transformation and the Bragg condition. The use of a Hough transformation enables the analysis of a Kikuchi pattern by means of line detection within the pattern given as a result of the diffracting patterns displayed on a 2 dimensional charge-coupled detector (CCD) surface. The equation used to perform a Hough transform

Eqn. 25 $$\rho = x_i \mathrm{Cos}\Theta_j + y_i \mathrm{Sin}\Theta_j$$

transforms the information from the image space in Cartesian coordinates (x,y), to Hough space in polar coordinates (ρ, Θ). By doing so, all lines in Cartesian space are translated into polar curves which intersect at distinct points when transformed into Hough space. The end result is a plot of points in Hough space rather than lines given in Cartesian space.

The Bragg condition occurs when incident electrons interact within a crystalline sample and then scatter in a way that is characteristic to the crystallographic planes described using Miller Notation[36]. This condition is given by the Bragg's Law

Eqn. 26 $$2d \sin\Theta = n\lambda$$

where n is an integer (1, 2, 3...) that gives the diffraction order, λ is the wavelength of the incident high energy electron (~ 20 keV), d is the interplanar spacing for the lattice, and Θ is the Bragg angle of diffraction (angle between the crystal plane and incident electron).

In order to utilize Bragg's law, each individual band of a Kikuchi pattern must be interpreted using a Hough Transform, and indexed using Bragg's Law. The indexing of all angles of the pattern gives rise to the orientation of the lattice at that point. An image of the number of line calculations required to obtain orientation information from a single Kikuchi pattern is shown in Figure 4. The Kikuchi pattern shown on the left has been indexed and the resulting pattern is shown on the right. Bragg's law is used to calculate each set of Miller indices given in Figure 4B from the Kikuchi pattern shown in Figure 4A, depending on line thickness, and angle. Fortunately, in the late 1980's automatic pattern detection software was developed to enable analysis of larger areas of interest within a material in an efficient time frame.

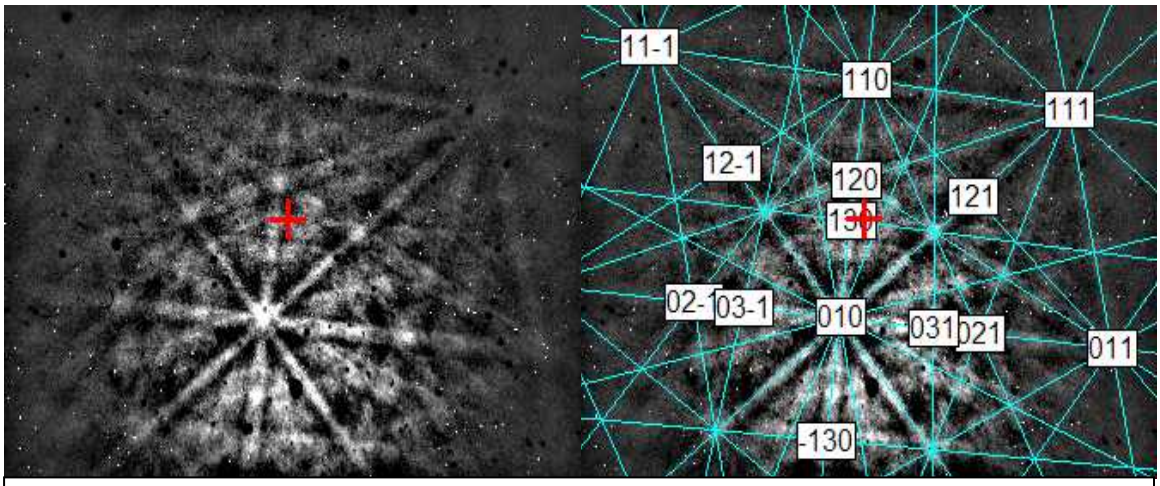

Figure 4. A) Kikuchi pattern obtained from Body Centered Cubic Iron; B) Indexing of the pattern performed by *Flamenco* software of HKL Technologies, Sunnyvale CA.

Software and Hardware

Field emission- scanning electron microscopy (FE-SEM) provided general imaging of the coupons before and after exposure to corrosion, Energy Dispersive X-Ray Spectroscopy (EDS) to identify chemical components within the sample, and Electron Backscatter Diffraction (EBSD) to identify areas of increased residual lattice strain of the samples. EBSD analysis was performed using the CHANNEL 5 system from HKL Technology.

Sample Preparation for EBSD

In order to increase Kikuchi band detection, polishing of each sample was performed prior to EBSD analysis. Each coupon was sequentially polished using the MetPrep 3 by Allied. The polishing of each coupon was accomplished using 3µm diamond, 1 µm diamond, 0.5 µm diamond, 0.1 µm diamond, and finished using 0.04 µm colloidal silica to remove any potential surface deformation due to the mechanical polishing. Once polished, samples were immediately mounted to a sample puck using colloidal silver paint to minimize charging of the sample due to the prolonged exposure to high currents. Utilization of this preparation technique provided EBSD Kikuchi pattern indexing rates greater than 85 percent on all scans used for analysis, and often indexing rates approached 95 percent.

EBSD Hardware Setup

The acquisition of strain information was performed using the same distances and beam settings for each analysis. During each acquisition, the FE-SEM stage was tilted to an angle of 70 degrees towards the EBSD detector, and then raised to a working distance of 15 mm. Once in position, the EBSD detector was then extended towards the sample 175 mm, which is illustrated in Figure 5. The EBSD detector box that links the hardware and software was set to *record* mode, and gain was kept at a value of 2 for

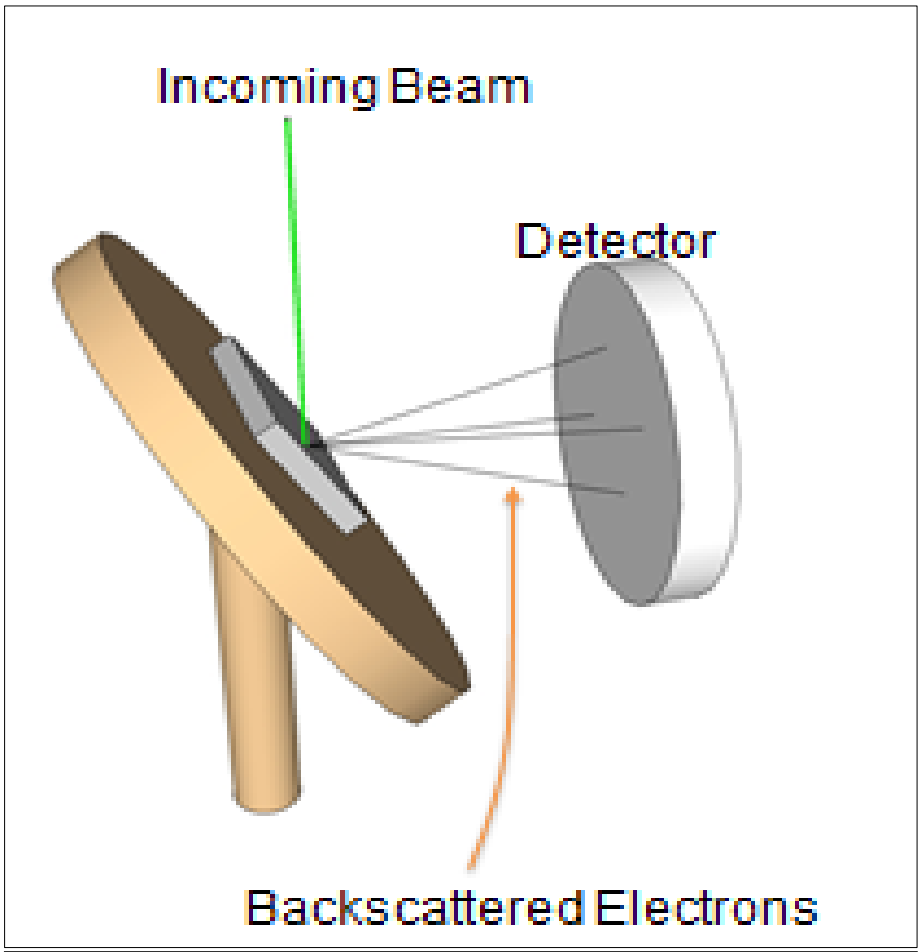

Figure 5. Schematic illustration of the stage, sample, detector and beam positions during EBSD analysis.

each scan. Beam settings were set to 20 KV, the *high current* mode was used, and apertures were set to 120 mm to enhance Kikuchi pattern detection capabilities by the EBSD detector.

EBSD Software Setup

All EBSD acquisition was obtained using the *Flamenco* software provided in the Channel 5 software package. The system was calibrated to detect Kikuchi patterns at various working distances upon installation. For each scan the calibration was used that had been specifically setup for analysis using 175 mm detector extension, and a working distance of 15 mm. The system needs manual calibration for each image magnification. Magnification calibration was performed using the *Spirit* EDS software, which was set to be the communication server between the FE-SEM hardware and *Flamenco* software. In order to scan the samples the types of materials present needed to be identified using the *Match Units* option in *Flamenco*. The materials selected for the scans were provided in the HKL, and alternate databases. Material selection included: Iron (old)-BCC, as well as Manganese-Sulfide (Hexagonal). The *setup* tab in the *Flamenco* software performs the acquisition of Kikuchi patterns, as well as the identification of material crystal orientation. For this process, the *spot mode* function for the FE-SEM needed to be used in order to focus the electron beam on a particular location that the user can select. Focusing the electron beam using *spot mode* produces a Kikuchi pattern from that exact location, enabling the user to calibrate the identification crystalline orientation based on the detection of Kikuchi bands at a known location. Several calibration locations are

necessary to provide the software with the information needed to accurately map crystalline orientation at each spot of the analyzed area.

EBSD Acquisition

Each EBSD acquisition time was minimized in order to reduce potentially damaging beam effects on the sample. In order to do this, scan times were kept at or near 1 hour. Scans lasting longer than one hour resulted in image error due to beam drift and charging of the sample. Depending on sample preparation and image magnification, step sizes for each spot acquisition varied from 0.1 µm to 0.25 µm.

Lattice Strain Maps

In order to obtain information about the residual strain our coupons, EBSD data is presented in the form of a local-misorientation map. A local-misorientation map provides data about the lattice strain of a coupon based on the change in EBSD Kikuchi pattern characteristics such as mean angular deviation (MAD) of the pattern's bands from that of a perfectly configured pattern for that lattice orientation, texture of the surrounding lattice, as well as the change in orientation of each point as a function of the orientation of the points surrounding that point. This is illustrated using a Figure 6, where a perfect unstrained lattice on the left correlates to Kikuchi pattern with crisp bands that correlate to a low MAD. Moving to the right side of the figure, the illustration of a misoriented lattice compared to the initial point is shown with its corresponding, rotated Kikuchi pattern. By taking the change of each pattern with respect to its

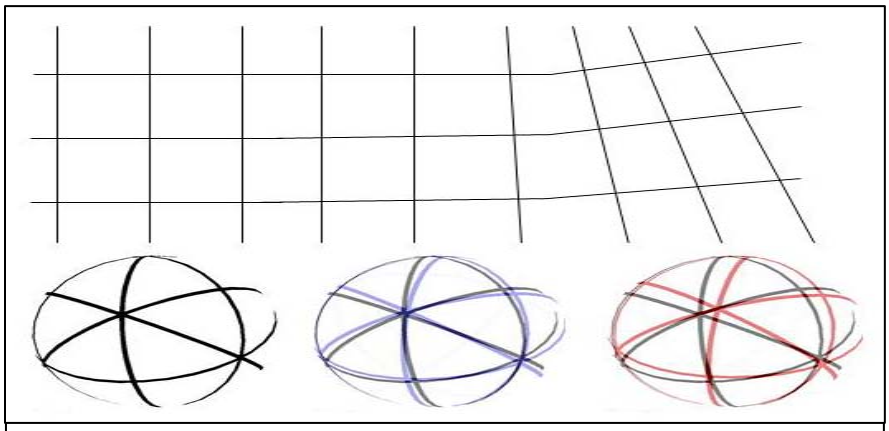

Figure 6 Illustration showing the correlation between an unstrained crystalline lattice and its corresponding Kikuchi pattern, as well as a strained lattice and its corresponding Kikuchi pattern. Black represents the unstrained pattern, while blue and red represent the change in pattern due to misorientation, The misorientation is used to interpret deformation and strain.

neighbors, the CHANNEL5 software is able to interpret the information, and provide a local-misorientation map corresponding to each data point of an area.

EBSD Mapping

Data obtained from an EBSD scan was translated to an information image referred to as an orientation map. The HKL software *Tango* provided this translation. Each sample set contained non-indexed spots where the *Flamenco* software was unable to calculate the orientation data for each spot. Image enhancement provided by *Tango* allowed us to extrapolate these non-indexed pixels based on the surrounding pixels. This type of enhancement minimizes discrepancy between pixels by interpreting information from several surrounding locations to provide the most likely orientation of that location. The types of maps used for the sample analysis include: phase, inverse

pole figure, and local misorientation, as represented in Figure 7 B, C, and D respectively. The inverse pole figure map provides information about 3 dimensional crystalline orientations as a function of the 2 dimensional locations on the sample. The information displayed takes advantage of miller orientation notation, and correlates each orientation value to a color from a gradient scale. The local-misorientation map builds on the information obtained pertaining to crystalline orientation by calculating the

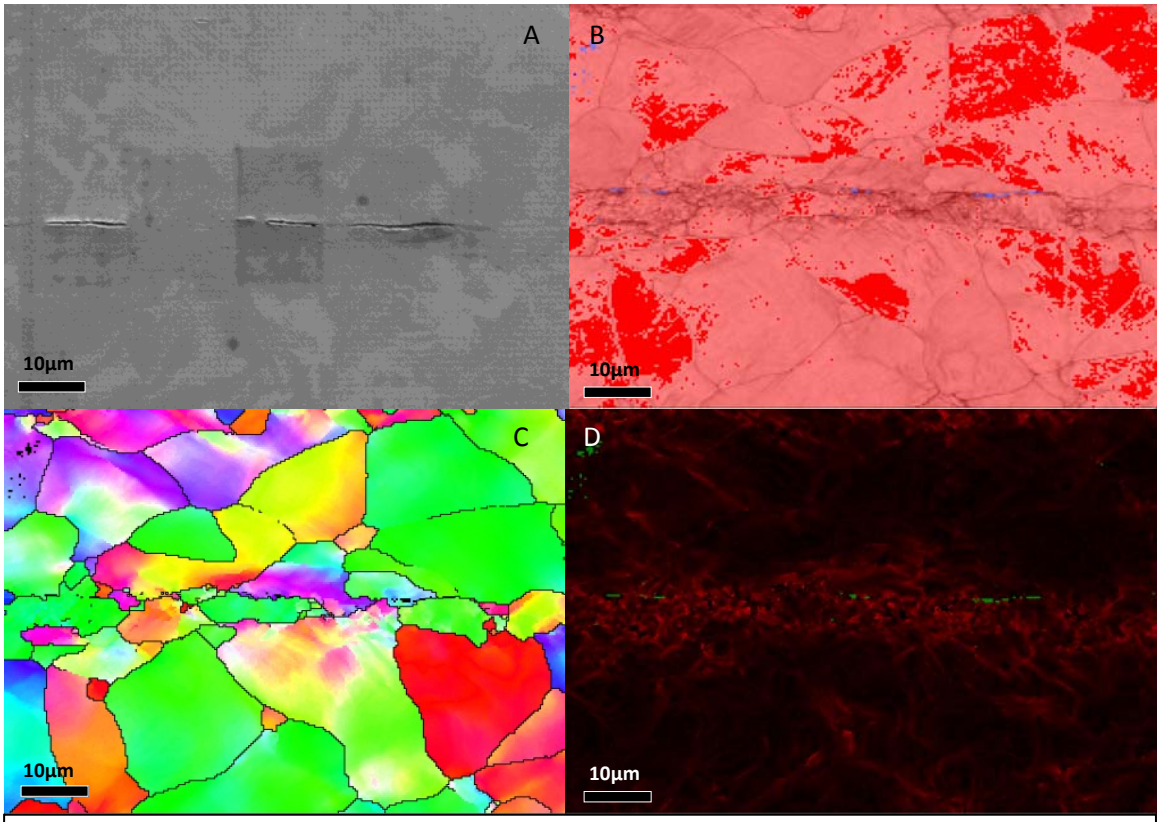

Figure 7. A) FEM image of a MnS inclusion running parallel to the surface of 1018 steel. B) EBSD-Phase map taken from the same area as A. C) Orientaion (IPF) map from the same area as A. D) Misorientation (strain) map of the same area as in A.

degree of change of orientation as a function of location. For example, a large change in orientation in a small distance results in a high value of local-misorientation in that area. The local-misorientation map, just like the orientation map, provides a map of local-misorientation where the amount of local-misorientation correlates to a color value located on a gradient scale. For all of the scans used, the color scale correlates to a minimum misorientation value of 0 degrees, and a maximum value of 6 degrees used for grain boundaries. The phase identification map allows for color-coding of different phases detected, while ignoring information about the orientation of that material. For example, some of the analyzed sample locations have long manganese-sulfide (MnS) inclusions running through the middle of body-centered cubic (BCC) iron called stringers. In the phase map of these locations iron will show up as one color, while MnS will show up as another regardless of orientation. The band contrast map is an alternate map not shown above, which provides information about surface texture, as well as material texture. It translates data obtained from the scan in terms of pattern quality. The primary use of this map was to aid in the identification of locations after corrosion, as provides a very good insight into what the sample looks like.

Removal of Electron Beam Effects

Exposure of a steel coupon to a high current electron beam at 20 KV may cause damage to the immediate surface of the sample. In order eliminate the effects of beam exposure such as cracking or reduction of hydrocarbons on the sample surface the sample was gently polished by hand using the Allied Chem-Pol polishing cloth. This

polishing cloth is made of soft polymer to eliminate removal of bulk iron, yet provides a means to remove the damaged iron from the sample surface. This was done prior to exposing any sample to a corrosive media.

AFM Overview

Atomic force microscopy (AFM) provided surface topography data from samples giving nanometer-scale resolution. For the purposes of this study the data scale of surface relief for locations taken before and after corrosion are set to the same scale, in order to provide accurate visual representation maps. All topography line scans were analyzed using the same scale as well. Locations analyzed before or after corrosion were performed with Mikromasch-NSC36/AL BS cantilever tips, using a Veeco Multimode V AFM system. Images were obtained using 256 pixels per line, and 256 lines per image.

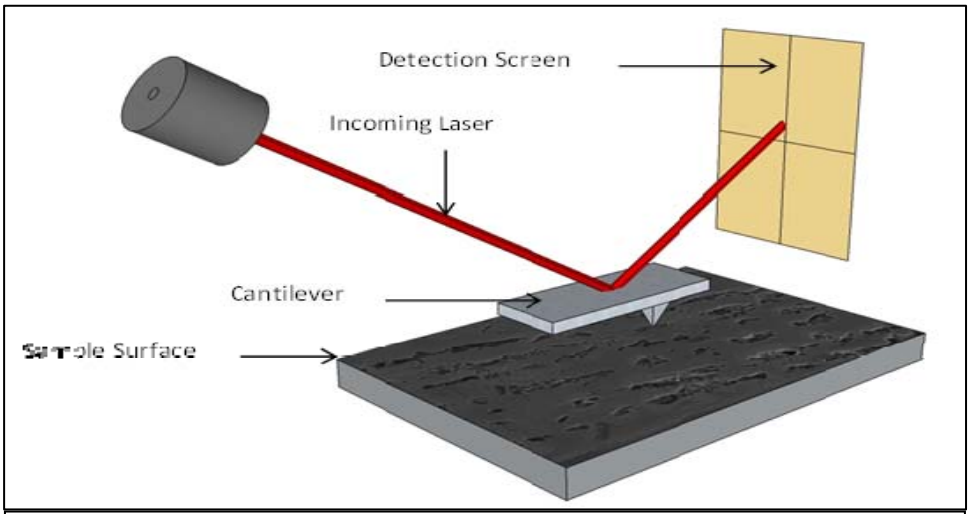

Figure 8. Illustration depicting the key components of AFM surface analysis.

The images were acquired at scan rates ranging from 0.200 Hz to 0.300 Hz.

AFM is able to provide 3-D surface measurements that are very sensitive to small changes in surface topography that can provide nanometer scale surface resolution. Scan area of AFM topographical maps are limited to 100 µm or less.

AFM works through the use of a laser, cantilever, and detection screen. The laser is focused by the user onto the backside of a flexible cantilever. The cantilever had a spring constant of 0.6 (N/m) and moves up and down according to the interaction between the sharp tip and the surface of the sample. Bumps in the sample cause the cantilever to rise, while depressions in the surface cause the cantilever to lower. The laser is reflected off the back surface of the smooth cantilever, and reflected to a photodiode. This screen then translates the calibrated signal position to a height on the sample surface. The mechanical components of this process are shown in Figure 8. The software then measures the change in location of the reflected signal from point to point along a scan due to changes in the topography.

By comparing positions along a scan, the software can then produce a map of the sample's surface, much like a topographic map that shows mountains and valleys. The key function of AFM in this study was to measure surface topography before and after corrosion, and to use the changes in these features in order to determine the rate of local anodic dissolution on the surface of the 1018 steel during corrosion. An example of an AFM scan across a MnS inclusion is shown in Figure 9.

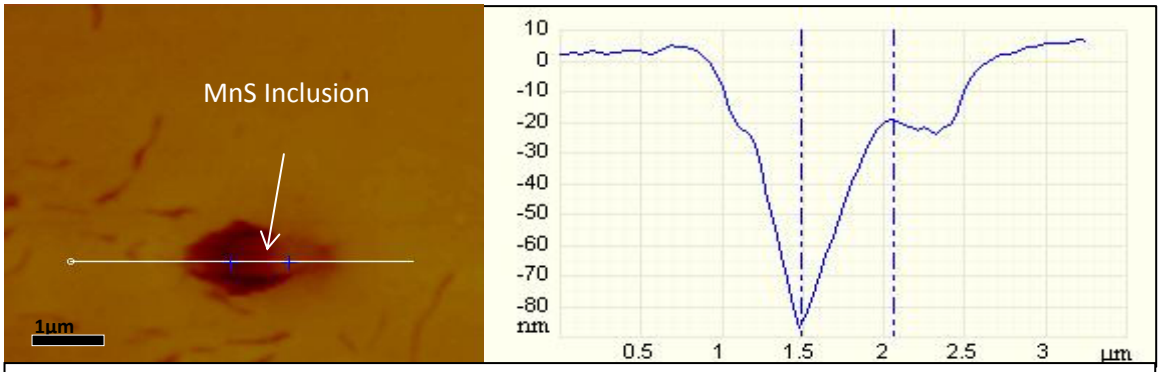

Figure 9. AFM scan on the left of a MnS inclusion in 1018 steel after polishing to 0.04 µM colloidal silica. The accompanying depth plot on the right corresponds to the line drawn across the AFM image, revealing the change in surface topography around the inclusion.

Biotic Corrosive Environments

Bacterial Cultures

Bacterial cultures for *Marinobacter aq., Desulfovibrio Indonesiensis, and Desulfoglaeba alkanexedens* (abbreviated ALDC for this study) provided the corrosive environment for several of the experiments performed. The cultures for *D. Indonesiensis, and Desulfoglaeba* are made using Widell media, a reducing agent, Resazurin for oxygen detection, and growth components such as lactate (for *D. Indonesiensis*), as well as acetate (for *Desulfoglaeba alkanexedens).* These cultures were stored in capped and crimped vials containing headspace filled with 5% H_2 gas, 25% CO_2 gas, and balance N_2 gas. The *Marinobacter aq.* cultures did not include Resazurin or the reducing agent since they are aerobic, and were often made 24 hours prior to use by adding freshly thawed pure culture to growth media and allowing them to culture overnight in seawater in an incubator in a sealed Falcon tube.

The use of an anaerobic chamber allowed for the development of anaerobic experiments involving live bacterial cultures immersed in culture media. These experiments were performed inside of the anaerobic chamber, which was flashed with nitrogen gas to remove the O_2 gas within the chamber. Further elimination of oxygen was performed through the use of a catalyst that converted oxygen gas to water vapor, which was adsorbed to the catalyst itself. The reliability of the glove box in providing an anaerobic environment was monitored through the use of XPS and EDS of samples after exposure to make sure that no corrosion deposits associated with Fe oxides were present on the surface. When oxygen was deemed present in the system due to intentional exposure of the system to the external environment, or when corrosion deposits on the surface of the steel after exposure showed a presence of oxygen in the corrosion product, then these experiments containing low levels of oxygen will be referred to as sub-oxic experiments.

Naval Fuel Tank Simulation Environments

The analyzed steel coupons were each put into a single vial containing 2 ml of a naval fuel, 5 ml of 0.2 μm-filtered seawater obtained from Key West Florida, and initially only *Marinobacter*. Each square coupon was suspended using an inert Teflon string. The top of the vial was capped and crimped, and a 16-gauge needle was inserted through the stopper on the top of the vial to allow for oxygen flux into the system. This needle was connected to a filter of pore size 0.2 μm, to inhibit external bacterial contamination of the system while allowing O_2 to enter the vial. An illustration of this setup is seen in

Figure 10. Oxygen measurements were taken, as described in section 2.5a. Upon depletion of oxygen levels in the seawater to below the anaerobic bacterial survival of 0.1 ppm, the vials were inoculated with *D. indonesiensis*, an anaerobic sulfate reducer utilizing the anaerobic glove box. This system most closely mimics that which is seen in a naval fuel tank while at sea. Primarily, it contains a layer of seawater overlaid with a layer of fuel, in a contained environment with iron present, as well as bacteria, and not completely isolated from oxygen.

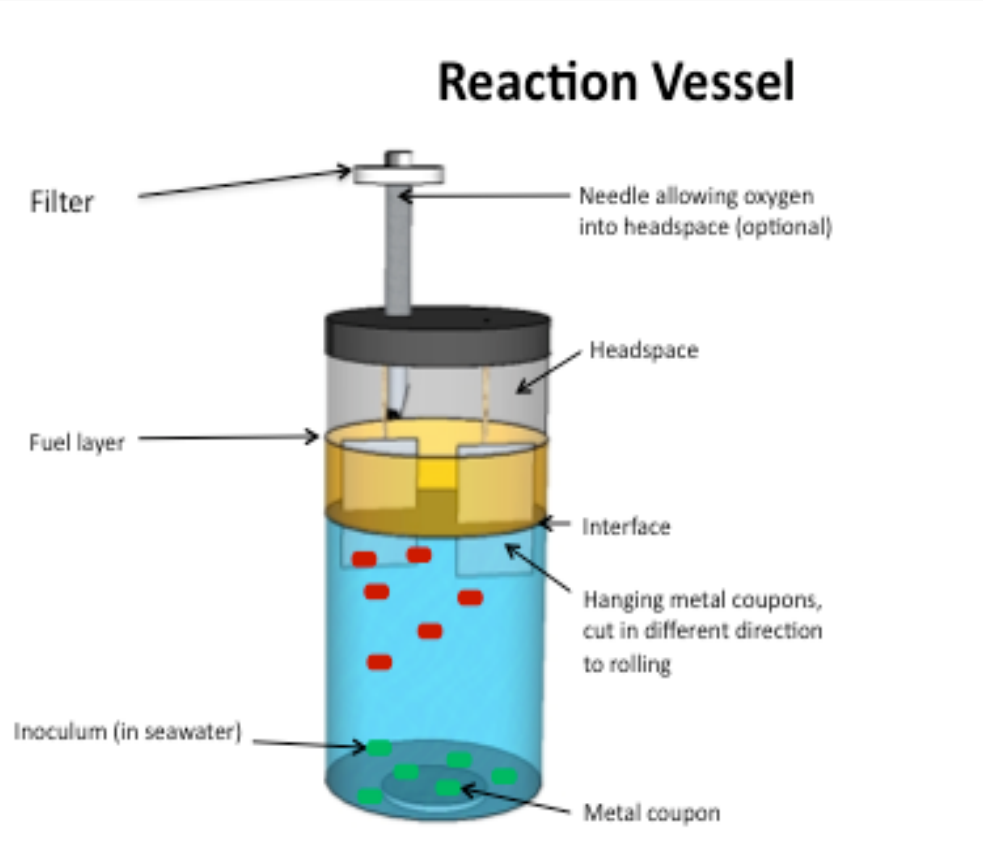

Figure 10. Aerobic oxygen vessel constructed to simulate a fuel/seawater ballast tank for a Naval ship.

Oxygen Measurements

Oxygen Probe Calibration

All dissolved oxygen measurements were obtained using the FireSting microprobe oxygen sensor system, along with the accompanying FireSting Logger data acquisition software. Calibration of the oxygen probe was performed according to the FireSting user manual calibration recommendation. A two-point calibration was used with two points consisting of a 100 percent O_2 saturated water, and a 0 percent dissolved O_2 in water. A fully saturated water calibration sample was prepared using 5 mL of deionized water contained in a 5 mL glass vial, which was sealed via a rubber cap and crimped using a metal cap crimp. Once sealed, the water was purged with compressed air for 30 minutes. The purely unsaturated water was created using the same technique; however the vial was purged at a rate of 10 liter/minute using compressed nitrogen, in place of compressed air. The calibration vials were immediately measured using the oxygen probe. The vial purged with compressed air was used to set the 100 percent saturation value in the FireSting Logger software, while the nitrogen purged vial was used to set the 0 percent saturation value.

Oxygen Measurement Apparatus

Depth measurements were made using a digital caliper attached to a micro-sensor manipulation apparatus developed in the lab. The apparatus allows for the vial to be clamped in place, in the upright position, using metal clamps covered in rubber. The clamp elevates and isolates the vial from any highly heat-conducting surface, thus

minimizing effects of temperature change of the vial due to the environment of the microprobe location. The FireSting oxygen sensor was also clamped in place, and through a process of screws and adjusters the probe was lowered into the vial at a known depth by precision manipulators. All depth measurements were made using a millimeter sized steps starting from the fuel surface until the probe reached to 10 mm below the fuel/seawater interface, a total range of about 20 mm with 1 mm intervals. An illustration of the apparatus is seen in Figure 11A, while a schematic illustration of the oxygen probe while inserted into a reaction vial is seen in Figure 11B.

Biyotrap

The Biyotrap is a chemically modified filter that has been developed in our lab for bacterial capture and concentration. The Biyotrap can be used to isolate bacteria for further uses without killing the bacteria. Unlike size exclusion filters which utilize small pore sizes to selectively filter bacteria from their fluid media, Biyotrap is a highly porous mesh consisting of glass wool fibers that have been activated by applying Amino-Propyl-Methyl-Diethoxy Silane (APMDES) through chemical vapor deposition to the glass wool. The deposition of APMDES on the surface of the fibers creates a negatively charged field around each fiber. The charge interaction of the surface with the bacteria allows for non-terminal selection of bacteria upon the surface of the glass wool fibers themselves.

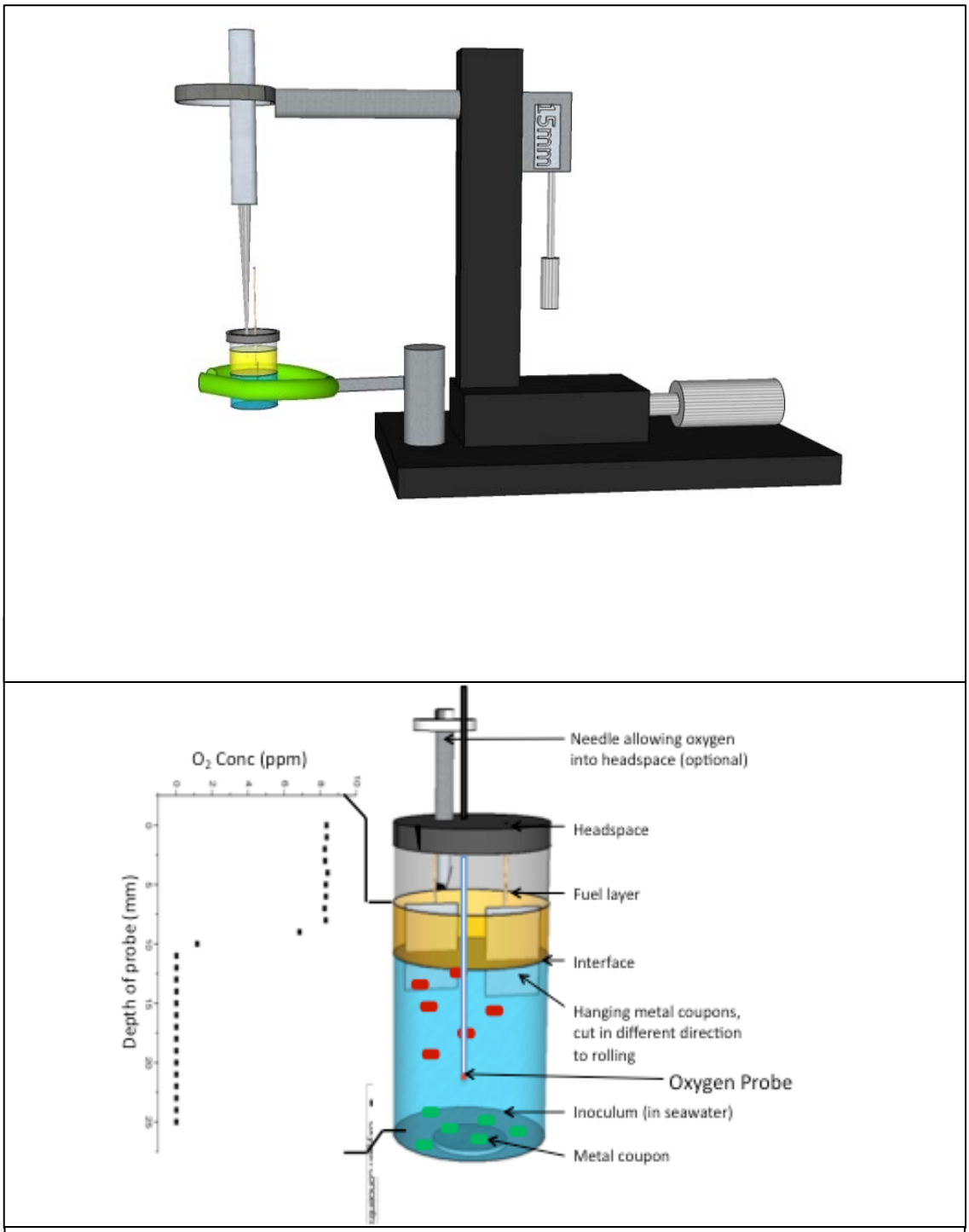

Figure 11. A) Illustration of the micromanipulator used for dissolved oxygen profiling. B) Illustration of the oxygen depth profile in relation to a model reactor.

These bacteria can then be removed from the filter by washing with the desired experimental fluid. For the experiments performed where Biyotrap was utilized, Biyotrap was used to remove sulfate-reducing bacteria from their growth media, which contain elevated levels of sulfide. The bacteria were then washed in the trap using filtered sterilized seawater, and finally inserted into the experimental vessel. This type of isolation has been shown to remove residual sulfide that may be present in the initial fluid. By removing sulfide, we are able to ensure that any corrosion of the steel due to sulfide presence is due to the production of sulfide from the SRB during the exposure period rather than from any sulfide that may have already been present in the SRB-containing media.

The mechanisms used for bacterial isolation using Biyotrap are illustrated in Figure 12. A 60 mL syringe was utilized, along with a syringe pump to ensure steady flow through the Biyotrap during isolation, illustrated on the left of Figure 12. Flow rates were set at 40 mL per minute. All SRB isolation using the Biyotrap was performed in the anaerobic glove box, using nitrogen purged seawater to ensure survival of the SRB during the process.

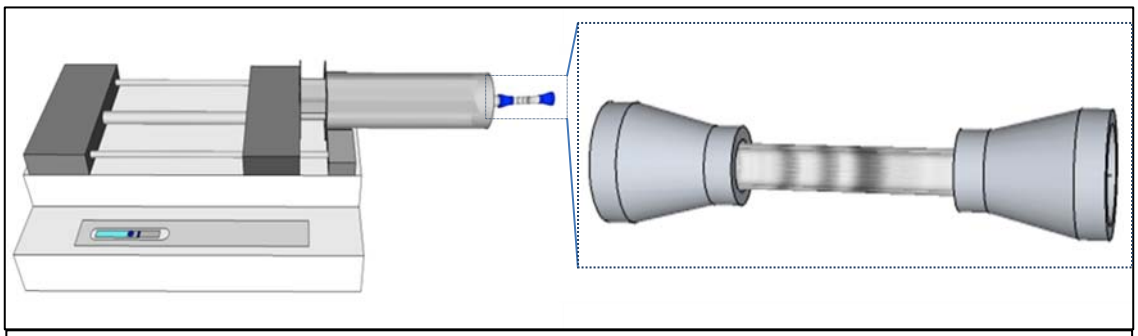

Figure 12. Left) Illustration of the Biyotrap attached to a 60 mL syringe being compressed by a syringe pump, and Right) a magnified schematic drawing of the actual Biyotrap apparatus outlined by the dashed rectangle.

Removal of Corrosion Deposits

In order to analyze the surface of the steel coupon after exposure, the corrosion deposits formed on the surface of the coupon needed to be removed. This was performed using one of two solutions prepared in the lab using ASTM standards. One solution will be referred to here as “Clark Solution”, which contains 500 mL 1 M HCl, 500 mL H_20, and 3.5 g Hexamethylenetetramine. The Clark Solution uses a mild acid to dissolve the corrosion deposits. Another solution contains a mild base to remove corrosion deposit without removing or MnS inclusions. The solution is made of 200 g Diammonium Citrate $(NH_4)_2HC_6H_5O_7$ with reagent water to make 1000 mL of solution. The basic solution requires an elevated temperature to remove corrosion deposits, therefore it was heated to 75 degrees Celsius and each coupon was exposed to the solution for a time period sufficient enough to remove all of the corrosion deposition yet short enough to minimize dissolution of the bulk iron. Times for exposure varied from 10 seconds to no more than 1 minute, depending on the amount of deposit formation on the surface. This amount of time was sufficient to remove all deposits formed during exposure, and allowed for further surface analysis of the surface left behind after the corrosion deposits are removed. The low pH Clark Solution is a rapid removal technique, and exposure time of each coupon was no more than 5 seconds. After any stripping of the coupon, it was immediately rinsed with deionized water to remove any residual stripping solution.

. After rinsing, the coupon was then immediately dried using a high flow rate of dry nitrogen stream to ensure no further corrosion was taking place due to water on the surface. An example of a frequently seen corrosion crystal is seen in the image on the left side of Figure 13, while an area that has been stripped of corrosion deposits is seen in the image on the right side of Figure 13.

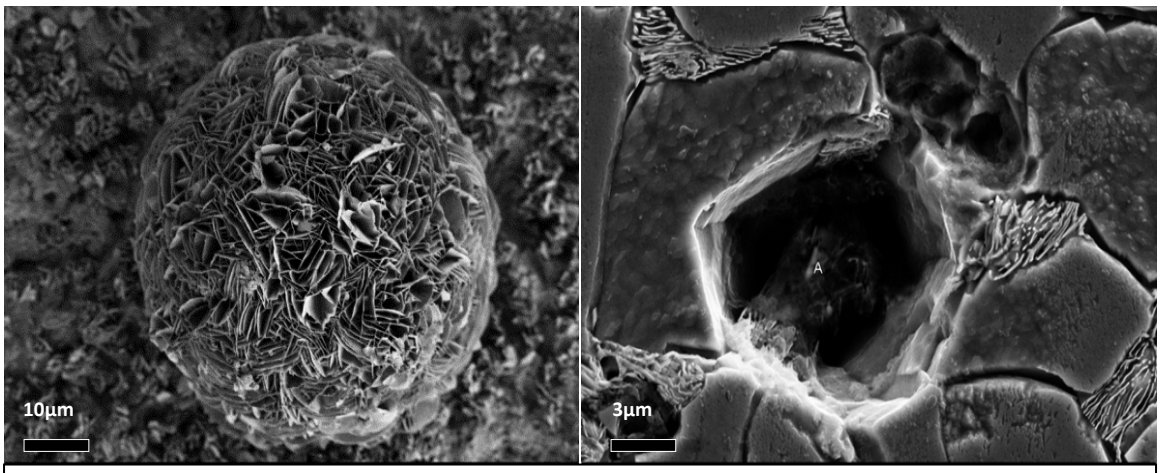

Figure 13. A) FEM image of a corrosion deposits prior to removal. B) FEM image of a 1018 steel sample surface after removal using Clark Solution.

Mass Loss Measurements

For mass loss corrosion rate measurements the mass of each coupon was measured directly prior to exposure to corrosive media. Each coupon was again measured for mass loss after stripping of the corrosion products for each experiment. The difference in mass gave us the mass lost as a result of corrosion.

Electrochemical Experiments

Electrochemical Reaction Vessel

Electrochemical measurements were used alongside mass loss measurements to establish corrosion rates of materials in electrolyte solutions. In order to perform these measurements, a key requirement of an electrochemical setup in an anaerobic environment was an anaerobic reaction vessel to ensure survival of SRB during experimental measurement. A vessel (vial) similar to the one shown on the left side of Figure 14 was designed similar to that described in section 2.4. The vessel was further modified to allow for the introduction of a silver-silver chloride (Ag/AgCl) reference electrode, a platinum counter electrode, and the use of the carbon steel coupon as a working electrode. The Teflon string from the earlier reactor development was replaced with Teflon coated copper wire that attached to the steel coupon through a hole drilled towards the top of the coupon. The wire was wrapped through the hole, and coated with colloidal silver paint to ensure a direct connection at the interface of the wire and the steel coupon. This connection was tested using a voltmeter. This area was then covered with several layers of impermeable Devcon brand epoxy to ensure that there was no direct interaction between the wire and the saltwater. This wire was inserted through the stopper to allow for connection with the potentiostat/galvanostat. The platinum wire was similarly run through the rubber stopper and located opposite the working electrode inside the reaction vial.

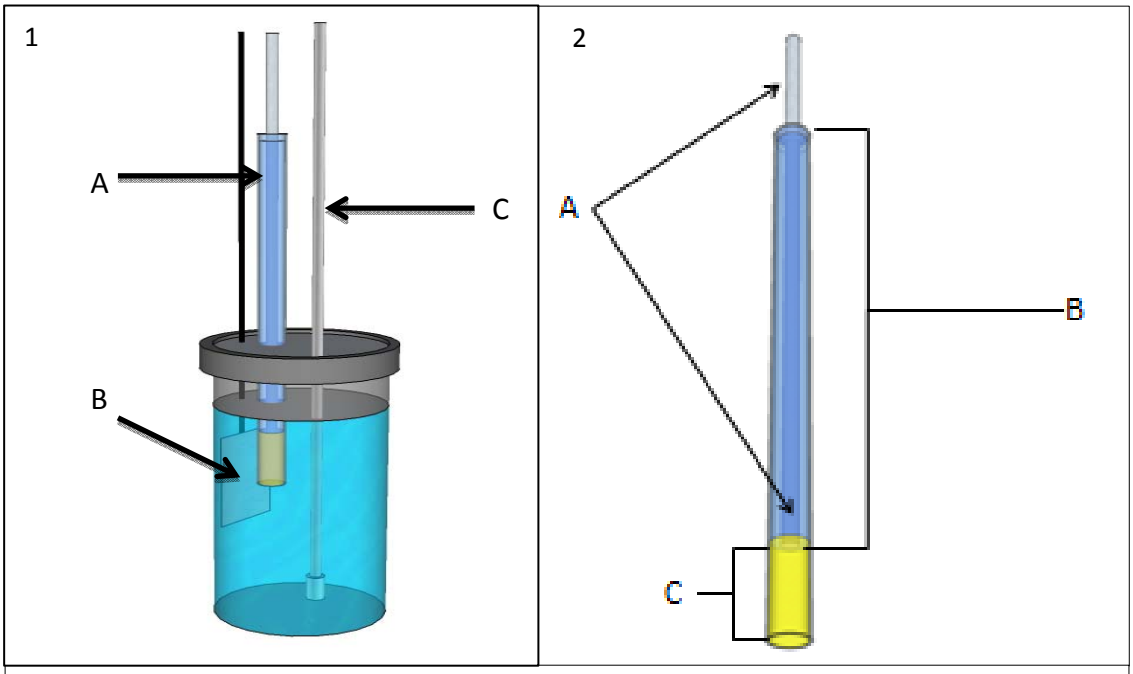

Figure 14. 1) Illustration of the electrochemical reaction vessel developed in the lab. A) Ag/AgCl capillary reference electrode. B) Working electrode (1018 steel coupon) suspended using a thin insulated Cu wire. C) Platinum-wire as a counter electrode. 2) Illustration of the Ag/AgCl reference electrode used for the electrochemical experiments. A) Silver wire. B) KCl solution inside of the glass capillary. C) Agar

The reaction vessel was then filled with the SRB containing medium inside of the anaerobic glove box, and the vessel was capped and crimped inside of the glove box. To eliminate diffusion of oxygen into the system along the components inserted through the stopper, the surface was coated with a layer of epoxy and allowed to dry before removal from the glove box. In order to allow for insertion of the Ag/AgCl reference electrode, a pipette tip was inserted through the cap of the vessel to act as a conduit for the small glass capillary to be inserted. The pipette tip was sealed with another pipette tip filled with a thick layer of silicon caulk to eliminate oxygen diffusion. In fact, most of

our anaerobic experiments were kept in the glove box during electrochemical measurements and wires were inserted inside the anaerobic chamber to conduct these measurements. If vials were taken outside the oxygen measurements were used to verify the presence or lack of dissolved oxygen in the vials.

Constructing a Reference Electrode

The Ag/AgCl reference electrode was prepared using a glass capillary, KCl saturated agar, AgCl coated Ag wire, and potassium chloride (KCl) with concentration of 3.5 mol/liter made with deionized water. Prior to use, the silver wire required coating with AgCl. Low grit sandpaper was used to remove any possible tarnish or oxide layer buildup on the silver wire. Next, 1-2 cm of the tip of the silver wire was inserted into 3M HNO_3 solution for a couple of seconds to further remove any surface contaminants. The tip of the silver wire was then put into 0.1 mol/l HCl solution, and attached to the PAR-273A potentiostat as the working electrode. Using a Unisense Ag/AgCl reference electrode and a pure graphite rod as the counter electrode created the needed circuit to allow for electroplating of the AgCl onto the silver wire through the electrochemical processes given as:

$$2Ag\ (s) + 2HCl\ (aq) \rightarrow 2AgCl\ (s) + H2\ (g).$$

A potential of 0.75 Volts was applied to the wire while it was in the HCl solution for 3 hours. These parameters allowed for deposition of pure AgCl upon the surface of the wire, verified by EDS and seen in Figure 15. The thickness of the deposit on the wire was measured using FEM, shown in Figure 16. The thickness of the layer after 3hrs at a

potential of 0.75 Volts equaled 36.35 µM. This correlated to a rate of approximately 10.2 µM of deposition per hour.

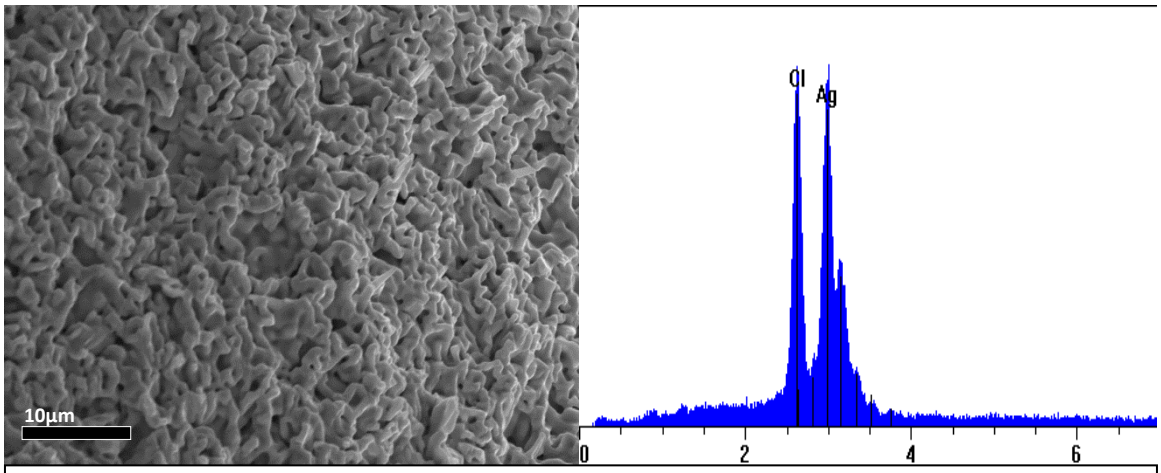

Figure 15. FEM image (left) of AgCl deposition on a silver wire after 3 hours in 0.1 M HCl with applied potential of 3 Volts.

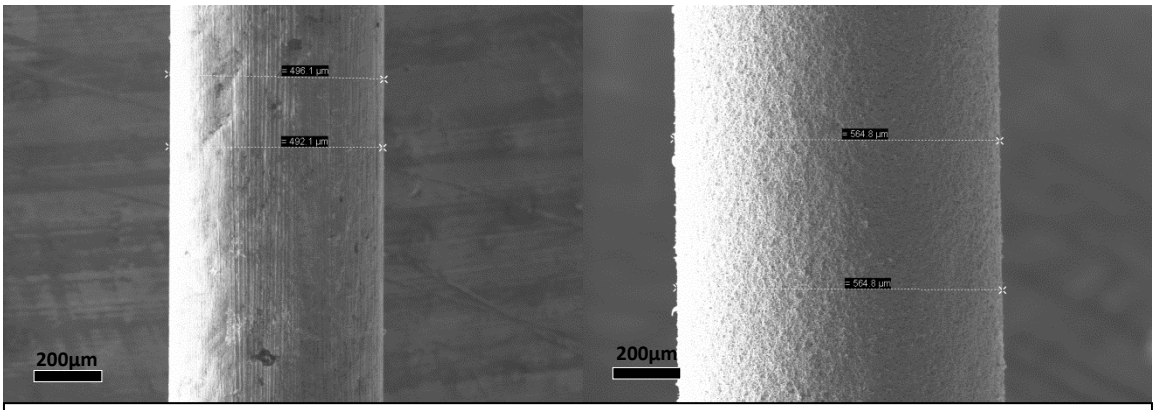

Figure 16. FEM images of a pure silver wire (left) and the same wire with AgCl coating on the surface (Right) after deposition using electro-plating of AgCl in 0.1M HCl for 3 hours at an applied voltage of 0.75 Volts.

The AgCl coated silver wire was inserted into the capillary, and then hot agar was added to the other end of the capillary to act as a salt-bridge and to ensure accurate

measurements by the reference electrode during the electrochemical experiments. 3.5M KCl was then added to the capillary through the use of a stretched glass pipette to act as a buffer solution to continuously supply chloride ions to the silver wire and the agar salt bridge. The top of the capillary was glued using epoxy to ensure stability and to eliminate evaporation of KCl. Throughout the construction of the electrode, great care was taken to ensure no air bubbles existed in the system that could potentially serve to block ion flow to the electrode.

Electrochemical Measurements

Electrochemical measurements and analysis were performed using the Princeton Applied Research model 273a (PAR-273a) potentiostat/galvanostat. Open circuit potentials were obtained using the PAR-273a during exposure of some experiments to help the researchers understand the state of the electrochemical processes which were occurring in the vessel. Corrosion resistivity measurements were also taken at pre-assigned intervals to establish corrosion current densities for the sample at the corresponding time of exposure However, as discussed in Chapter 1, diffusion of ions across the double layer puts severe limitations on Tafel plots hence we decided to use the linear portion of the $\Delta\varphi$ vs. i plot near the equilibrium potential. For the measurements taken during this experiment, the slopes were taken tangent to the curves at or near ~5mV above and below the equilibrium potential. From these slopes we determined the corrosion resistivity R in Ohm-cm^2, and from this value we

determine the corrosion current $i_o = \frac{1.28\times10^{-2}}{R}$ in Amps/cm^2. From this value we determine the corrosion rate as $\tau = 1.16 \times 10^4 \, i_o$ in mm/year.

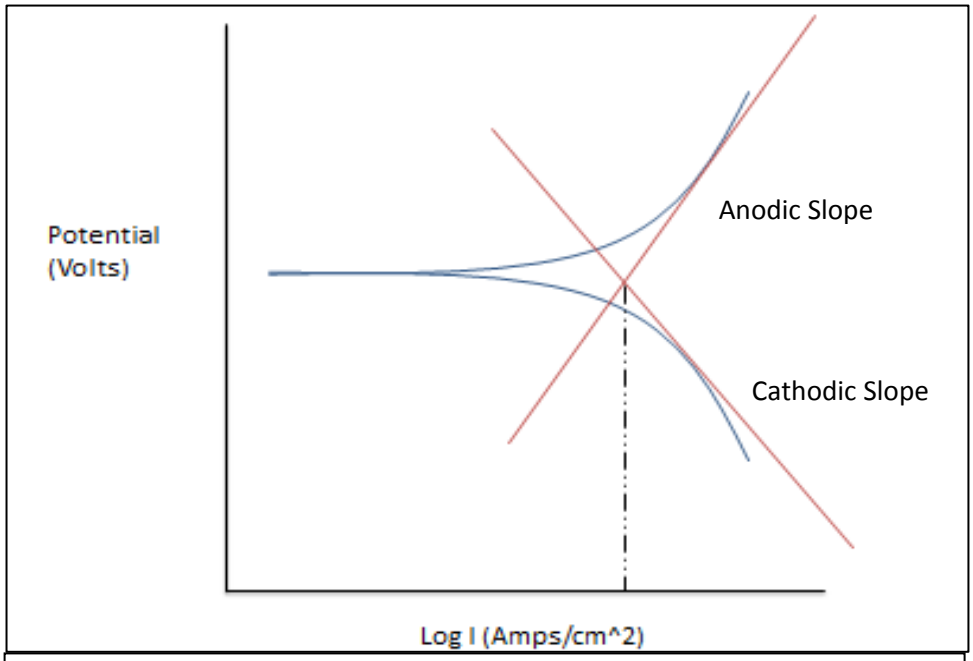

Figure 17. Example an Evans diagram, $\Delta\varphi$ vs. Log *i,* plots illustrating the anodic and cathodic Tafel slopes (red lines) set tangent to the linear portion of the potential resistance curves. The dotted line identifies the i_o=$i_{corrosion}$ value for the system, and the horizontal portion of the plot illustrates the location of the equilibrium potential.

RESULTS AND DISCUSSION

The Role of Strain in Microbially Influenced Corrosion

Corrosion Environment

The analyzed steel coupons were each put into individual vials containing 5 mL of sulfide media, and suspended using the Teflon string as described in the previous section. This media contained *Desulfoglaeba alkanexedens* (also known as ALDC), a hydrocarbon degrading sulfate reducing bacteria (SRB), along with the carbon sources needed for growth. The exposure period for this experiment was 14 days, and occurred within a sealed anaerobic glove box with low oxygen content to maximize the corrosion effects due to sulfide while still having trace amount of oxygen continuously entering into the system. This environment is called suboxic. The resulting corrosion products of the experiment were determined using EDS.

Chemical Deposition

After 14 days of exposure to the ALDC environment, coupons showed signs of low level oxygen corrosion in a sulfide rich environment. The results of the corrosion product formation on the surface of the coupons are shown in Figure 18. In the FEM image shown in Figure 18, corrosion deposits are the rough areas on top of the polished surface. These corrosion products correspond to surface depositions consisting primarily of iron-sulfides, as well as iron-oxides.

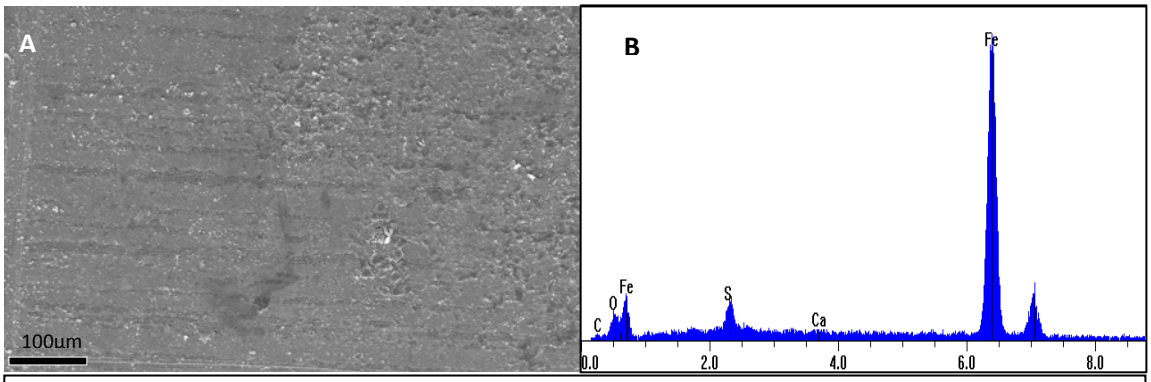

Figure 18. A) FEM image taken at 20Kv with a magnification of approximately 440x, of a parallel cut coupon after 14 days exposure to SRB-MIC environment, and B) the accompanying EDS spectra.

Corrosion of Coupons Cut
Parallel to the Rolling Direction

Analysis was first performed on a parallel cut coupon prior to exposure to ALDC media. An area of interest was selected and imaged with a 20 KeV electron beam using basic FEM imaging techniques. The FEM imaging of the same area after 14 days of exposure, and followed by the removal of the corrosion product, shows a detailed view of smooth areas that have undergone minimal corrosion, and the rough areas that have undergone trench-like corrosion, see Figure 19. As mentioned earlier, analysis of clean

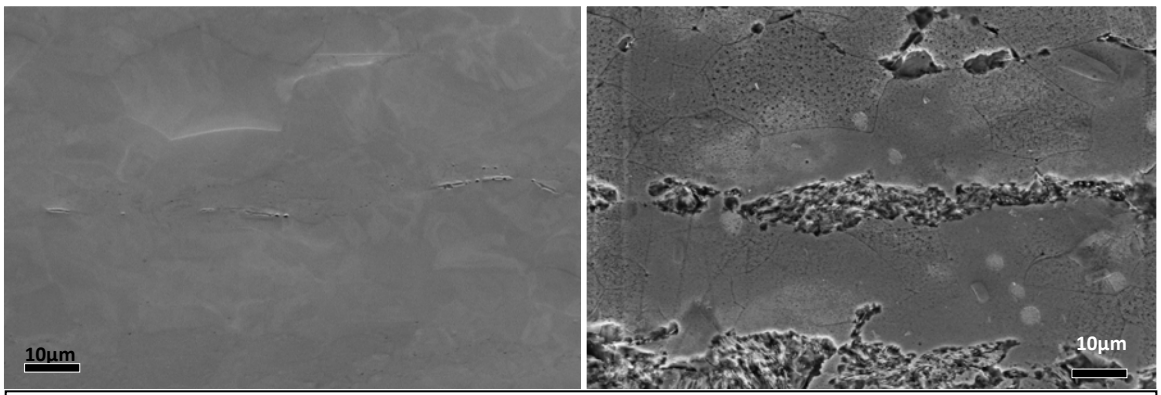

Figure 19. Left: FEM image of a location on a polished, parallel cut coupon. Right: Same area after 14 Days exposure to ALDC

surfaces included EBSD mapping using 20 KeV electrons at a working distance of 15 mm. The local-misorientation map obtained as a result of this analysis is shown in Figure 20. In comparing the FEM image in Figure 19 corresponding to the corroded surface and the EBSD misorientation map of the clean surface, grains and grain boundaries visible in each map may be used as aids. In the EBSD local-misorientation map in Figure 20, the areas colored orange-red correspond to high misorientation and hence highly strained which correlate with high corrosion in Figure 18, while the other areas appearing as blue and green corresponding to low strain show low corrosion. This is an important observation where the areas mapped as highly strained ended up corroding the most after 14 days of exposure to the ALDC media, which can be charaterized suboxic and sulfifogenic.

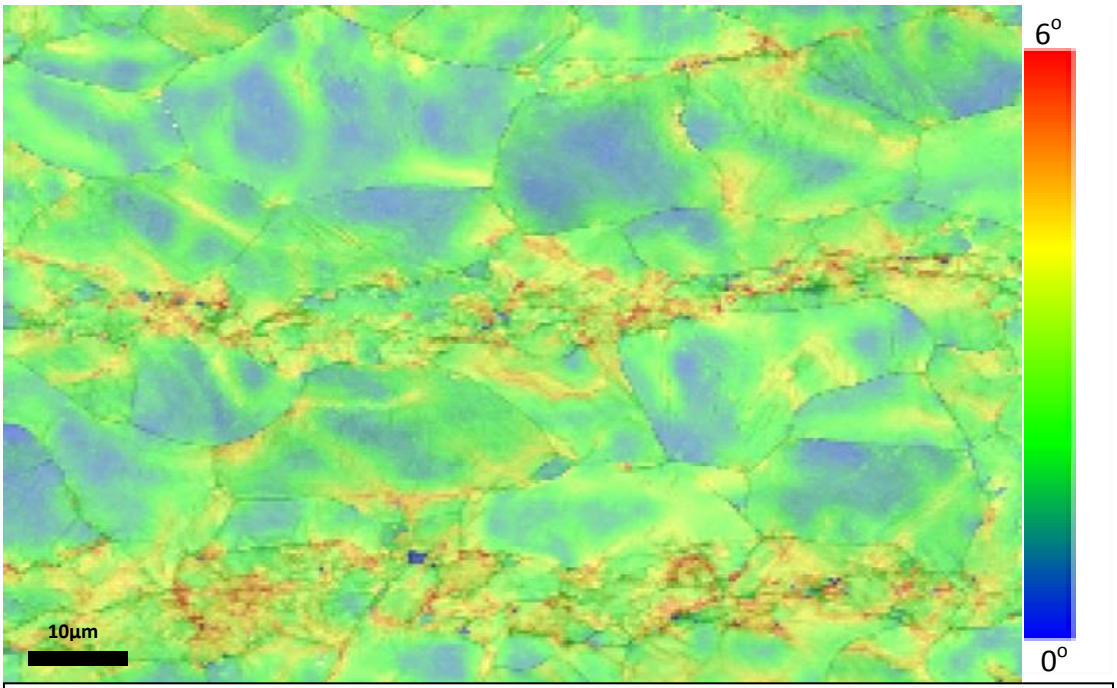

Figure 20. Local-misorientation map of the same area shown in Figure 19.

To understand the color scheme in the misorientation maps we resort to the HKL software which enables the user to select a point within the map to view the orientation as interpreted by the software. Figure 21.A shows four selected points equally spaced along the vertical axis in the image. Visual inspection shows that there is a correlation while moving position from point 1 to point 4 within the designated area with the displayed 3-dimensional cubic lattice given on the right side of the figure. Strain amount is very low at points 3 and 4, shown as blue, while these values increase to highly strained when moving towards points 1 and 2. By looking at the orientation of the BCC iron along this same motion, the orientation changes very little in areas corresponding to blue-green low strain, while the orientation changes rapidly in the area of orange-red representing the highly strained lattice.

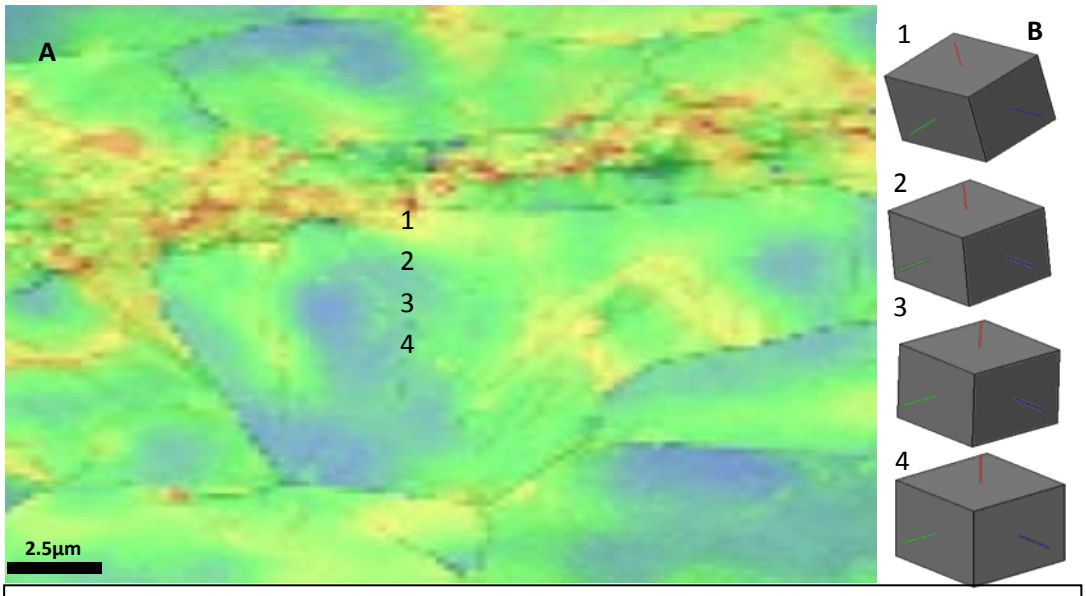

Figure 21. Local-misorientation map of an enlarged section of Figure 17 with locations 1-4 corresponding to the crystal representation given by illustration of the 3-D BCC cubes on the right.

Image Analysis Using Matlab

Further verification of the correlation between accelerated corrosion and strain at this location was achieved using a MatLab code the author has developed, which was written to perform image alignment and similarity analysis of the AFM and Strain images for the same location. In order to do this, the images were first converted to binary and set in a way that the relative brightness and contrast were the same so that the regions of strain and the regions showing more corrosion could easily be identified. This was performed using the built in Matlab function "*imadjust*" which allows basic contrast and brightness adjustments to be performed on the loaded image file. Since the AFM image uses dark areas to represent deeper areas on the surface, the colors of the image were also inverted so that the deep areas corresponded to light areas in the binary image, seen in Figure 22A. This inversion is important when comparing the depth image to the binary strain image given in Figure 22B.

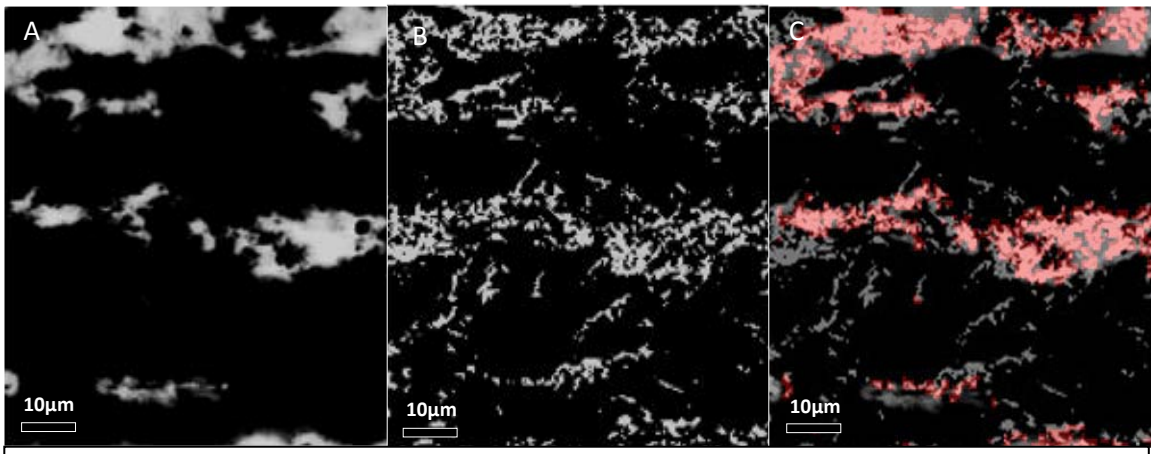

Figure 22. Image comparison of A) an AFM image taken of a location after corrosion. B) The strain map of the same location. C) A Matlab created image overlay of the two images with areas of intersect highlighted in red.

The images were then overlapped in Matlab, and the points of intersection between the two images were established and colored in red. The image overlay and red shading of the AFM image and the corresponding EBSD misorientation map is shown in Figure 22C. Visual analysis of the image portrays many areas of overlap, as shown by the red. Comparison of the red intersected areas in this figure reveals a high correlation with the areas in the AFM image that represent depth. Areas in red also correspond to areas of strain, though there is other strain that is present outside of the corroded areas. This analysis suggests that in corroded areas there is a clear presence of strain, while not all strained areas are corroded. On the same note, in unstrained areas there exists little or no accelerated corrosion found on the AFM surface analysis. A side by side comparison of the raw data represented by the FEM image, EBSD strain map, and AFM image are shown in Figure 23 for further illustration of the results.

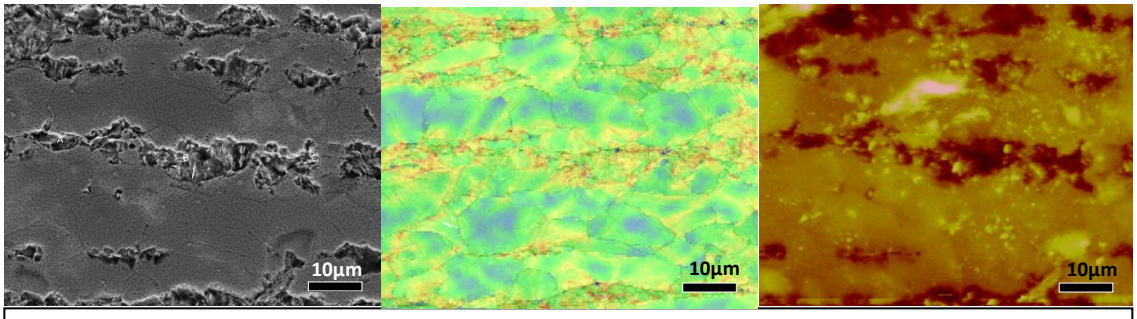

Figure 23. FE-SEM image(Left), Strain Map(Center), and AFM surface topography (Right) of the same area of a parallel coupon after corrosion in ALDC environment.

Strain Accelerated Corrosion

The local misorientation maps provided by the HKL Software are composed of pixels containing combinations of red, green, and blue values in order to provide the visual map. For quantitative analysis, a single value per pixel was required to calculate the strain value from the local misorientation value. In order to do this, the local misorientation map was converted to gray scale using the built in Matlab function "rgb2gray" so that each pixel had only 1 value that represented the amount of local misorientation, rather than values for red, green, and blue. The RGB and greyscale images for this area are shown in Figure 24. Once the data was converted, the image becomes a matrix of size 300 columns by 300 rows where each spot in the matrix represents a pixel with a value that correlates to the degree of misorientation.

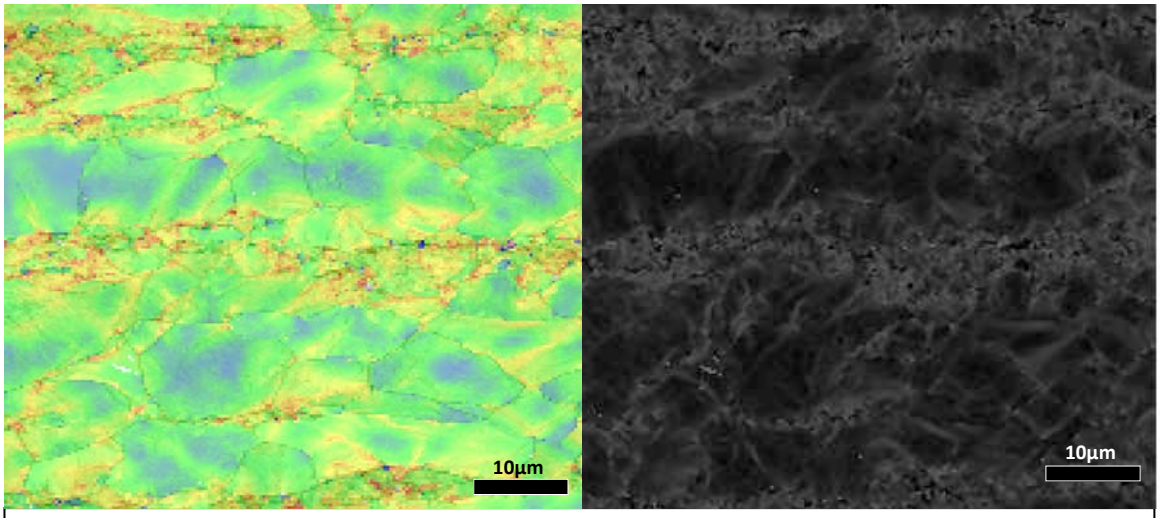

Figure 24. A local-misorientation map acquired from EBSD (Left) and the same map after being transformed from RGB into grayscale using Matlab (Right). The grayscale image has been brightened to allow for visual verification of that it is indeed the same area as the figure on the left. The actual data shows less visual contrast.

According to mechanochemical theory of strain accelerated corrosion, we hypothesize that the areas exhibiting larger strain, as recorded by the local misorientation map, would act as sites for accelerated anodic dissolution of the metal.

In order to establish the anodic dissolution rate of the material due to strain, the EBSD data must first be converted to a value for plastic strain (ε_p). The means of interpreting plastic strain form EBSD data has been a focus of interest since the automated indexing of EBSD data became available. Some of the most widely accepted ways of measuring strain have come through the use of Cross-Correlation techniques, with the most notable strides coming from work performed by A.J. Wilkinson[37] [38] [39]. The advantage of these techniques is the extremely accurate method of calculating local strain values from EBSD data. The drawback is the need for acquiring EBSD data from the same area before and after deformation in order to calculate the correlation between misorientation and strain. This type of technique is limiting in the industrial analysis setting due to the inability of most end users to have information about their material prior to processing.

A more direct approach would be to utilize empirically derived data and apply the equations that which correlate EBSD data directly to the strain information for materials. In previous work done by Kamaya et al. [40] an empirical correlation was made between the local plastic strain of steel at a given location and the local misorientation value at the same location. The equations derived from their experiments allow for the

calculation of local strain values from the local misorientation values obtained through EBSD analysis. This is done by use of the equation:

Eqn. 27 $$\varepsilon p = \frac{M_l - 0.1}{-0.0027d^2 + 0.041d}$$

where M_l represents the local misorientation value (degrees), and *d* refers to the step size of the EBSD scan itself. According to Masayuki Kamaya's experiments, there exists a linear correlation between local misorientation and plastic strain. The correlation between these two parameters becomes more linear as EBSD step size is decreased. Using d=0.25μm as a basis step size (EBSD scans performed for this experiment range in step size of 0.1 μm<d<0.25 μm), the above equation was applied to the data contained within the misorientation matrix given in Figure 24.

Although **Eqn. 27** given above was developed for 316 stainless steel the equation will be used for the 1018 steel coupons in this study due to the similarity of mechanical properties between 316 stainless steel and 1018 carbon steel.

For 316 Austenitic Stainless Steel;

Youngs Modulus(E_{316})=193GPa; 50% Reduction of area, 40% elongation

For 1018 Mild Carbon Steel;

Youngs Modulus(E_{1018})=190-210GPa; 48% Reduction of area, 27% elongation

By applying this equation to each individual point of a local misorientation matrix by use of our developed Matlab file *strained.m* attached in the appendix of this paper, a strain value can be assigned for each point within the scan area based on the plastic deformation of the crystalline lattice.

The strain data becomes important when applying it to mechanochemical equations proposed by Gutman for anodic dissolution of metals as given in the equation below. The applicable equation was used by Cheng et. Al [41] during the study of corrosion of X100 pipeline steel undergoing plastic strain. For the shift of electrode potential as a function of plastic strain:

Eqn. 28 $$\Delta\varphi = -\frac{TR}{nF}\ln\left(\frac{\nu\alpha}{N_o}\varepsilon_p+1\right)$$

where $\Delta\varphi$ is the change in potential (volts), T=300 Kelvin, R=Gas constant (8.314J/mol K), n=number of electrons transferred per redox reaction, F= Faradays constant (96,485C/mol), ν=0.45, $\alpha = 1.402 * 10^{11} cm^{-2}$. A value of N_o=1.078×10^{10} cm^{-2} is used for the surface density of dislocations for cold rolled 1018 steel which is similar to those obtained for type 304 cold-rolled steel by other groups[42], and represents an averaged value calculated empirically using our acquired strain values and rate of corrosion (AFM depth measurements) at several different locations, then using these values to solve for N_o using Equations 28, and 29 (given below). The electrochemical potential is then applied to the matrix of strain values to calculate the change in corrosion potential relative to the unstrained areas due to plastic strain, as seen in Figure 25.

The map suggest as much as almost 40 mV potential difference between the strained areas (dark blue) relative to the unstrained areas (light blue) where dark blue areas (strained areas) are more active than those that are not strained. This galvanic potential is the driving mechanism of the corrosion in the strained areas. The approach

to calculate change in corrosion current uses an equation from Cheng (derived from Gutman), assuming constant bulk cathodic current density:

Eqn. 29 $$\Delta I = \Delta i_a = i_{ao} e^{\frac{|\Delta\varphi|}{b}}$$

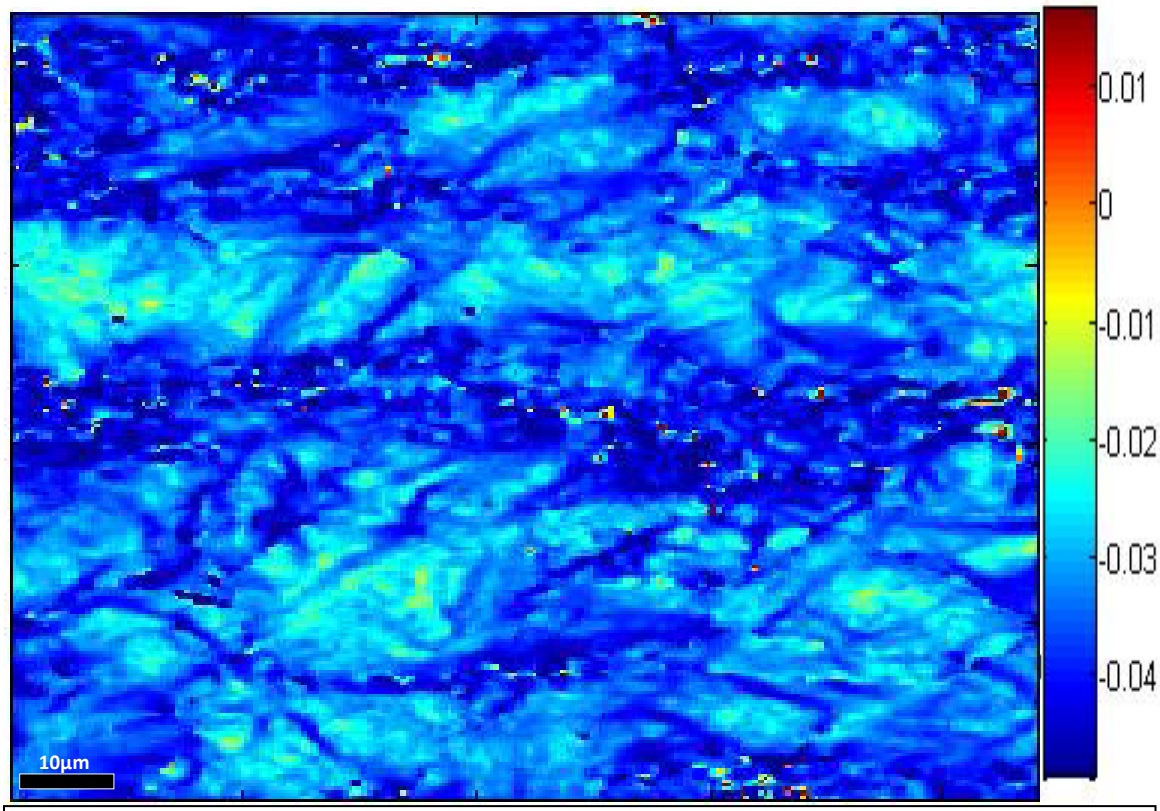

Figure 25. Change in Anodic equilibrium potential (V) as a function of plastic deformation.

where ΔI represents the change in overall current density, Δi_a represents the change in anodic current density, i_{ao} is the standard corrosion current density obtained from the corrosion resistivity of the unstrained steel. Eqn. 29 is equivalent to amount of current one would get if we applied a $\Delta\varphi > 0$ potential above the corrosion potential and observe the additional current density relative to the corrosion current density of the

unstrained steel. The implications of this are extremely important: this suggests that any local strain in the carbon steel creates a localized galvanic cell driving the local corrosion at that location. From Eqn. 29 it is clear that $\frac{\Delta I}{i_{ao}} = e^{\frac{|\Delta\varphi|}{b}} \cong e$ for $\Delta\varphi \approx b \approx 0.06\,V$. This means for 60 mV excess potential the corrosion current increases nearly by a factor of three relative to the standard corrosion current density.

Plotting the change in both current density and equilibrium potential as a function of strain using the equations shown above helps to illustrate the expected effect of strain upon the surface of the sample. Figure 25 shows a plot of these relationships. This plot reveals the continual increase in the corrosion current density as a function of plastic strain, and hence the change in the equilibrium potential towards the more active region (negative). Implication of this data is remarkable: As mentioned above a relative change of 40 mV (0.04 V) between a grain that is less strained and a grain that is more strained contributes $\Delta I = 5x10^{-6}\ A/cm^2$ of current to the corrosion processes where we assume i_o =2.337*10^{-6} A/cm^2. This is an additional (see Formula 22 in Chapter 1) corrosion rate of about 1.16x10^{4}* ΔI = 5.82x10^{-2} mm/year or 58 µm/year accelerated corrosion rate compared to the overall corrosion. This almost doubles the corrosion at that anodic location. Obviously if the i_o was larger the excess corrosion would have been proportionally larger.

Information obtained from polarization resistance (corrosion resistivity) measurements provided approximate values for the corrosion current density as

explained in Chapter 1. For this study we obtained a corrosion current density of about i_o =1.592×10^{-6} Amps/cm^2 and corrosion potential of E_o = *-0.525 V*.

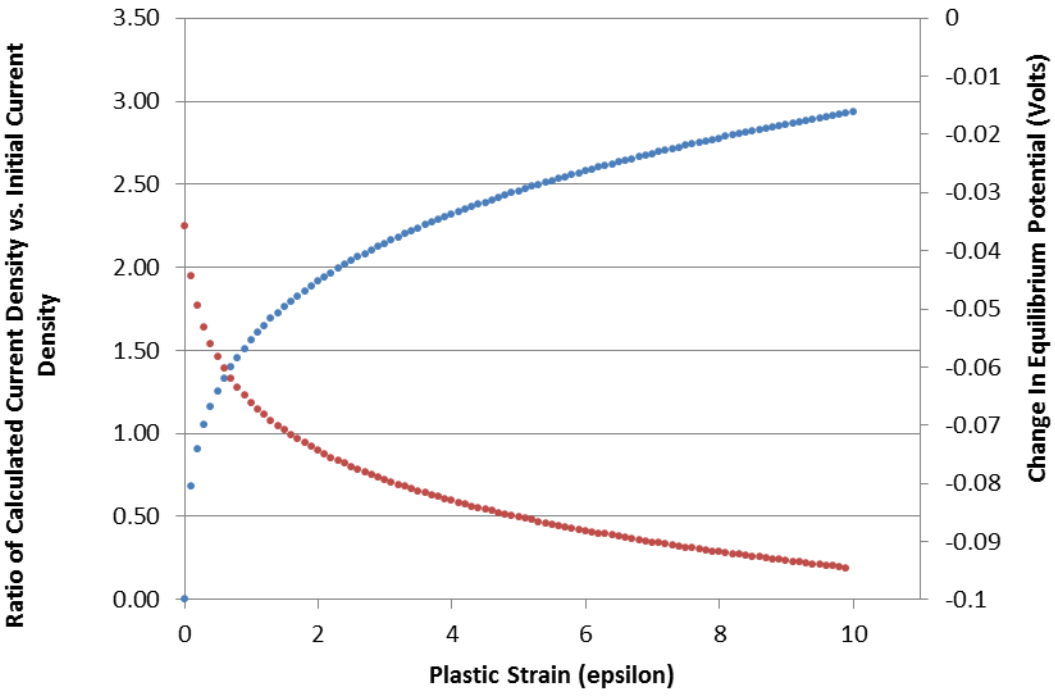

Figure 26. Plot of the change in corrosion current given as $\Delta I/I_o$ (Blue) and equilibrium potential change (Red) as a function of plastic strain using mechanochemical equations.

A similar value for corrosion current densities is reported in similar experiments [31]. As discussed in Chapter 1, the Tafel slopes cannot be obtained reliably from our Tafel plots hence we used an approximate value of b_a=0.06 V in our estimations of corrosion rates by taking into account similar values in the literature. The Tafel plot associated with this experiment is shown in Figure 27. In the inset it shows the linear behavior of the $\Delta\varphi$ vs. *i* plot near the corrosion potential E_o from the slope we obtained the corrosion resistivity

R=8.037×10^3 Ohm-cm^2. The anodic corrosion current was obtained using Formula 21 in Chapter 1 to be 1.592x10^{-6} Amps/cm^2.

A plot of the change in corrosion current density in terms of $\Delta I/i_o$ is shown in Figure 28. The corrosion current measured in the highly corroded (red) areas corrode at a rate of approximately twice as fast as those locations showing the least amount of strain.

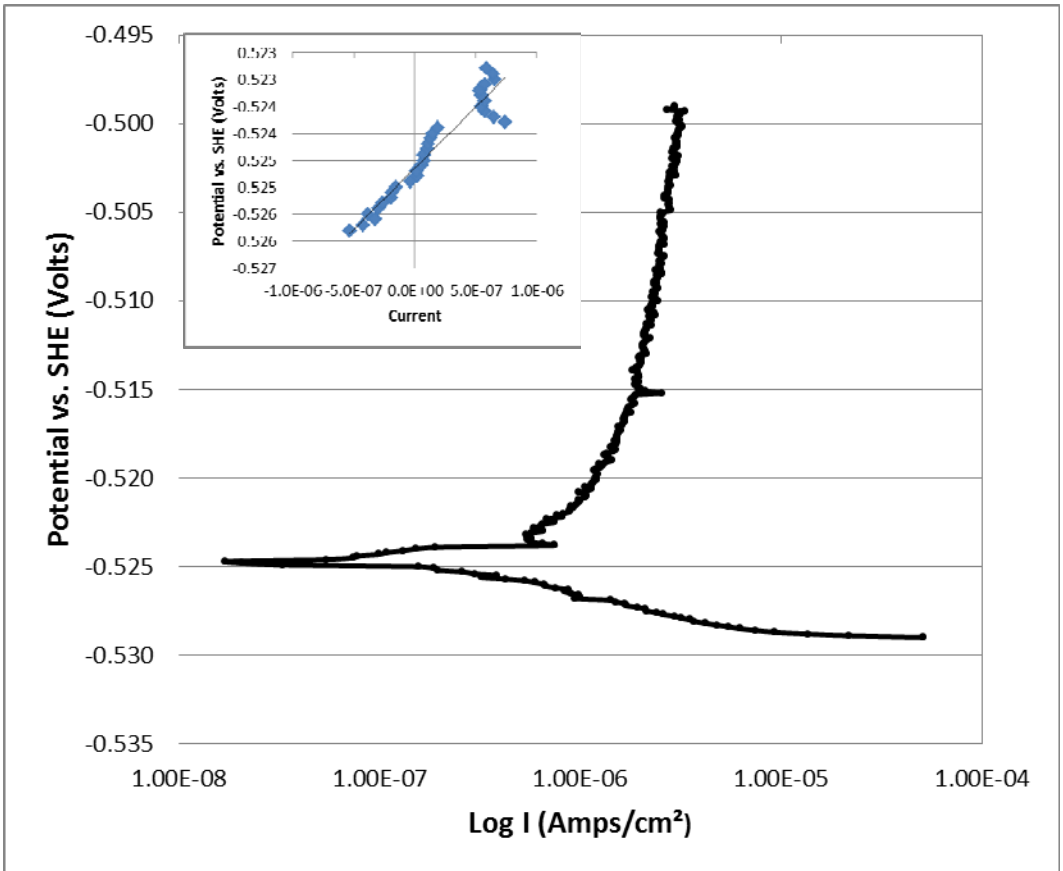

Figure 27. Electrochemical polarization resistance measurement taken at the initial point of exposure for a 1018 steel coupon in anaerobic ALDC media.

The corrosion rate can be obtained from Equation 22 in Chapter 1:

Eqn 30. $$Rate\left(\frac{mm}{yr}\right) = 1.16 * 10^4 i_o$$

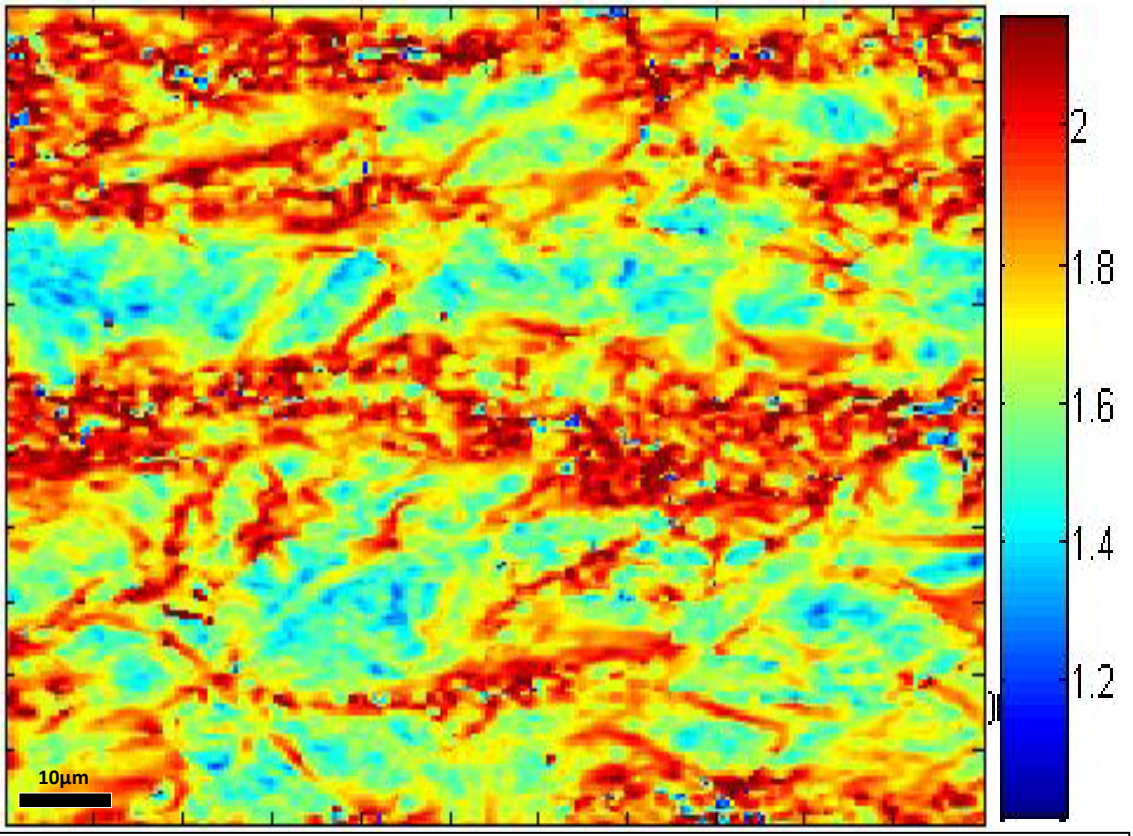

Figure 28. Plot showing the ratio of $\Delta I/i_o$ as a function of strain and location. Red areas represent those with the highest increase in current density, while green areas represent areas with less increase of current density.

where i_o is the corrosion current density in A/cm^2. For the current density measured above, the formula yields a corrosion rate of ~ 0.018 mm/year.

The translation of data from strain to corrosion rate in terms of mm/year, shown in Figure 29, is extremely valuable, because the predicted corrosion rate data acquired from the calculation shown above using EBSD local-misorientation information can now be quantitatively compared to measurements acquired through AFM surface

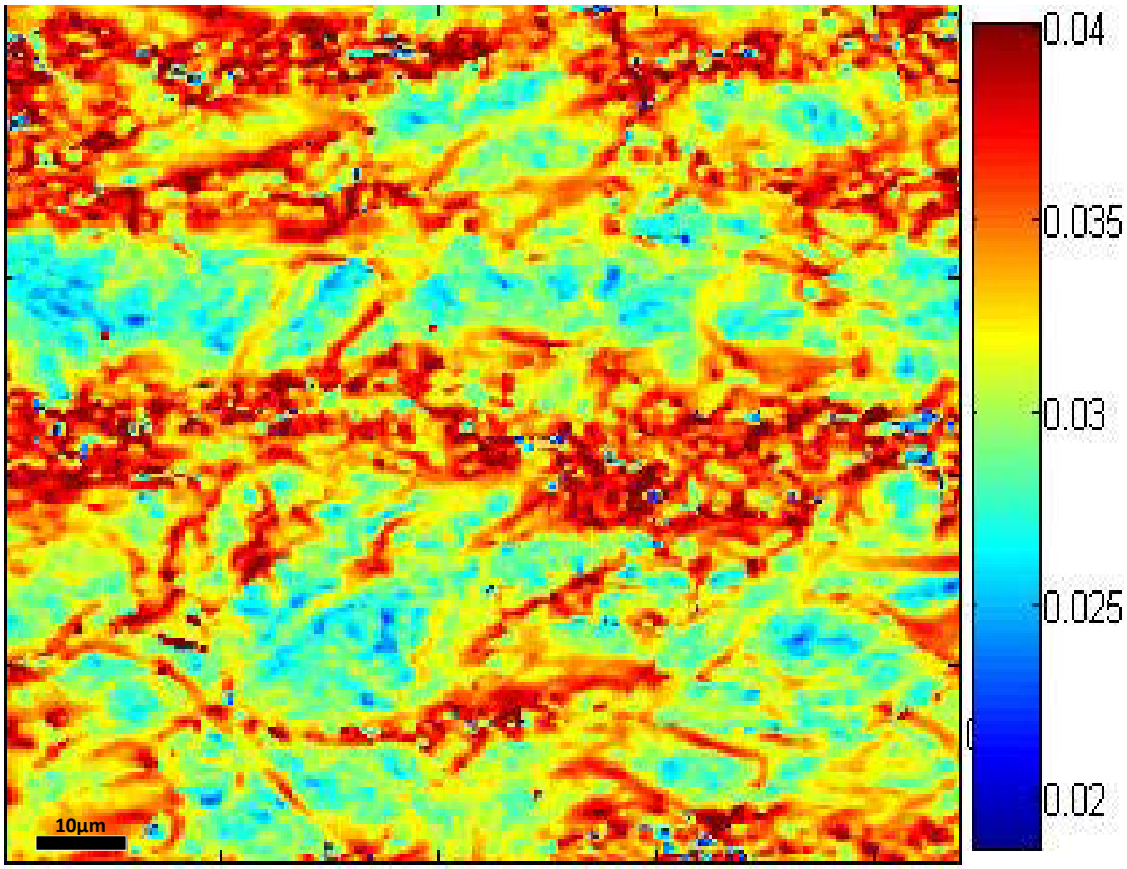

Figure 29. Predicted relative corrosion rates in mm/year as a function of position on the surface of the corroded and strained carbon steel. Red areas represent the highest corrosion rate, while green areas represent areas with less corrosion.

topography. These two data sets can be further used to assess the predicted amount of iron dissolution to the measured amount of dissolution.

Comparison with the AFM
Correlation Measurements

An AFM scan was taken of the exact same area after exposure to the sulfide media, and is seen in the left image of Figure 30. The line in the image shows where the line profile of the surface topography was acquired in order to provide the measured

surface topography information. Predicted surface topography was obtained from a line-scan taken through the same area of the local misorientation data. Points A, B, C, and D in Figures 30 represent corresponding data points to compare the measured and predicted values.

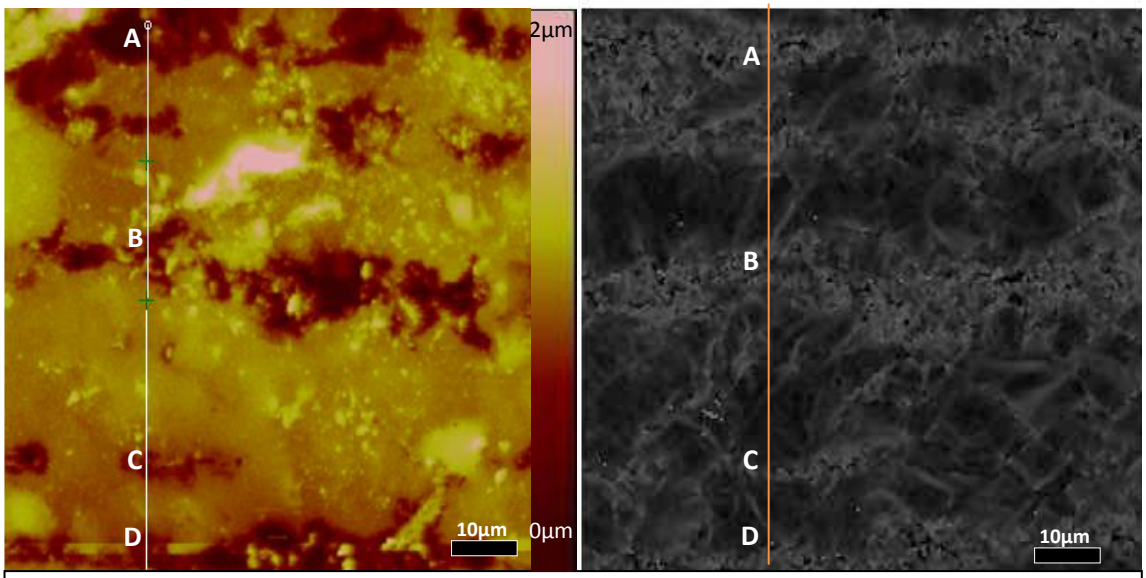

Figure 30. The image on the Left is an AFM scan taken of the parallel cut coupon after exposure to 14 days in ALDC environment. The image on the right shows a local misorientation map corresponding to this area prior to exposure.

Comparison of the actual depths to the predicted values at points A,B,C, and D reveal that predicted corrosion rates agree with the observed data within better than 27% accuracy as shown in Table 2. For example, the predicted value of corrosion depth at point A is within 3.4 % of its observed value. Similarly, the corrosion rates predicted by the model for points B, C and D agree within, respectively, 9.3, 7.8 and 16.3 % accuracy with the measured values.

This is an important result because it shows that through the utilization of EBSD, AFM surface measurements, mechanochemical principles, and electrochemistry, the amount and location of accelerated dissolution of 1018 steel can be predicted before exposure to a corrosive environment.

Location	Predicted Depth	Measured Depth (μm)	Error (%)
A	0.4942	0.512	3.4
B	0.4795	0.529	9.3
C	0.4912	0.533	7.8
D	0.5702	0.681	16.3

Table 2. Values obtained from AFM surface analysis (measured) and analysis using EBSD strain information (predicted) and the calculated difference in depth measurements at the same locations from both data sets.

The results were verified through analysis on other spots of the parallel cut coupon. The binary images of one of these locations are displayed in Figure 31, along with the results of the overlaying of these two images. Just as in the analysis for the previous location, the information obtained from AFM surface analysis and EBSD local misorientation analysis were changed to grayscale and overlaid to allow for visual inspection of those regions of overlap. Analysis reveals that once again areas of increased anodic dissolution of the 1018 steel correspond to areas of increased strain.

Mechanochemical analysis was again performed using the Matlab file *strained.m* by applying the equation given by Masayuki Kamaya to obtain strain values from the local misorientation information, followed by application of the mechanochemical

equations. The results again show that the anodic potential becomes more negative in regions of increased strain represented by regions of dark blue in Figure 33, an increase in corrosion current represented as red regions in the image on the left side of Figure 32, and ultimately an increase in anodic dissolution of 1018 steel in a form of mm/yr represented by red regions in the image on the right side of Figure 32.

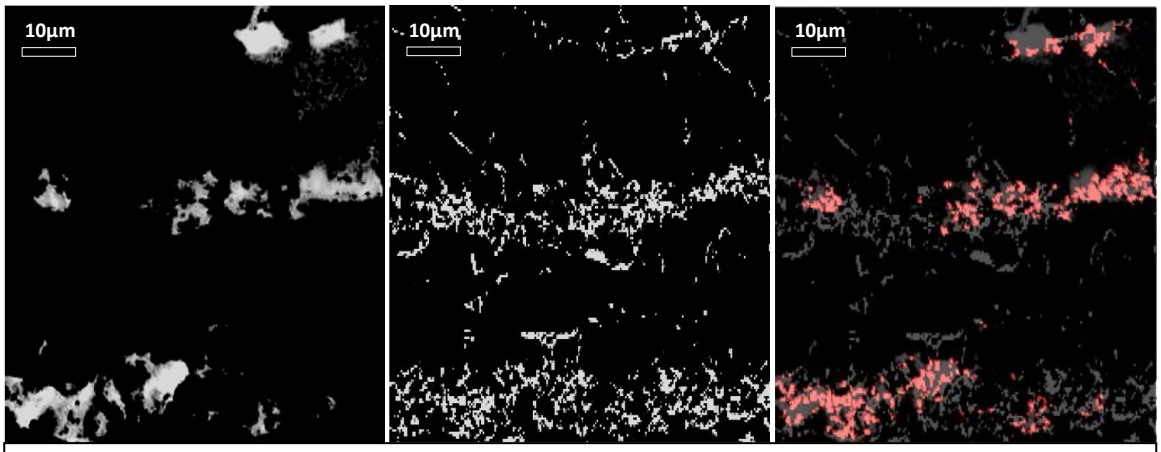

Figure 31. Image comparison of A) an AFM image taken of a location after corrosion. B) The strain map of the same location. C) A Matlab created image overlay of the two images with areas of intersect highlighted in red.

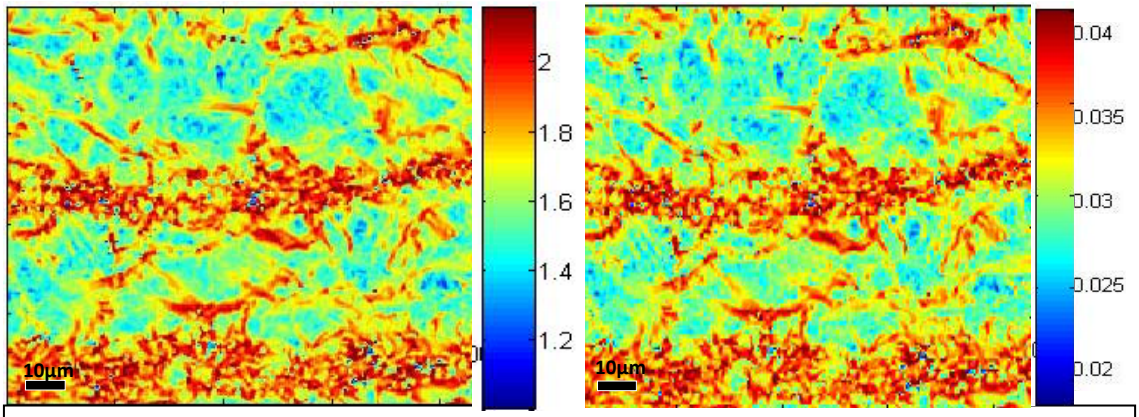

Figure 32 Predicted change in current density as a ratio of $\Delta I/i_o$ as a function of position and strain on the corroding surface (Left), and the predicted change corrosion rate (mm/yr) as a function of position on the strain on the corroding surface (Right).

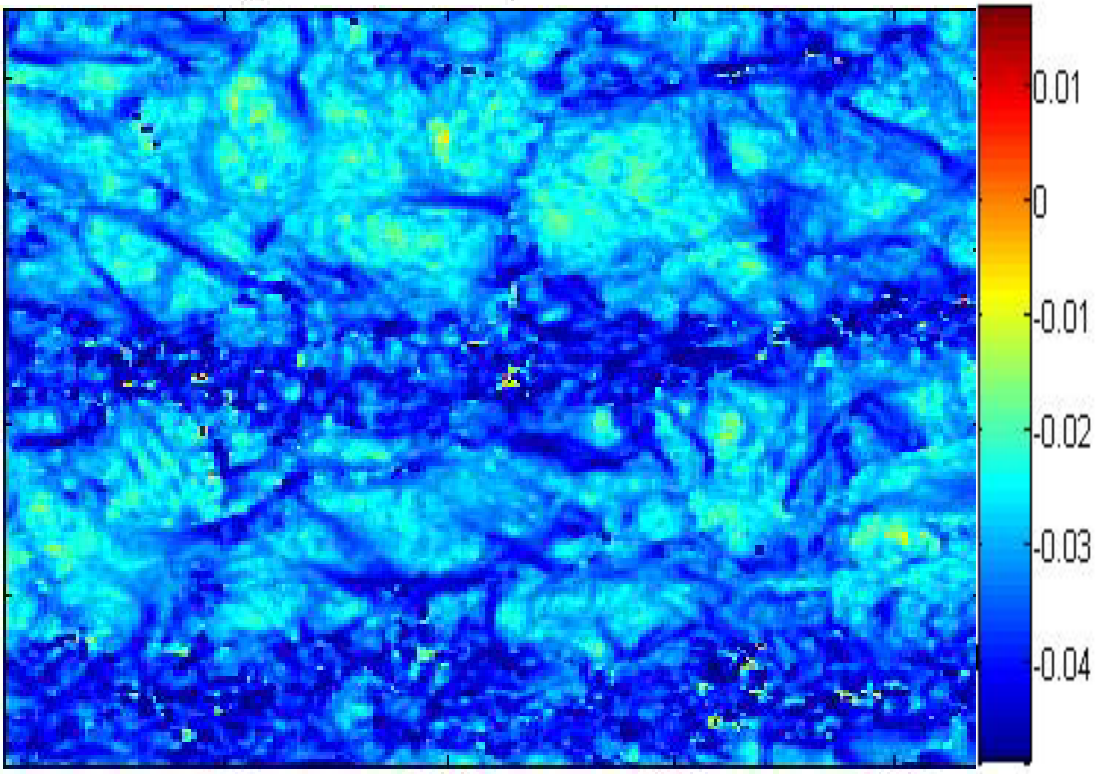

Figure 33. Predicted change in anodic equilibrium potential (Volts) as a function of position on the strained and corroded surface

AFM surface analysis of the same area after exposure, shown in Figure 34, reveals accelerated corrosion in areas categorized by increased plastic deformation. Data analysis of both the AFM data and the predicted corrosion rate using mechanochemical principles is shown in Table 3. Comparison of measured values acquired through AFM surface analysis and predicted values are within the same order of magnitude as discussed in relation to data presented in Table 2. The source of all of our errors likely relate to the inability to accurately determine the Tafel slopes associated with the anodic and cathodic branches of the resistance plots.

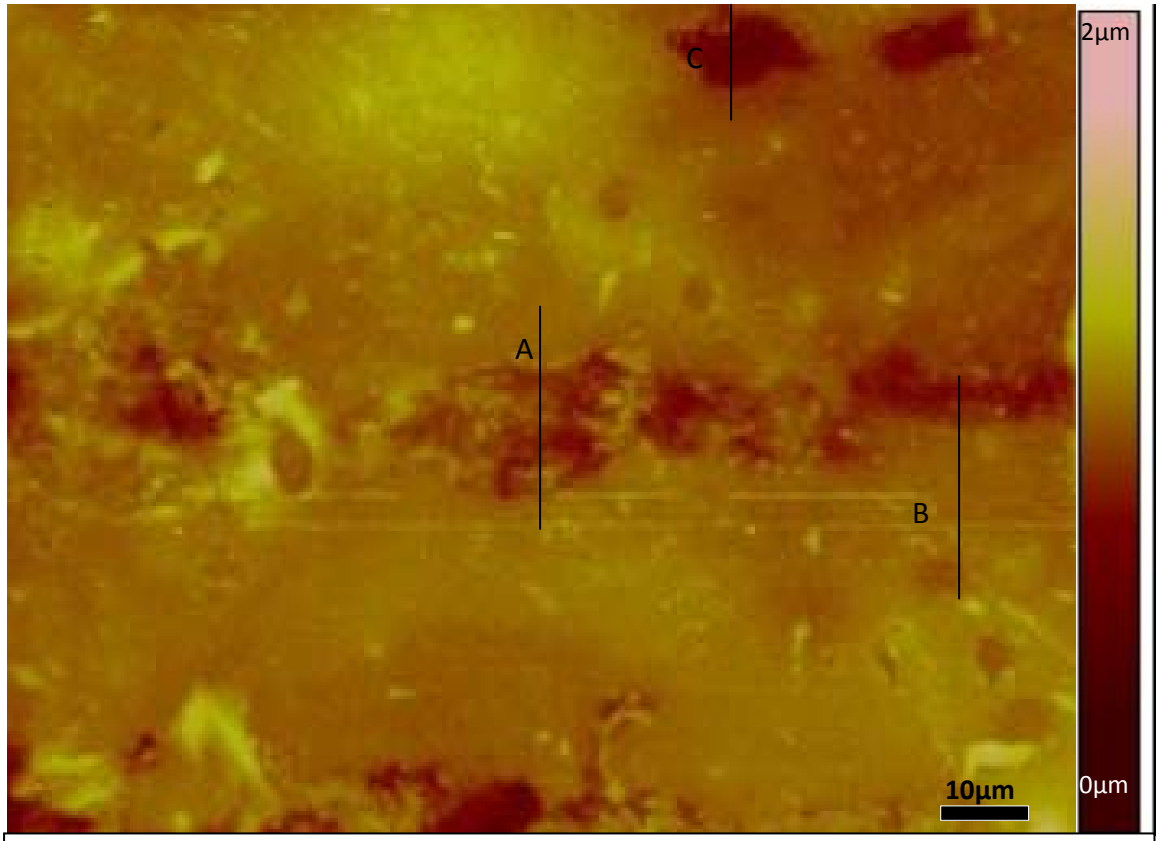

Figure 34. An AFM image taken of the parallel coupon after 14 days of exposure in ALDC media. Image corresponds to the same location shown in Figures 30-33.

Location	Predicted Depth	Measured Depth (µm)	Error (%)
A	0.394	0.49	19.5
B	0.319	0.311	2.57
C	0.4263	0.415	2.72

Table 3. Values obtained from AFM surface analysis (measured) and analysis using EBSD strain information (predicted) and the calculated difference in depth measurements at the same locations from both data sets

As mentioned earlier, the reason for this is the onset of the diffusion limited currents in our Tafel plots.

The information from Figure 35 shows that the AFM surface data obtained from three line scans taken across the same area shown in Figures 31-34, corresponding to the parallel cut coupon show a very drastic change in surface topography in areas far from the highly strained areas, as compared to those areas of high strain. Analysis of the three line scans taken across the area show large surface topography amplitudes for the top and bottom lines, which are in areas of high strain, while the center line shows minimal topography amplitude compared to the other two. In fact, the areas far from strain show only tens of nanometer surface topography difference, while those that are highly strained show several hundreds of nanometer topography difference.

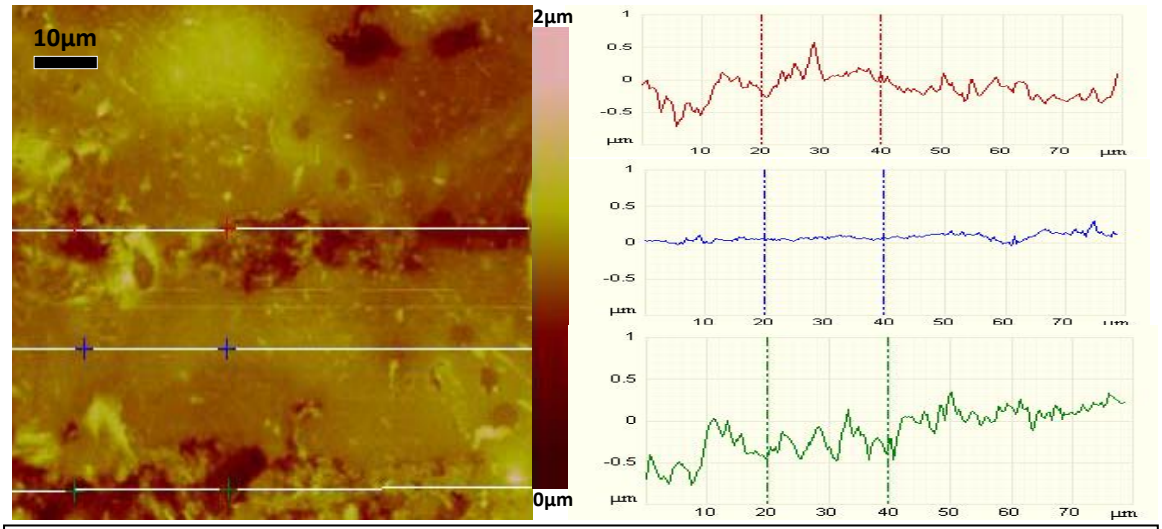

Figure 35. A) An AFM surface image showing three line positions, and B) their corresponding height data.

This is significant due to the fact that the predictions are several hundred nanometers in size, which is similar to the measured values. Ultimately this leads to the conclusion that the agreement between the predictions and the measurements would not simply happen by chance, but rather that it does in fact make an accurate suggestion that strain is a dominating factor in the rate of anodic dissolution of a coupon cut parallel to the rolling direction for 1018 steel under the given conditions.

A third location of the same coupon was analyzed using EBSD and FEM imaging only. Using the same correlation made at the previous locations, Figure 36 readily shows that in areas of increased local misorientation values represented by red colored regions in the EBSD map on the right, there is a corresponding increase in anodic dissolution of the metal represented by dark regions in the FEM image on the left. The simple, and quick, type of analysis lends itself to functional use in the industry as a predictive tool that can be utilized for materials analysis prior to exposure to a corrosive chemical environment. In particular, the predictive value of this technique is of importance in analyzing samples for potential sites of pitting, as well as when comparing one type of steel to another for quality assessment purposes.

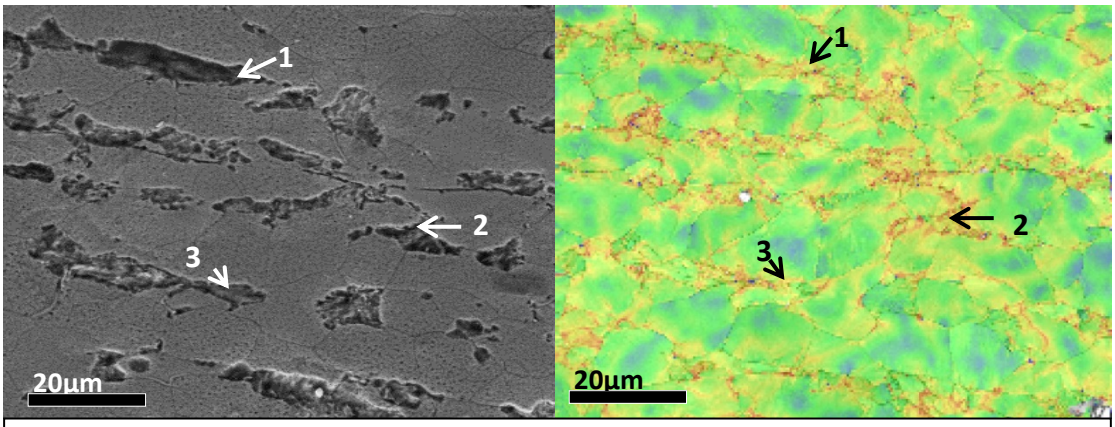

Figure 36. FEM image(Left), and Strain Map (Right) of the same area of a parallel coupon after corrosion in ALDC environment. Arrows represent the same 3 locations in both images.

Besides issues associated with the accurate determination of the current density, other possible explanation factors for the differences between the model and the measured values are the assumptions made for the model; that the cathodic processes in the environment are constant. This assumption is required to establish the change in anodic equilibrium potential as a function of strain only. In actual experiments the overall corrosion rates change as a function of ion concentrations in solution, such as Fe^{2+}, and HS^{-}, as a function of changes in pH of the system during exposure, and also due to the presence of passivation layers that may have an inhibiting effect due to their presence on the surface of the steel[21]. However, as a whole the model appears to be satisfactory.

Pitting On Parallel Cut Coupons

One of the major forms of destructive corrosion seen in industrial application of steel is the process of pitting. During the pitting process, accelerated corrosion is

concentrated in one, often circular, area. One form of pitting which initiates at MnS inclusions[43] proceeds by forming a small area of influence encircling the inclusion. Several mechanisms serve to accelerate the corrosion around this inclusion to form the pit including strain between the surface of the inclusion and the ferrite ion, changes in pH, surface charge such as Cl^- ion concentration on the surface, and creation of active and passive layers in or near the pitting area[44]. According to Melchers[45], large pits are believed to form as a result of smaller pits coalescing into one large pitted area. Figure 37 helps to support this theory. In this figure the strained lines seen as bright red in Figure 37.B resulted in dissolution of metal in the same areas after exposure to the ALDC sulfide environment. The image seen in Figure 37.C suggests that the corrosion occurring between the lines occurred first, and the growth is beginning to occur just around the initial seed established by the initial corrosion process driven by strain.

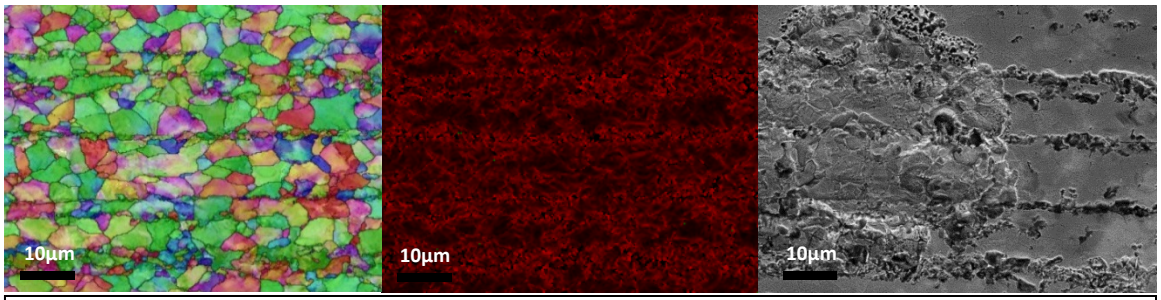

Figure 37. A) Orientation and Band Contrast. B) Strain Map. C) Pit alongside parallel corrosion bands.

EBSD Analysis of a Perpendicular Cut Coupon

The same analysis as described in the previous sections for a parallel cut coupon was also applied to a perpendicular cut coupon. The local misorientation data was interpreted in the same way as for the local misorientation map of the parallel cut coupon; blue and green correspond to low lattice strain while orange and red corresponds to high lattice strain. Figure 38 shows an FEM image of a location prior to exposure in the left image, after exposure in the center image, and the EBSD local misorientation map of the same location shown in the image on the right. Visualizing the change in orientation that occurs as a function of position along a specific axis may help to fully understand the concept of strain within the material. Figure 39 illustrates this where the relation between position, orientation, and strain are shown.

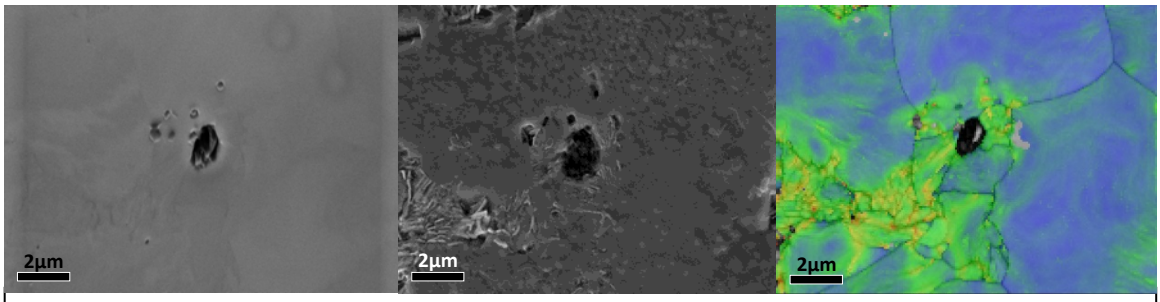

Figure 38. FEM images showing a location before and after corrosion and the corresponding strain map of a coupon cut and polished perpendicular to rolling.

Enlargement of an area, distinguished by the black box given on the map, is seen in Figure 39.B, which shows a map along the horizontal axis of the selected area, and the local misorientation value along the axis designated by the color scale.

Using the crystal display function of the HKL software similarly to the parallel coupon provides 3-dimensional images of the detected grain orientation at a point on the map. The area encompassed by the black box in Figure 39A is enlarged and displayed in Figure39.B. Visual inspection shows that there is a correlation while moving position from left to right within the designated area with the displayed 3-dimensional cubes given on the right side of the figure. Strain amount is very low at areas shown as blue, while these values increase to highly strained when moving towards points the left of the area of concern. By looking at the provided orientation of the BCC iron along this same motion, the orientation changes very little in areas corresponding to low (blue) strain, while the orientation changes rapidly in the area of high (orange) strain.

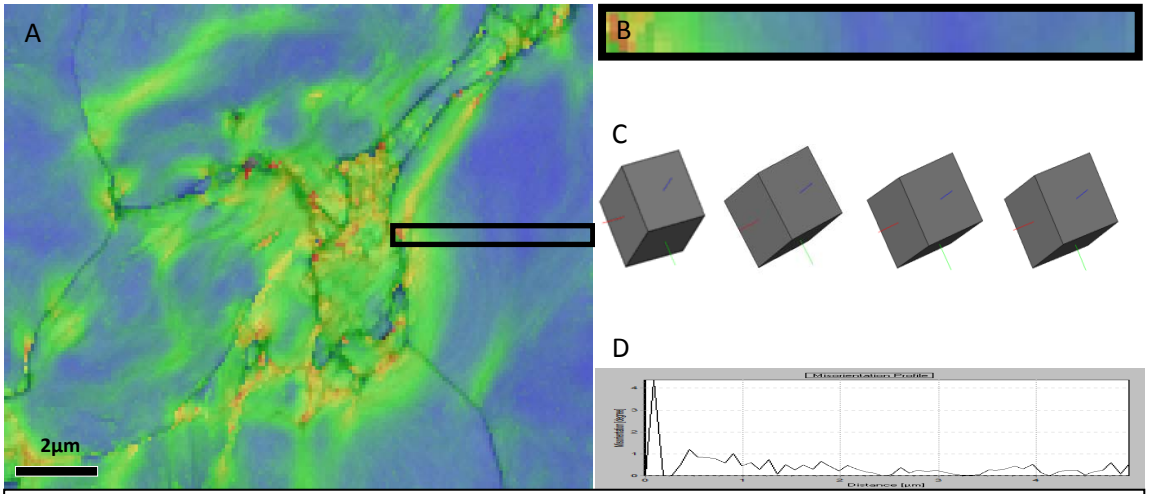

Figure 39. A) EBSD local misorientation map of an area on a perpendicular cut steel coupon with area of interest enclosed inside of the black rectangle. B) Area of interest expanded for better visual observation. C) Iron cubic cell orientations along the area of interest. D) Plot of the local misorientation value as a function of position measured horizontally through the area of interest.

Further analysis given in Figure 39D shows the calculated misorientation profile given by the HKL software along a line created through the same area. The misorientation profile illustrated both with variations in the color, as well as the orientation change of the BCC iron, as a function of position horizontally across this area.

Electrochemistry of a Coupon Exposed to Anaerobic ALDC Culture

As mentioned before, there were two types of environments for the ALDC culture experiments. One of them, shown in the previous section, was considered a sub-oxic environment due to the low level presence oxygen. Another experiment was performed using the same reactor setup; however the conditions were performed in a strictly anaerobic environment. To ensure anaerobic corrosion only, the reaction vials were assembled in an anaerobic glove box with a nitrogen gas atmosphere. They were then removed from the glove box and purged with a gas flow of 5 % CO_2, 4.97 % Hydrogen, and balance nitrogen at a flow rate of 10 liters per minute for 15 minutes. After purging, the vials were returned to the glove box immediately. The entire preparation process occurred with a capped and crimped vial to ensure no entrance of oxygen was possible throughout the procedure.

Electrochemical measurements were taken at the beginning and end of the experiment to establish changes in open circuit potential, and also to monitor any change in the slope of the anodic and cathodic curves. The results are shown in Figure-

40. There was an increase in open circuit potential equal to 132mV from the beginning of the experiment to the end of the experiment. The overall shape of the slopes for both circumstances is indicative of an environment that would cause passivation of the sample, confirmed by the slow increase in the anodic current with increasing potential.

Corrosion resistivity measured from the slope of the voltage vs. current near the corrosion potential gives a large value $R=1.55x10^{5}\ Ohm\text{-}cm^{2}$ which yields a small corrosion current density of $i_o=8.26x10^{-8}\ Amps/cm^{2}$. This suggests a protective Fe sulfide on the surface preventing anodic and cathodic processes.

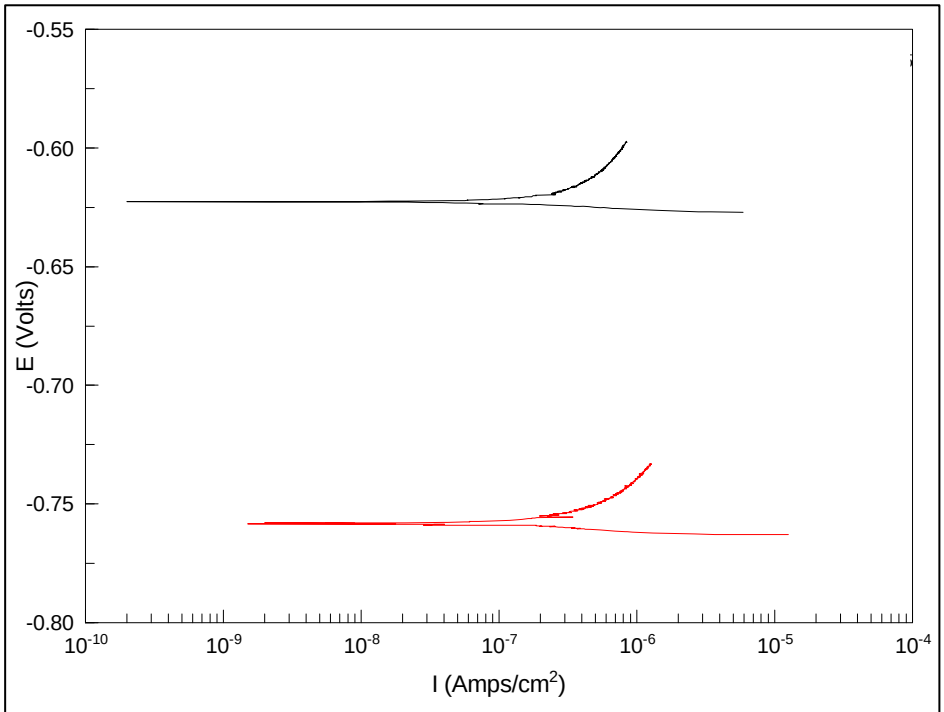

Figure 40. Tafel plots taken at the beginning (red) and end (black) of the Anaerobic ALDC experiment. Potential values are measured vs. Ag/AgCl

Further analysis was performed at the end of the experiment through use of a more broad change in potential during polarization measurements of the system, shown in Figure 41. The inset in Fig. 41 shows the zoomed in behavior of E vs. i near the corrosion potential (near minimum current) from which we obtained the corrosion resistivity which led to the corrosion current density of $i_o=8.26x10^{-8}\ A/cm^2$. This value can be contrasted with the traditional way of obtaining this current. As mentioned in Chapter 1 we expect to get a wrong result through traditional analysis even though low current densities are favorable of conditions leading to diffusion limitations.

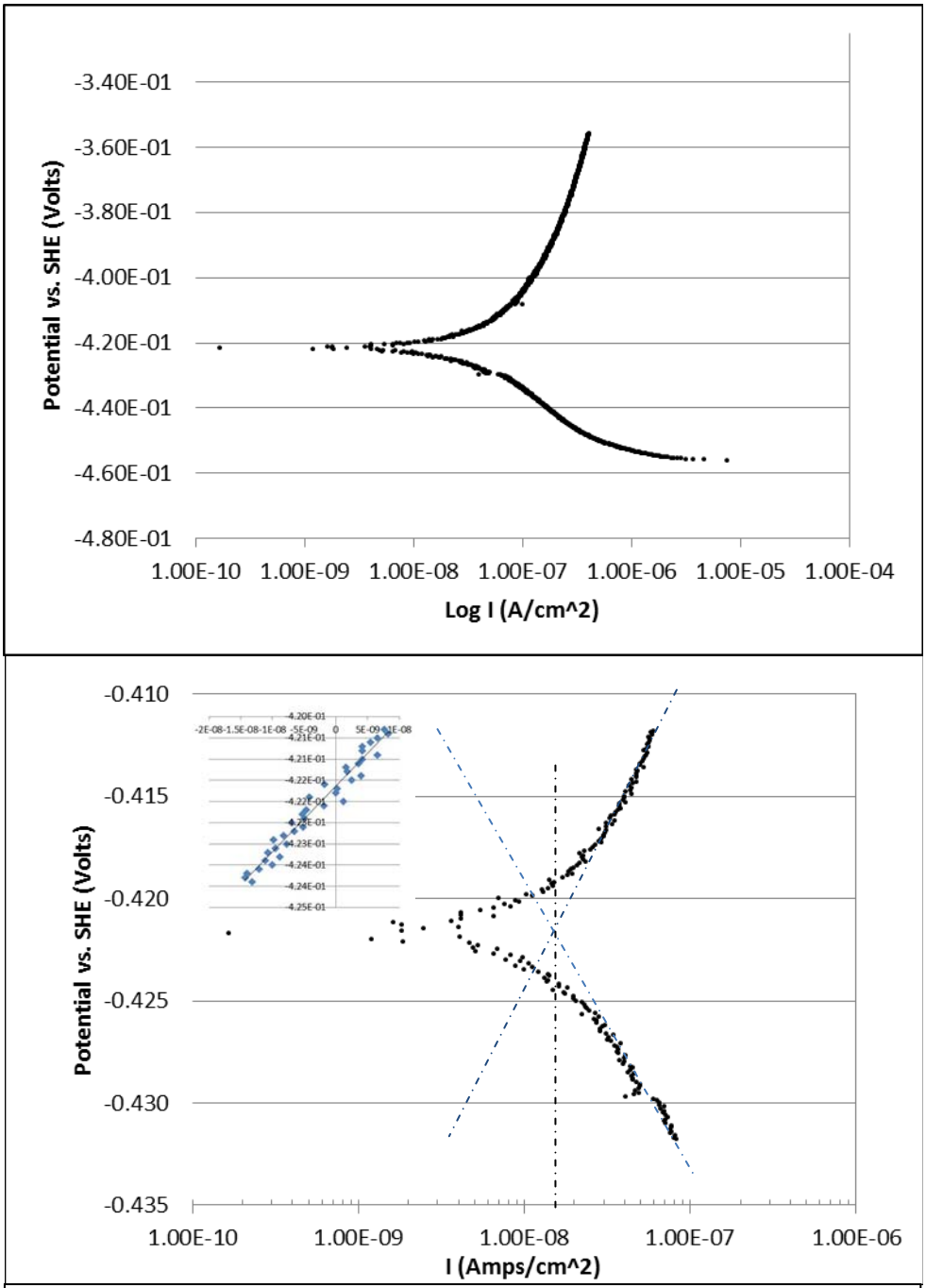

Figure 41. Tafel plot taken immediately after initial exposure of a 1018 steel coupon exposed to anaerobic ALDC media (top), and the same data magnified to identify the corrosion current density and Tafel slopes, seen as black and blue dashed lines respectively (bottom). Inset shows E vs. I plot taken near the corrosion potential, which is used to obtain the corrosion resistivity R.

In using the traditional method, this current is obtained by intersections of the Tafel slopes of the anodic and cathodic curves from which b_a and b_c can be calculated to yield 0.013 V and 0.011 V, respectively; these are shown as the dotted lines drawn tangent to the anodic (upper) curve and cathodic (lower) curve. The corrosion current density $i_o = \frac{1}{R} \frac{b_a b_c}{2.303\,(b_a+b_c)}$ for the system was calculated to be i_o~ 3*10^{-8} Amps/cm^2, whereas the i_o obtained from the intersection gives i_o~ 1.2*10^{-8} Amps/cm^2. In fact, the true value is $i_o = \frac{1.28\times10^{-2}}{R} \cong 8.3*10^{-8}\ Amps/cm^2$ obtained as outlined in Chapter 1. The potential was referenced to the standard hydrogen electrode (SHE) in Figure 42 to provide information about the state of ion concentrations in solution by using thermodynamic equilibrium equations cited in Chapter 1. The disagreement between corrosion currents obtained from the Tafel slopes, compared to those obtained using $i_o = \frac{1.28\times10^{-2}}{R}$ is not surprising. Despite the low current densities involved in these measurements the onset of the diffusion limitation prevents us from obtaining correct values for b_a, b_c and i_o. Even under the most favorable conditions this approach still gave a factor ~7 times less current density than the actual value. This error would be even larger for those systems characterized by higher corrosion current densities.

As mentioned previously, the use of Pourbaix diagrams can yield insight into the corrosion processes taking place within the system. The equilibrium potential of the system begins at -0.550 Volts and finishes at -0.426 Volts. The system was originally at a pH of 7.5, and underwent little changes in terms of pH.

Correlation of the initial open circuit potential of -0.550 Volts to the Pourbaix diagram for a simple anaerobic sulfide environment suggests that Mackinawite was the most probable iron sulfide deposition upon the surface of the steel initially. At the end of the experiment, the open circuit potential approached -0.426 Volts, which approaches the equilibrium line between Mackinawite and Greigite at pH of near 7.5. It is theoretically possible that some of the corrosion deposits on the surface underwent transformation to the Greigite phase.

Past studies have shown that at low dissolved sulfide concentrations, small exposure times, more negative equilibrium potentials, and pH>5, Mackinawite is likely to form a weak passivation layer[46]. At longer exposure times, pH>5, and higher equilibrium potentials Mackinawite likely converts to Greigite and pyrite, which have a greater inhibiting effect compared to Mackinawite. At low sulfide concentrations this process can occur with minimal corrosion taking place, creating an environment that is likely to inhibit the corrosion of steel throughout the entire exposure period[46]. Due to the low amount of corrosion seen in the purely anaerobic experiment, it is at least possible that the steel underwent a passivation that inhibited it from corroding as quickly as we observed in the sub-oxic experiment.

Anaerobic Indonesiensis Culture Experiment

Another bacterium of interest in sulfide corrosion of steel is *Desulfovibrio Indonesiensis*. This experiment was carried out in two phases. In first phase of this

experiment, the coupons were analyzed using FEM, EBSD, and AFM analysis in the same way as the two prior experiments. The Samples were first exposed to an Indonesiensis culture in the anaerobic chamber and allowed to corrode for two weeks. Electrochemical measurements were taken during the process and FEM analysis was conducted on the coupons after the exposure. Results from the first phase showed very low corrosion rates upon the surface of the sample, with minimal amounts of iron sulfide development on the surface. It was believed that the bacteria were potentially in a dormant phase in the culture media, or essentially at a low state of metabolic activity for the reduction of sulfate to sulfide. In order to test this hypothesis, a new technique was utilized that would take advantage of the metabolic activity of growing organisms. During this process, the coupons were exposed to a solution containing 4 ml of growth media and 1 ml of culture media. Solution samples were taken from the experiment vials at several points throughout the experiment to measure the reduction of sulfate to sulfide. The increase in sulfate reduction is one of the accepted ways for measuring the activity and growth of SRBs, so a decrease of sulfate concentration would indicate an increase in the SRB activity, and hence an increase in sulfide in the container.

The predicted change of anodic potential of the coupon due to local misorientation was calculated through Matlab analysis using the *StrainedIndo.m* file, which I developed as part of this work. This file uses the same mechanochemical analysis as results shown for previous experiments; however the StrainedIndo.m file utilizes electrochemical values that correspond to corrosion in an indonesiensis

environment. These electrochemical values were obtained from polarization resistance data which are represented in the Evan's diagram shown in Figure 42. The accompanying corrosion values obtained from curve fitting of the diagram gives the following values for the electrochemical system:

Initially,

$i_{ao} = 1.687 * 10^{-6} A/cm^2$, and E_o=-0.552 Volts SHE.

After 25 days of exposure, $i_{ao} = 1.555 * 10^{-7} A/cm^2$, and E_o=-0.565 Volts vs. SHE.

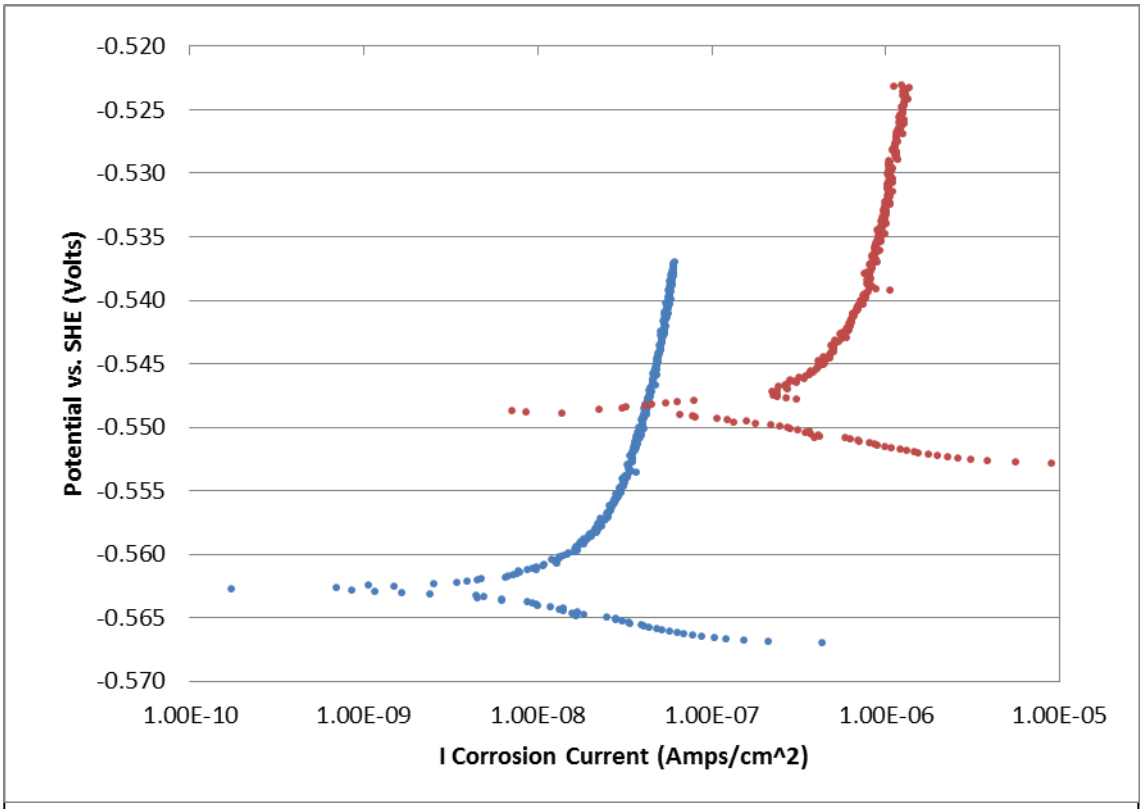

Figure 42. Evans diagram showing the polarization resistance data for 1018 steel coupon exposed to indonesiensis culture in Widdel media. The red curve was taken at the beginning of the experiment, and the blue curve was taken at the end. Potential values measured vs. SHE

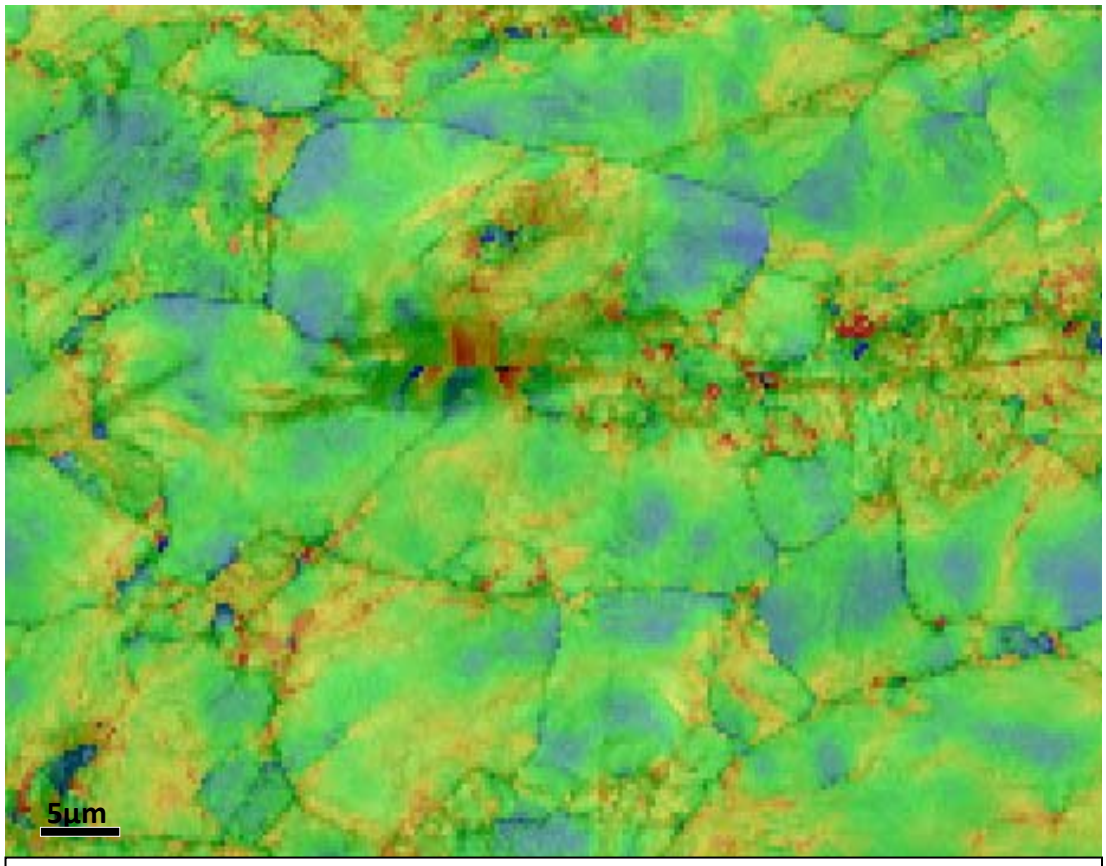

Figure 43. A Local misorientation map from EBSD data of a location on a parallel cut coupon before exposure to corrosion in an *Indonesiensis* environment. Blue/green represents lower strain while Orange/Red represents the areas of higher strain. Band Contrast has also been shown in the picture for easier viewing of the grain boundary

The local misorientation map data shown in Figure 44 provided values needed for calculating the change in anodic potential as well as corrosion rates seen in Figure 45A and Figure 45B respectively. Comparison of the predicted values for the corrosion rates between this environment and the ALDC environment from previous experiments reveals a much lower rate of corrosion. The anodic potential changes according to strain values are similar between the *Indonesiensis* environment and the ALDC environment;

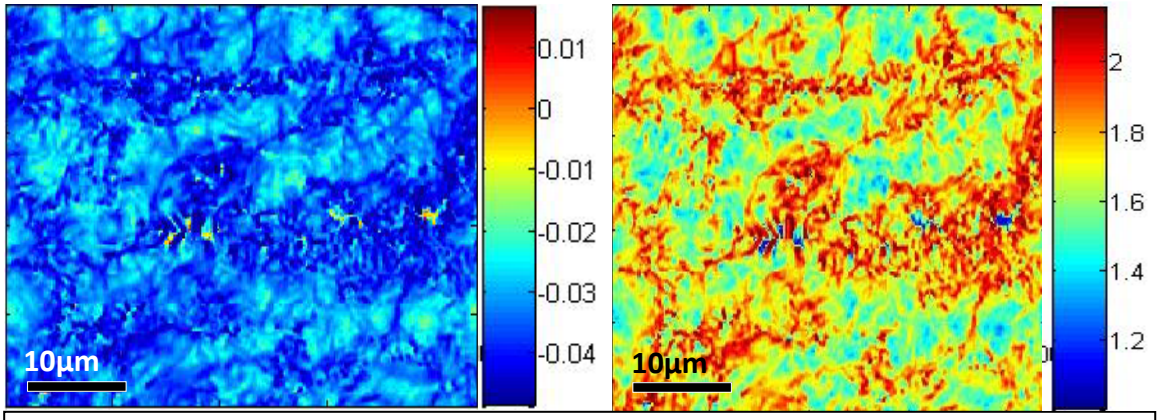

Figure 44. A) Calculated change in anodic equilibrium potential (Volts), and B) the ratio of the change in corrosion rate over the initial corrosion rate ($\Delta I/i_{o)}$ from EBSD acquired strain information.

however the change in corrosion rate is much lower. The lower change in calculated dissolution rate is due to the much lower i_o value for this experiment compared to that of the ALDC experiments. Due to the nature of the mathematical equations used for the analysis, specifically **Eqn. 23**, the i_o value is proportional to the change in corrosion rate. This reveals the sensitivity of the analysis to the initial values obtained from the system through electrochemical analysis. The trends are similar between this experiment and the sub-oxic ALDC experiment, with both of them showing a decrease in anodic potential in regions of strain which further results in an increase in predicted dissolution rate in those regions.

Corrosion of the steel coupon was characterized by rich biofilm growth, seen in the images shown in Figure 45 along with development of biotic sulfide growth shown in Figure 46. Just as with the anaerobic ALDC culture experiment, analysis of the anaerobic *Indonesiensis* experiment shows very little corrosion has happened on the surface.

Electrochemical polarization resistance curves confirm the reduction in corrosion current density as a function of time, suggesting the development of diffusion resistance layer (most likely Fe-sulfide) on the surface of the steel. These results help to reaffirm the need for oxygen as a key component for the accelerated corrosion of steel in sulfidogenic environments based upon the cathodic reactions occurring in solution.

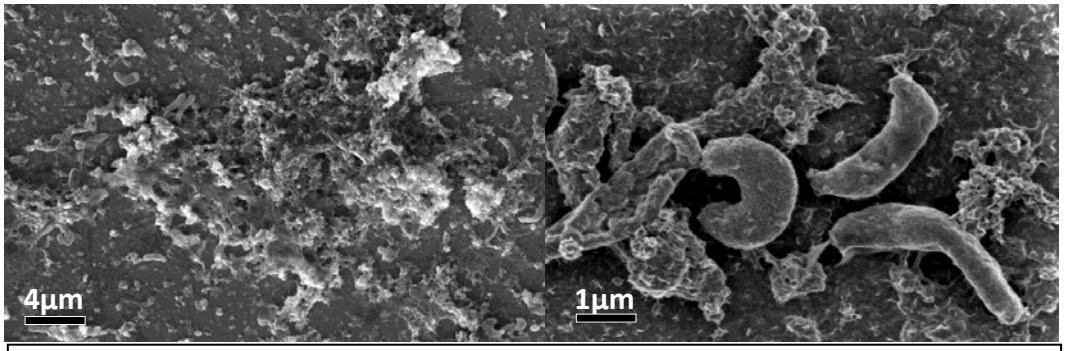

Figure 45. Left) Biofilm growth on a 1018 steel coupon after exposure to indonesiensis media. Right) FEM image showing the typical "croissant" shaped bacteria indicative of *Desulfovibrio indonesiensis*.

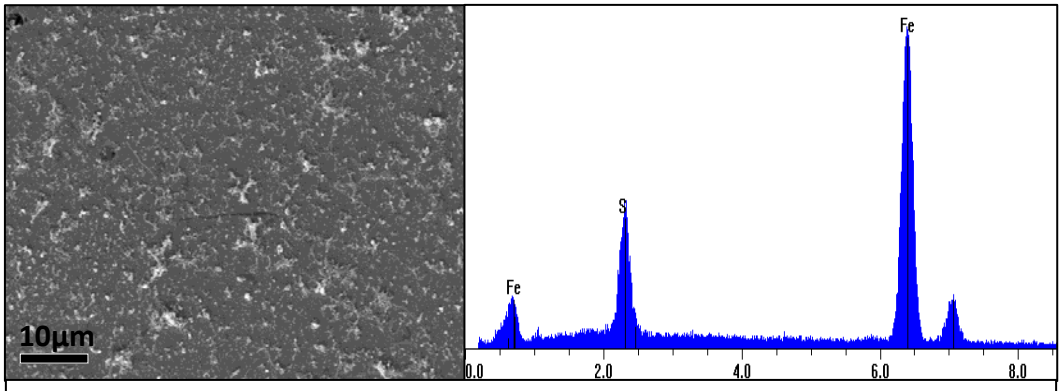

Figure 46. Corrosion deposition and biofilm colonies on a 1018 steel sample after exposure to indonesiensis media (left), and EDS spectra of the area showing the deposition of FeS on the surface (right). Note the lack of an oxygen peak, verifying the strictly anaerobic corrosive environment for the experiment.

Figure 47 shows three images taken of the same location, which reveal the connection between strain of the cementite and the accelerated corrosion rate which can is expected to happen in this region within the pearlite-rich area due to the induced strain upon the cementite due to lattice mismatch between the ferrite bcc and cementite orthorhombic structures. This location is denoted by the vertical line drawn in Figure 47.

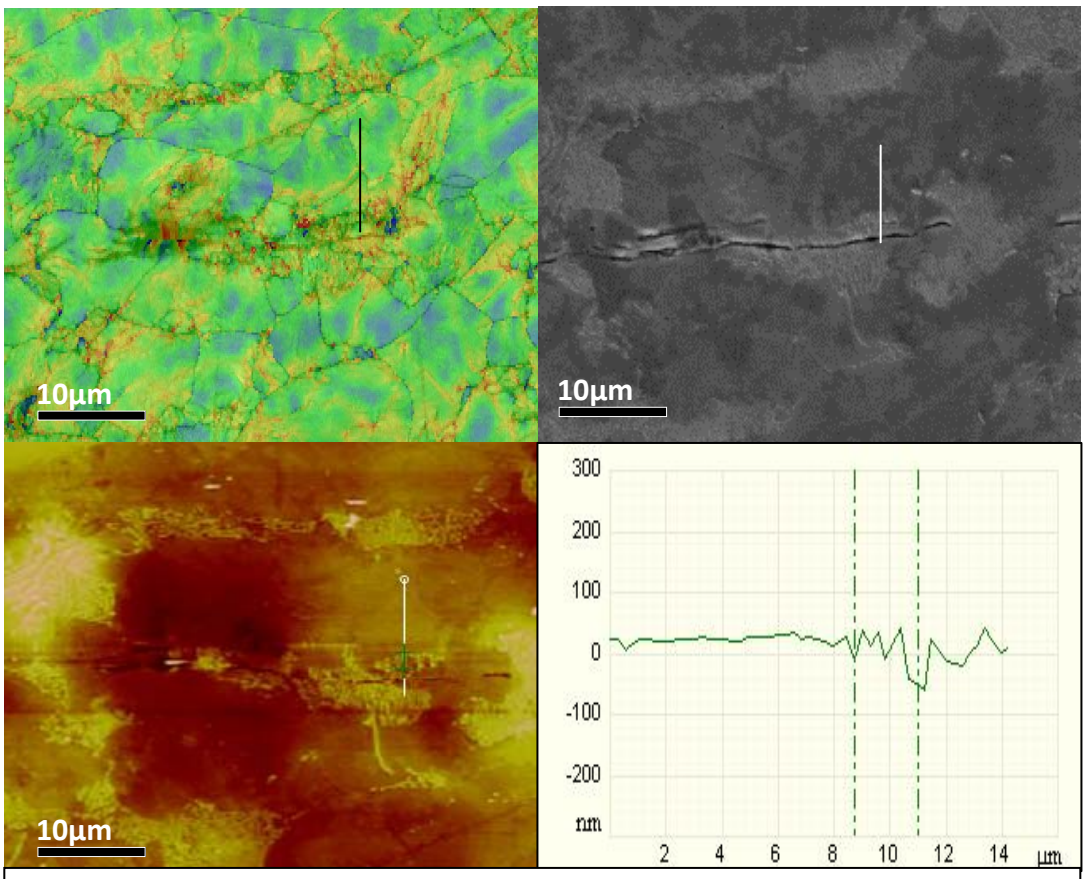

Figure 47. . Three images of the same area. The EBSD misorientation map was taken before corrosion. While the FEM and AFM images were taken after corrosion. Lines in all three images represent the location shown in the line scan (bottom right) quantifying the depth as a function of location on the line.

The AFM line scan shows an accelerated change in depth within the pearlite of approximately 75 nm. Using the Matlab *StrainedIndo.m* file I developed in connection with this work, and using values obtained from electrochemical measurements for corrosion rate, a maximum value of corrosion depth equal to almost 482.5 nm is obtained when using the initial corrosion current density of $i_{ao} = 1.687 * 10^{-6} Amps/cm^2$, while a maximum corrosion depth equal to 52.3nm is obtained when using the corrosion current density of $i_{ao} = 1.555 * 10^{-7} A/cm^2$ taken at the end of the experiment. Neither of these values identically represents the actual measured value, but it is important to note that the actual measured value does lie somewhere in between the two calculated values, and most close to that for the corrosion current density taken at the end of this experiment. This reveals something about the sensitivity of the anodic dissolution of the iron to the time dependent electrochemical processes taking place within the system.

Assuming that the iron will corrode for extended periods of time at the initial corrosion rate is likely going to produce predicted values that are much greater than the actual values, whereas anodic dissolution predictions made using electrochemical data obtained after the initial passivation period may provide a corrective factor that can serve to bring the predicted values to within a closer proximity of the actual values.

Figure 48 demonstrates the same observation as described for a parallel cut coupon; however this time the AFM scan is associated with a perpendicular cut coupon exposed to the same environment as the parallel cut coupon. The location of the

depressions of the line scan shown on the right side of Figure 49 correspond to the locations within the pearlite where the ferrite structure found between the lamellar walls of the cementite structure has corroded away, while the raised portions correspond to the harder carbide (cementite) fins that have not corroded. The depressions have not only corroded quicker than the carbide fins, they have also corroded at a quicker rate than the bulk iron that is not associated with the pearlite structure, seen on the far left side of the AFM image and accompanying line scan.

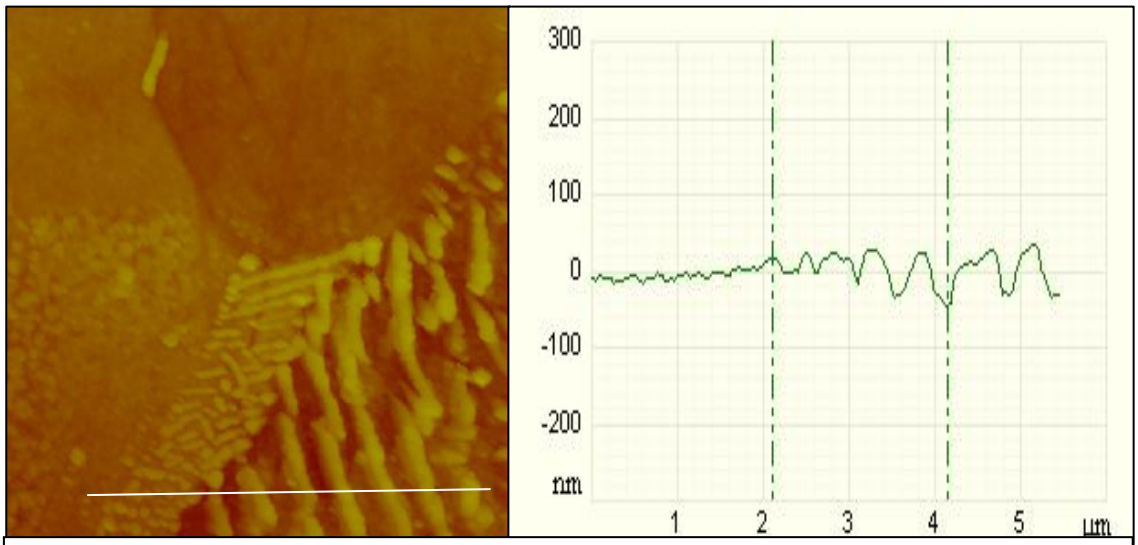

Figure 48. AFM image taken after exposure to a purely anaerobic Indonesiensis corrosion environment. The black line of the AFM image corresponds to the depth profile shown in the plot on the right.

The mass loss data, shown in Table 4, revealed that the parallel cut coupon underwent more rapid corrosion as compared to the perpendicular coupon when exposed to the same anaerobic environment containing Indonesiensis. The parallel

coupon began with a lower mass, but the change in mass per unit area after corrosion was greater for the parallel cut coupon (0.5094 mg/cm^2) than for the perpendicular cut coupon (0.4382 mg/cm^2). This correlates to a higher percent of the coupon's mass lost due to dissolution of iron for the coupon cut parallel to the rolling direction as compared to the coupon cut perpendicular to the rolling direction.

Coupon Cut	Mass Before (mg)	Mass After (mg)	Mass Loss (mg/cm^2)	Exposure Time (days)
Parallel	1165.413	1163.63	0.5094	35
Perpendicular	1191.804	1190.27	0.4382	35

Table 4. Mass loss data for steel coupons after 35 days exposure in anaerobic *D. Indonesiensis* culture.

Biyotrapped Indonesiensis Experiment

Coupons were exposed in a corrosive environment containing seawater and the bacteria indonesiensis. The methods used to create the reaction container were the same as discussed previously in the methods portion of the paper. The exposure time for the round coupon was 14 days, while the parallel and longitudinal coupons were exposed for 21 days. All samples were corroded in separate vials containing the same concentration of biyotrapped *Indonesiensis* bacteria in coffee filtered seawater to closely resemble marine environments. Each vial contained 125 µl of lactate to provide a carbon source to enable the metabolic processes of the bacteria to proceed.

Parallel Coupon

Four locations of a highly polished parallel cut coupon were analyzed at 5KX magnification using EDS, EBSD, and AFM analysis as described previously. Four locations were located before and after exposure using the measurement tool in the Ziess software SmartSEM. A line was drawn from the location to both a vertical and a horizontal axis manually etched into the sample using a diamond scribe etching tool. This ensured accurate identification of location. Figure 48 contains an FE-SEM image of a MnS inclusion running parallel to the rolling direction, and showing itself as a "snake-like" shape running horizontally through the image. These types of MnS inclusions are sometimes referred to as "stringers" in the industrial setting, and this term will be used to describe them in the following analysis for the parallel cut coupon. EDS analysis of three points, as seen in Figure 49A,B and C, verify the presence of a MnS stringer left behind from the metallurgical processing of the steel. This location was further analyzed using EBSD, and the corresponding strain map is shown in Figure 50.C. Visual analysis of the strain map identifies certain areas of strain that run in the horizontal direction across the image. These bands correspond to strain that runs along the sample in the direction parallel to the rolling direction. The FEM image shown in Figure 50.B reveals an increase in pitting and corrosion rate in the areas most highly categorized by strain. The rates of corrosion, however, are very low compared to the corrosion rate seen in the ALDC media from the prior experiment.

A possible explanation for the low anodic dissolution rates of the sample will be established using electrochemical concepts in the next section.

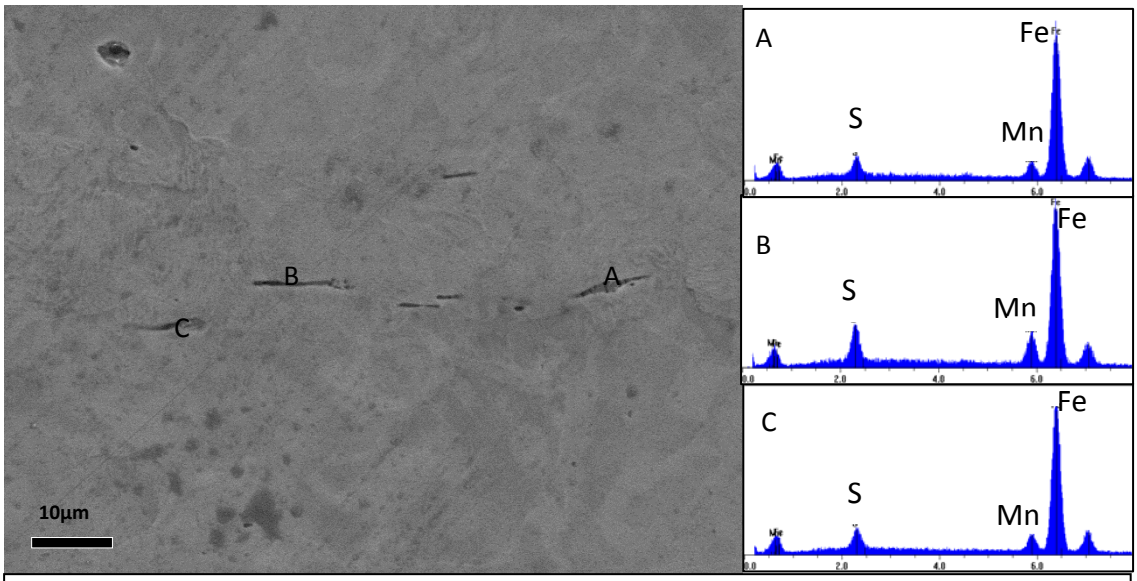

Figure 49. FEM image of a MnS Stringer on a coupon cut parallel to rolling direction (Left). EDS spectra corresponding to points A,B and C respectively from the image (Right).

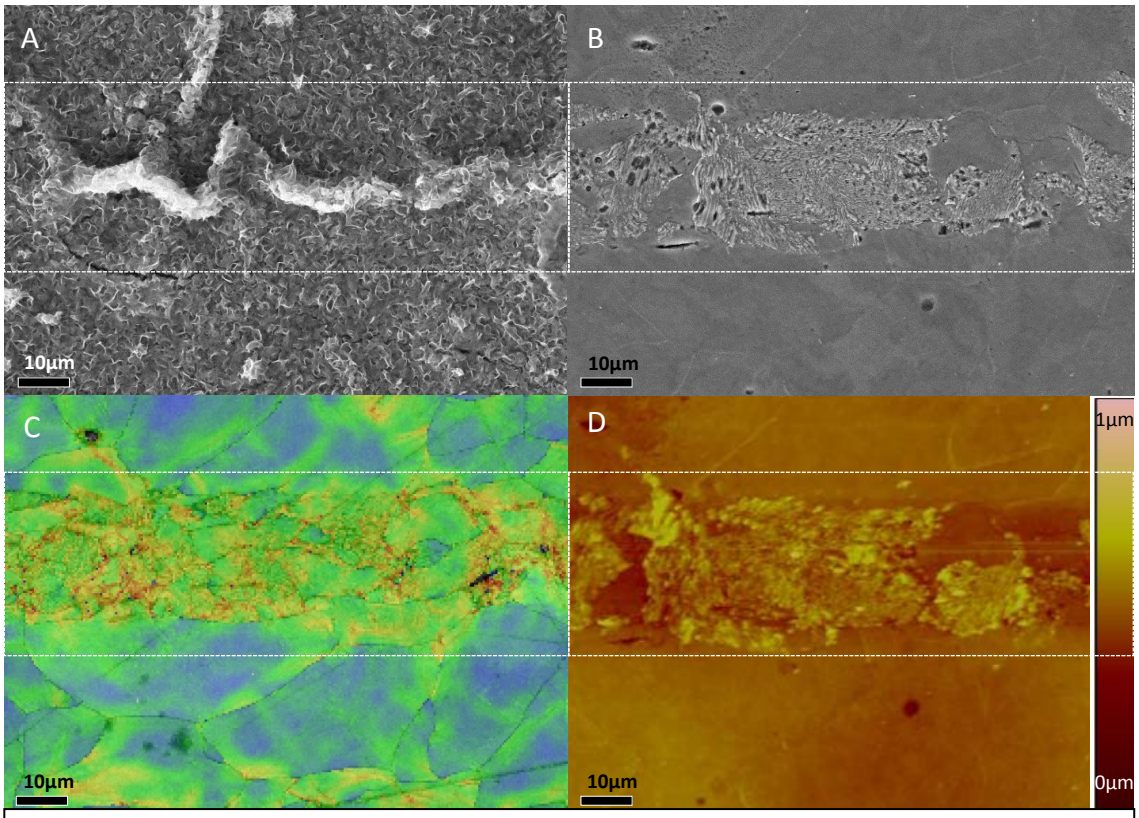

Figure 50. A) FEM image showing the corrosion product developed after 21 days exposure in Biyotrapped indonesiensis environment. B) Image of the same location after removal of corrosion product. C) EBSD local-misorientation map of the same location prior to exposure. D) AFM image of the same location after exposure and corrosion product removal. The white dashed lines were added to highlight the areas characterized by the banding of strain along the elongated pearlite structure.

Electrochemistry of a Sample
Exposed to Biyotrapped *Indonesiensis*

Electrochemical experiments give several valuable insights into the corrosion processes occurring on a sample's surface during the exposure period. For several of the experiments performed, corrosion rates as a function of reaction time were obtained by corrosion resistivity measurements, as well as by measurement of the open circuit potential (OCP) established between the 1018 steel coupon and the Ag/AgCl reference

electrode. Measurements on the *Indonesiensis* experiment using biyotrapped bacteria are shown in Figure 51.

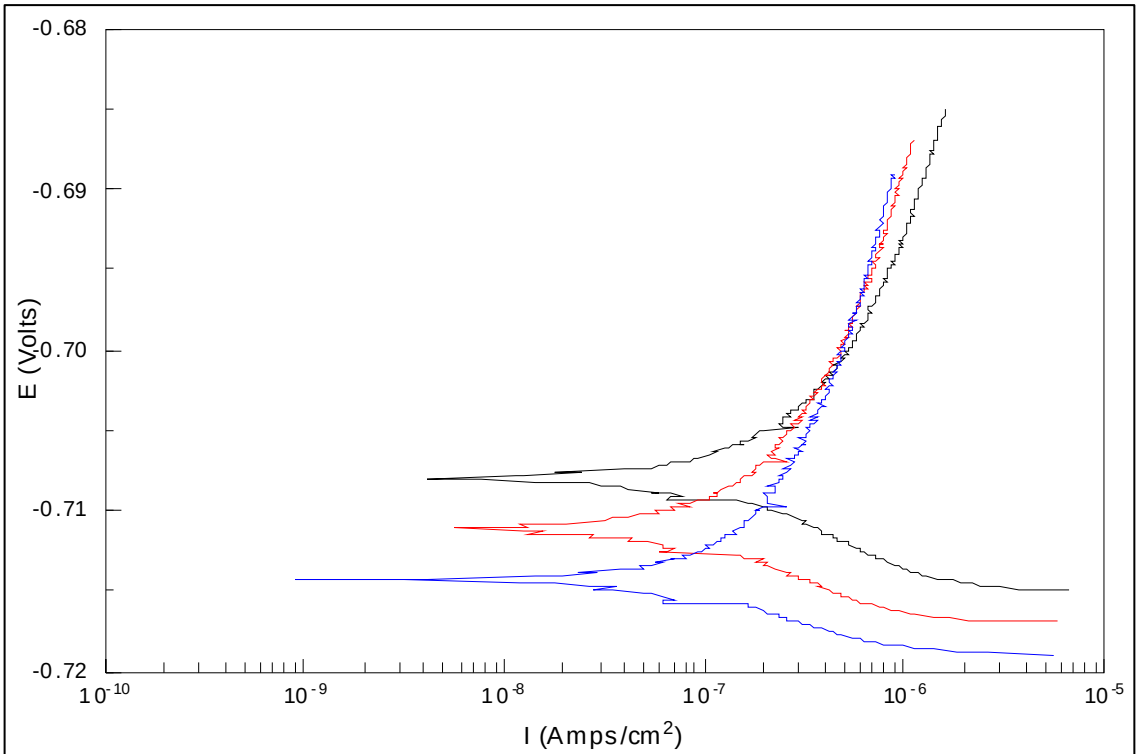

Figure 51. Tafel plots taken during corrosion using biyotrapped *Indonesiensis*. The black line indicates a measurement taken at the beginning of the experiment, the red line was taken after eleven days, and the blue line was the final measurement taken after 21 days exposure.

These results are similar to those obtained from experiments performed by other groups[47,48] for exposure of steel to SRB corrosion. The information gained form the Tafel plots give rise to several conclusions: the first observation reveals a trend in equilibrium potential that is decreasing as a function of time. Equation 13 of Chapter 1, $\mathrm{E} = -0.44 + 0.0296 * \log\ [Fe^{2+}]$ would suggest that dissolved $[Fe^{2+}]$ ion

concentration would be decreasing which is an indication of lower corrosion rates. The decrease in potential also corresponds to the decrease of likelihood of localized corrosion due to pitting and intergranular corrosion[20]. The curves also reveal a decrease in corrosion current density as a function of time, further indicating the development of a layer that has been passivated by the corrosion products. Results from AFM and FEM analysis of the coupons after corrosion show little to no corrosion occurring on the coupon's surface after an exposure period similar to that of the ALDC culture media. Low levels of sulfide as suggested by EDS often corresponds to a thin protective layer of Fe sulfide, and can serve to prevent the anodic and cathodic activities on the surface of the metal [46]. Another important result is obtained from analysis of the slopes of the curves of each polarization resistance measurement. The anodic portion of the curve is represented by those data points located above the equilibrium potential. As the slope of this curve increases, the corrosion rate as a function of changing potential decreases. This is indicative of an environment characterized by passivation of the sample[20]. The slopes of the anodic curves, shown in Figure 51, decrease as a function of time. This indicates an increase in the passivation effect upon the sample as a function of time at low sulfide levels. From the analysis of the electrochemical measurements revealing that the environment was not suitable to high rates of corrosion, it is now clear that the samples were exposed to environments that make correlating strain to corrosion rates less clear than in previously described experiments because of the cathodic protection.

The results from the biyotrapping experiment supports the belief that SRBs can be washed of inorganic sulfide created in the growth media, and the eventual development of sulfide into the system can be monitored through electrochemical measurements. The experiment also verifies the fact that high corrosion potentials are needed for accelerated localized corrosion to occur. The mass loss data from this experiment is shown in Table 5. Along with the parallel cut and perpendicular cut coupons, a control sample of 1018 steel coupon cut perpendicular to rolling direction but from a different steel rod that was round, was also exposed to the corrosion media. The area of this coupon was 2.93cm^2 as compared to the area of the square perpendicular and parallel cut coupons which equaled 3.5cm^2. The parallel cut coupon corroded faster than either of the perpendicular cut coupons.

Coupon Cut	Before (mg)	After (mg)	Mass Loss (mg/cm^2)	Exposure Time (Days)
Parallel	1229.244	1227.882	0.3891	21
Perpendicular	1248.843	1248.015	0.2365	21
Round	881.156	880.527	0.2146	14

Table 5. Mass loss data for steel coupons after exposure in corrosive media containing seawater and Biyotrapped *D. Indonesiensis*.

Trans-granular Corrosion in Abiotic Sulfide Environment

A 1018 polished steel coupon was exposed to an abiotic sulfide environment using 30mM Na_2S at pH=7.5 for 5 days in the anaerobic chamber. The coupon was analyzed using the same EBSD process as described in previous experiments. The coupons were then stripped of their corrosion deposits, and AFM data was taken of the surface.

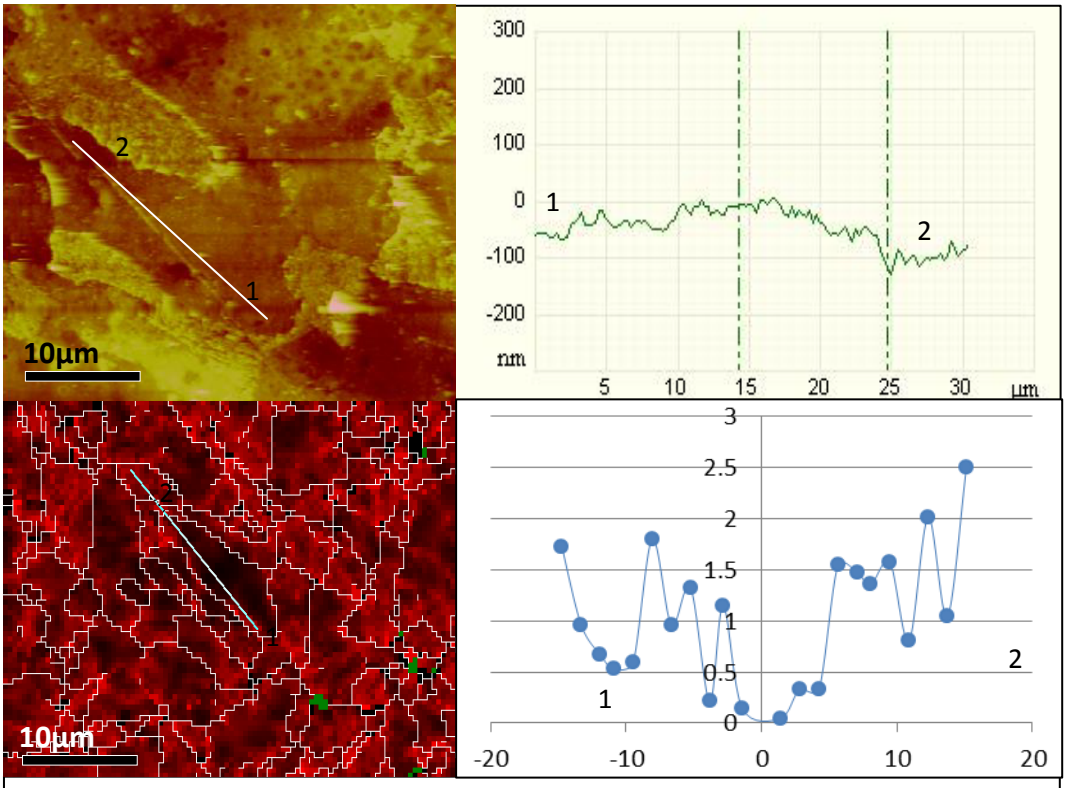

Figure 52. AFM image with an accompanying line scan shown on the top left and top right respectively, and the local misorientation map and its accompanying local misorientation-line profile shown on the bottom left and bottom right respectively. For the local misorientation map on the bottom left, dark areas indicate low strain, while red areas indicate increased strain.

Figure 52 shows the comparison between the AFM data and the local misorientation data obtained from a grain that has undergone corrosion on a perpendicular cut coupon. Comparison of the AFM surface topography plot, and the local misorientation plot reveals the analogous increase of misorientation towards the two ends of the line scans (represented by the numbers 1 and 2 in Figure 52) as well as an increase in surface depth at these locations. This reveals that there is a correlation in this grain between the deformation of the crystalline lattice and increased corrosion rate of that grain.

Corrosion of 1018 Steel Samples In Naval Fuels

JP5-Camelina

A sub-oxic experiment was performed using fuel, seawater, *Marinobacter* (an anaerobe), and *Indonesiensis* as the SRB. Previous research performed by Lewendowski et. al[3,5,6] remarks that the accelerated rate of corrosion that occurs when iron sulfide corrosion occurs in the presence of oxygen. Although a clear mechanism for the accelerated process is not exactly known, Figure 53 shows a drastic increase of corrosion deposition located at the interface of the fuel/seawater solution, which support their observations. This phenomenon was also found in the other fuels at the fuel seawater interface.

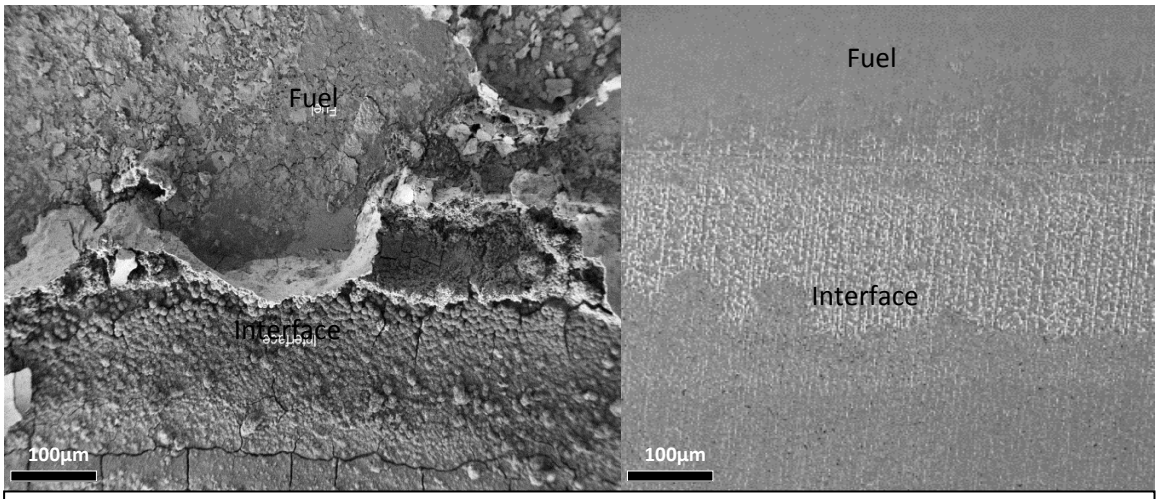

Figure 53. 1) FEM Image taken of the JP5-Camelina Fuel/seawater interface after 12 days in the reaction vessel. 2)FEM image of the same interface after the corrosion product was stripped away using Clark Solution

The increased rate of iron dissolution occurred alongside the increased deposition of corrosion product near the interface. This suggests that the increase in anodic processes near the interface resulted alongside an increase in cathodic deposition in this zone, which is shown in the right image of Figure 54. Comparison of the two images in this figure demonstrates how the increase in accumulation of corrosion deposits on the left image of the figure clearly correlates with the anodic dissolution seen in the right image of the figure. This effect is further amplified as a function of time. Figure 54 shows the development of larger corrosion deposits at the interface and the corresponding increased corrosion of bulk iron in this zone after almost 21 days of exposure in the same environment as shown in the previous figure.

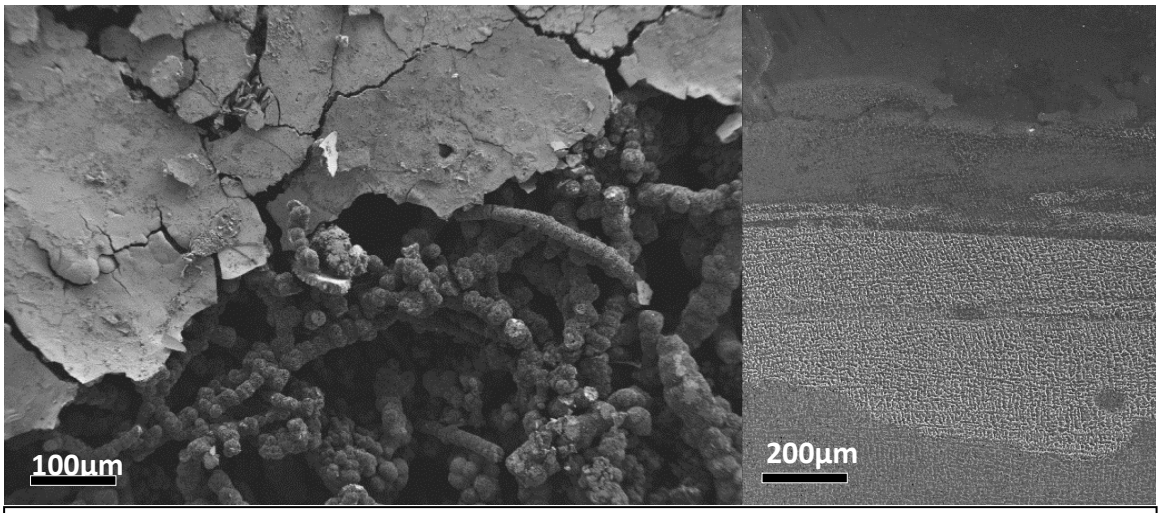

Figure 54. FEM images showing the interfacial corrosion products (left) and anodic dissolution of the bulk steel (right) after exposure to a JP5-Camelina, Seawater, and mixed microbe system for 496 hours.

This contrast becomes more striking at higher magnifications. Figure 55 is an FEM image taken of a parallel cut coupon exposed for 11 days. The left half of the image, corresponding to the interface, shows an increase in corrosion depth as a result of the interfacial aided corrosion processes. The right half of the image, corresponding to the area further from the interface and deeper into the seawater, shows little to no acceleration in dissolution.

As mentioned previously, an increase in the oxygen concentration in sulfide containing microbial environments is known to have accelerative effects on the corrosion rate of steel[49], and is the most likely explanation of the effects seen at this interface.

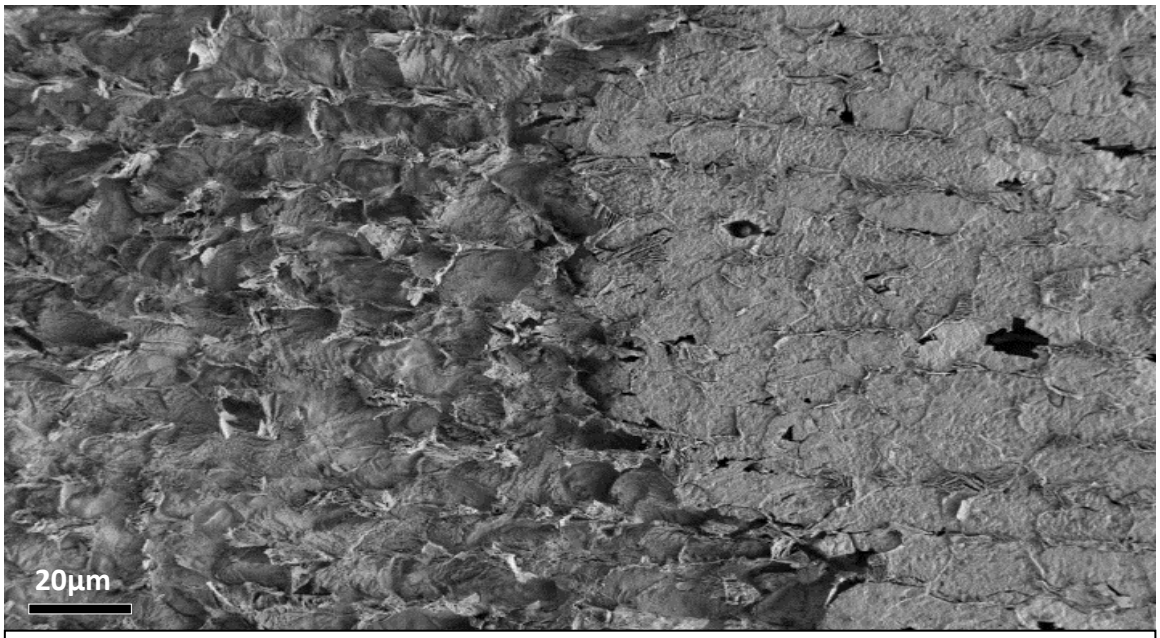

Figure 55. FE-SEM image taken at 1 KV of a coupon after exposure for 11 days in the mixed microbe fuel-seawater reactor. The left half of the image corresponds to the area closest to the interface, while the right half of the image corresponds to further from the interface and deeper into the saltwater.

In order to show this, the presence of dissolved oxygen and the sulfide accumulation on the surface of the steel are measured using oxygen depth profiles and EDX, respectively.

Oxygen Profiles

Oxygen profiles were made using the manually calibrated *Firesting* oxygen probe for each experiment. Each measurement was taken incrementally by moving deeper into the reaction vial in steps of 1mm for each reading. The value was not recorded until the dissolved oxygen readings stabilized. In all of the oxygen profiles, the origin on the depth scale (x-axis) corresponds to the point at which the oxygen probe first touched the Naval Fuel at the fuel/air interface and is measured in millimeters (mm), while the

oxygen concentration (y-axis) is measured in parts per million (ppm). Moving from left to right along the depth axis corresponds to moving the probe further down into the reaction vessel. At or near 10 mm depth for each profile there is a sharp drop in oxygen concentration to a reading of less than 1 ppm of dissolved oxygen within 1mm of depth into the seawater. Notice that our oxygen sensor is not calibrated for dissolved oxygen reading in fuels. These sensors are not so sensitive O_2 in fuels; in fact, the sharp drop in O_2 concentration from fuels to water transition usually means a drop from 70-80 ppm on the fuel side to 1 ppm in water within a mm distance of fuel/water interface.

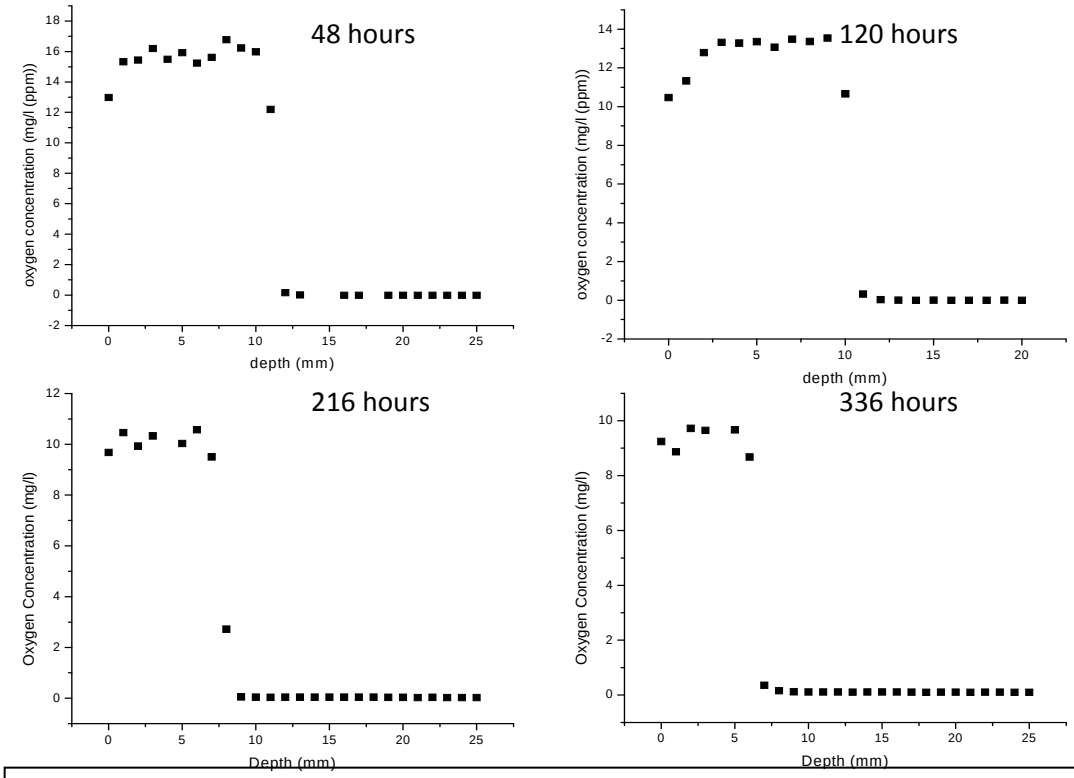

Figure 56. Oxygen profiles across the JP5 /seawater interface.

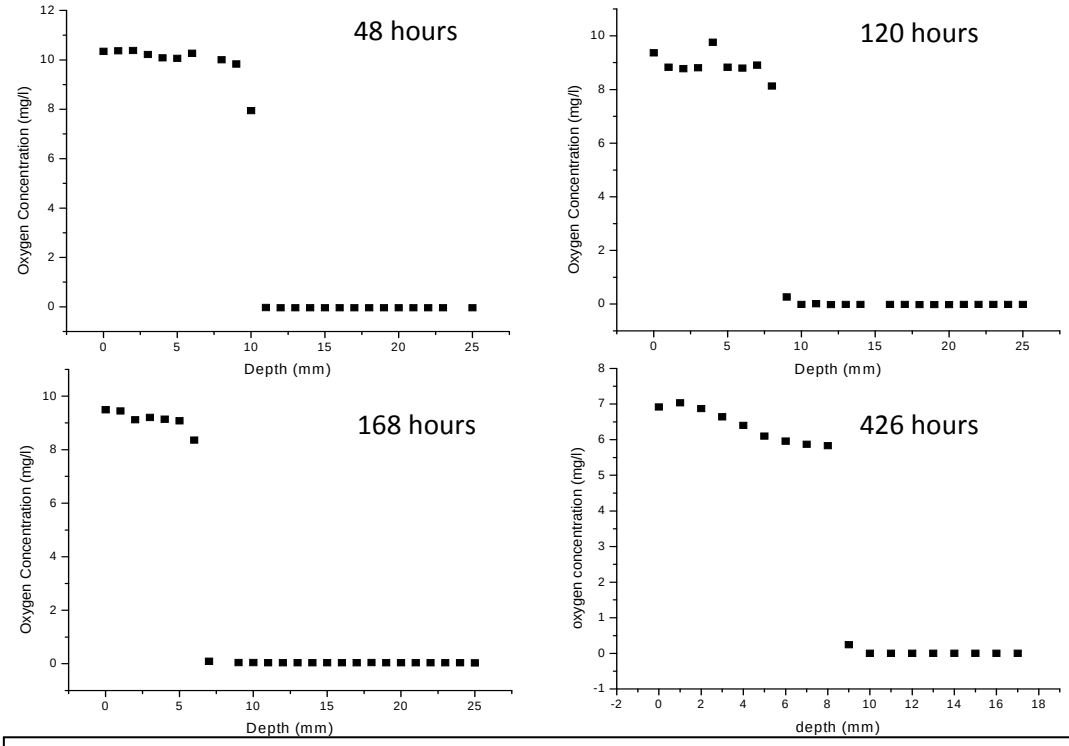

Figure 57. Oxygen profiles across the JP5-Camelina/seawater interface

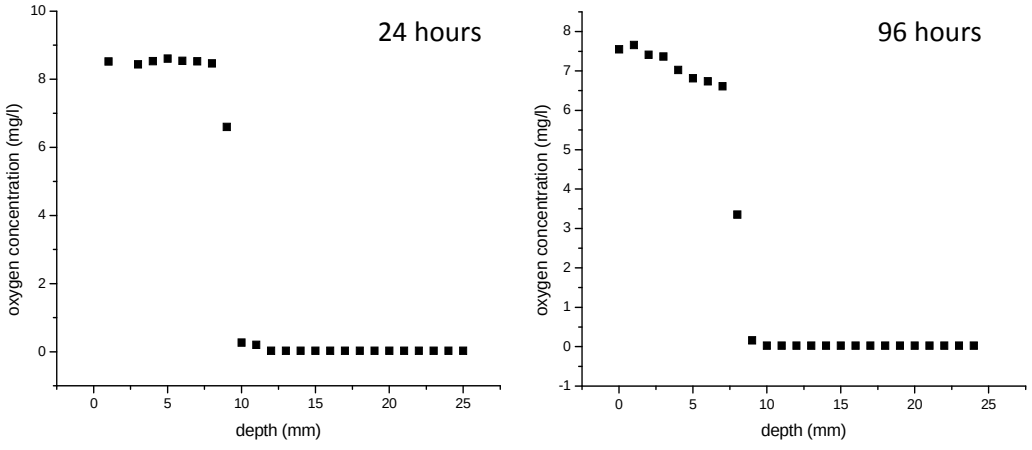

Figure 58. Oxygen profiles across the F76/seawater interface.

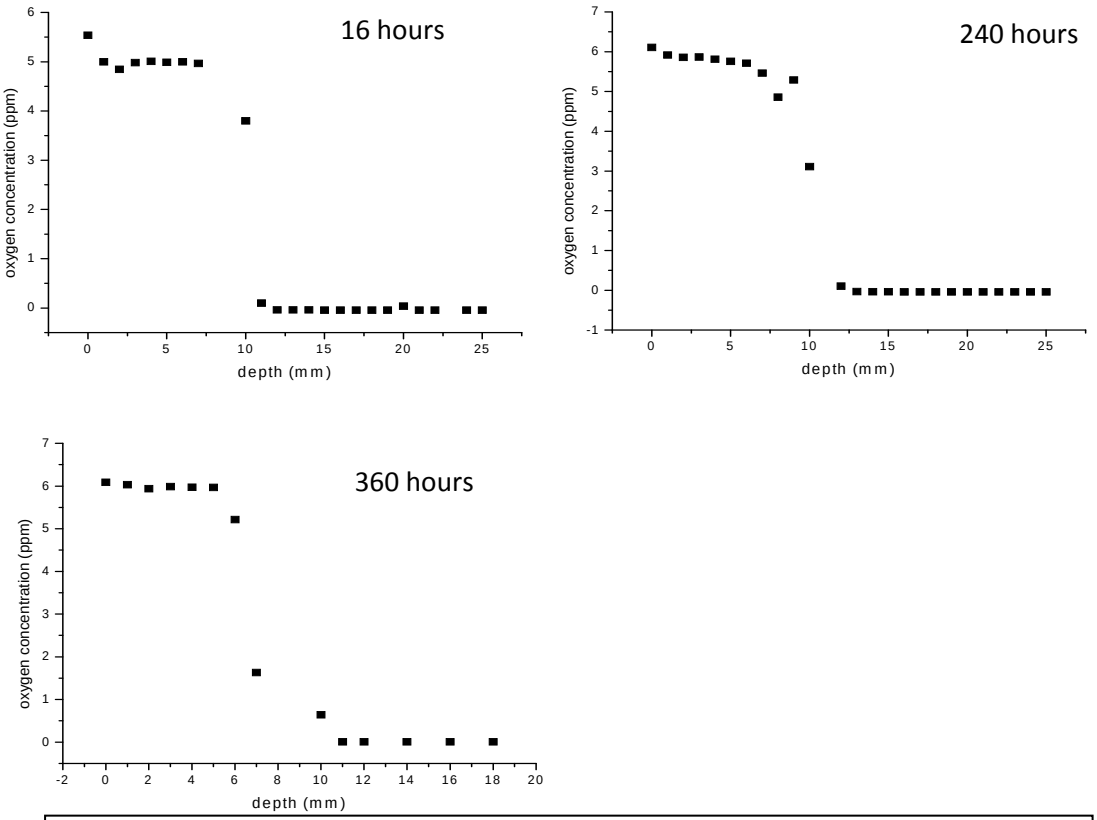

Figure 59. Oxygen profiles taken for the fuel seawater experiment using FT-F76

Development of Microbially Produced Sulfide

An important result from the experiment is the development of sulfide on the samples as the corrosion process proceeded. The sulfide present in the SRB media was washed from the bacteria by the use of the Biyotrap. This meant that any sulfide present in the system was produced post-inoculation as a result of microbial metabolism, because there was no sulfide in the system right after inoculation. The presence of the sulfide has two major implications. The first implication is that the use of biyotrap to concentrate bacteria that can be further used after isolation is validated.

The presence of sulfide in solution, which reveals its presence as iron sulfide in the corrosion deposits, indicates that bacteria were isolated from one environment, and then reintroduced into another system without jeopardizing of their viability. The second implication is that the isolation of SRB can be used as a means to further increase the control of the environmental conditions present during MIC in these types of experiments. This is a step that has not readily been performed with ease for past researchers utilizing SRB for MIC. The validation of sulfide production was performed using EDS analysis of steel samples after corrosion. Figure 60 shows the corrosion products developed in the fuel and the aqueous portion of the reaction vessel after exposure to a corrosive environment. The left image, corresponding to corrosion in the fuel, shows a very different form of corrosion products compared to the right image, corresponding to aqueous corrosion. The EDS spectra shown in Figure 61 for the corrosion product developed in the fuel and the seawater show a presence of iron-

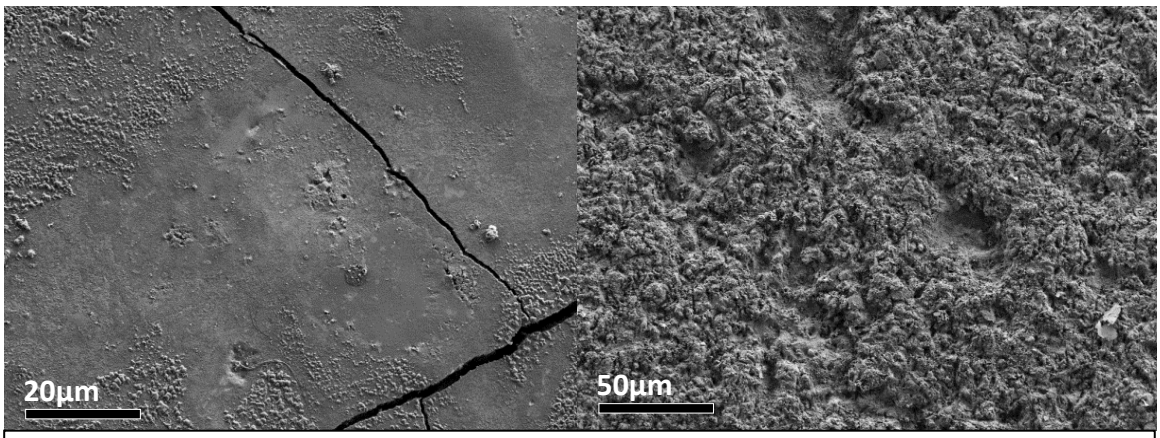

Figure 60. Left) FEM image showing the corrosion product on the sample in the fuel side of the interface and Right): the corrosion deposits on the aqueous side of the sample in a mixed culture of *Marinobacter* and *Indonesiensis*, in a JP5-Camelina/seawater system

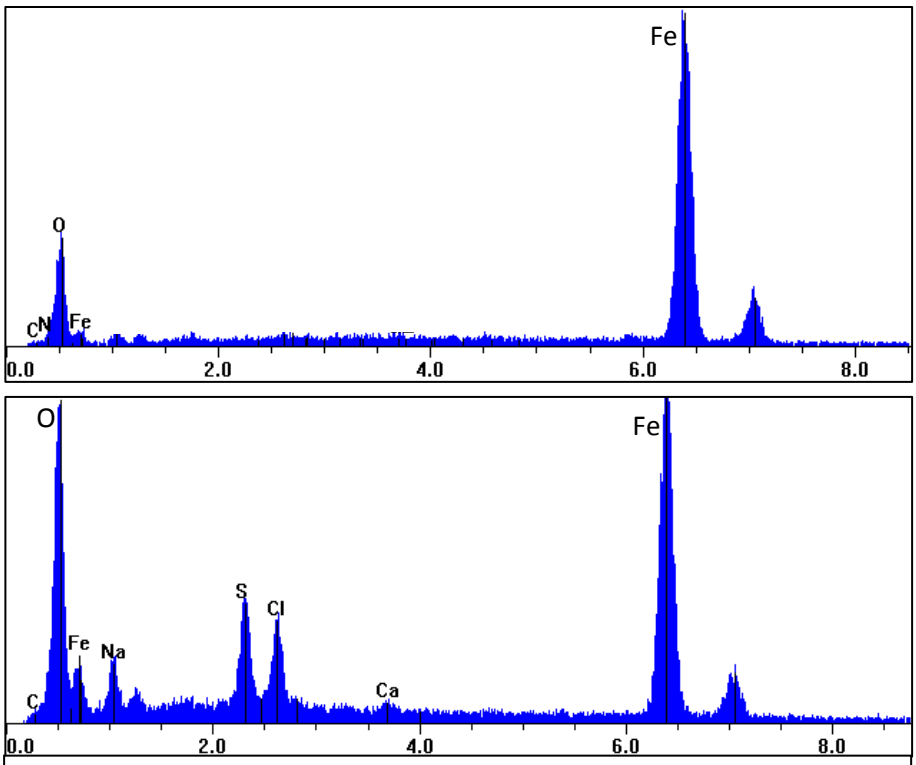

Figure 61. EDS Spectra taken from the fuel (Top) and from the aqueous (Bottom) exposed areas of a coupon after 456 hours in a mixed culture, JP5-Camelina/ seawater system.

sulfide as well as iron-oxide, and salt (NaCl) in the seawater portion, while the fuel portion of the vial shows predominantly iron-oxide formation.

Magnification of the corrosion deposits developed in the saltwater portion of the vial reveals the presence of globular crystalline structures made up of combined iron-oxides and iron-sulfides. These structures, shown in Figure 63, measure a diameter of approximately 10-20 µm and appear to grow approximately of 100 µm in height from the surface of the steel.

Further verification that these crystals contain iron sulfide by the *Indonesiensis* SRB which can be imaged on the surface of the coupons is shown in Figure 62. The images of Figure 63 show both bacteria that are present in the system during the process. *Marinobacter aq*. is seen as the oblong shaped bacteria shown in both images, while the SRB is seen in the left image having a deflated appearance and slight curvature

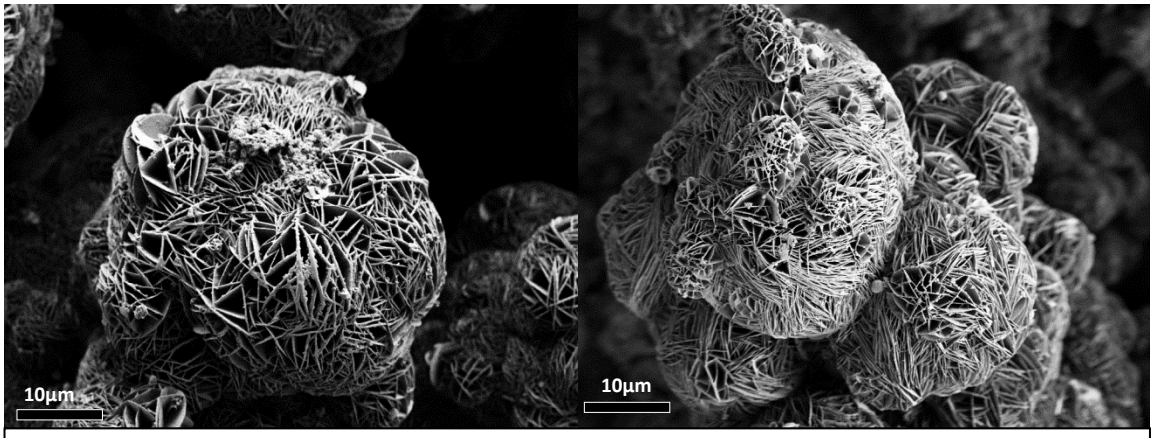

Figure 63. Two FEM images of corrosion deposits located in the saltwater portion of the reactor. Each is composed of iron-oxide and iron-sulfide created after exposure to a mixed microbe, JP5-Camelina, and seawater environment.

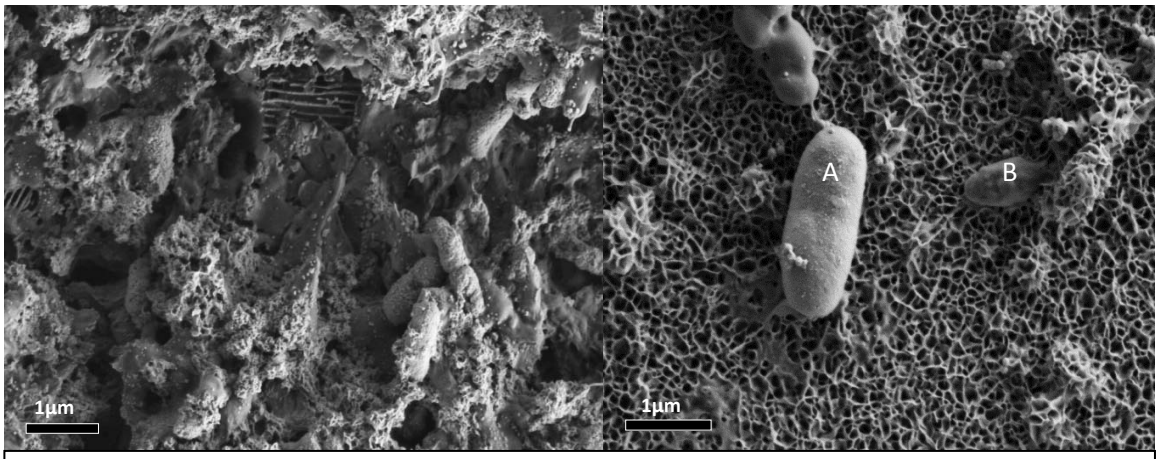

Figure 62. Left) FEM image of corrosion products mixed with biofilm and bacteria, and Right) close-up of Marinobacter (A) and SRB (B) after exposure to mixed cultures in JP5 Camelina/seawater environment.

like a croissant. These mixed cultures have a tendency to create thick biofilms on the surface of the steel. Much of the material that resembles a crust in the left image of Figure 63 is comprised of this biofilm that is mixed with corrosion deposits.

Naval Fuel-F76

Similar results were obtained for corrosion of 1018 steel in a fuel seawater environment containing *Marinobacter aq*, *D. indonesiensis* and F76 diesel fuel. There is a clear increase in corrosion deposition at the fuel seawater interface during corrosion, shown in Figure 64. Just as with JP5-Camelina, there are low levels of corrosion in the fuel, high levels at the interface, and then slightly lower levels of corrosion in the seawater portion of the reaction vial. Just as with JP5-Camelina, corrosion in the

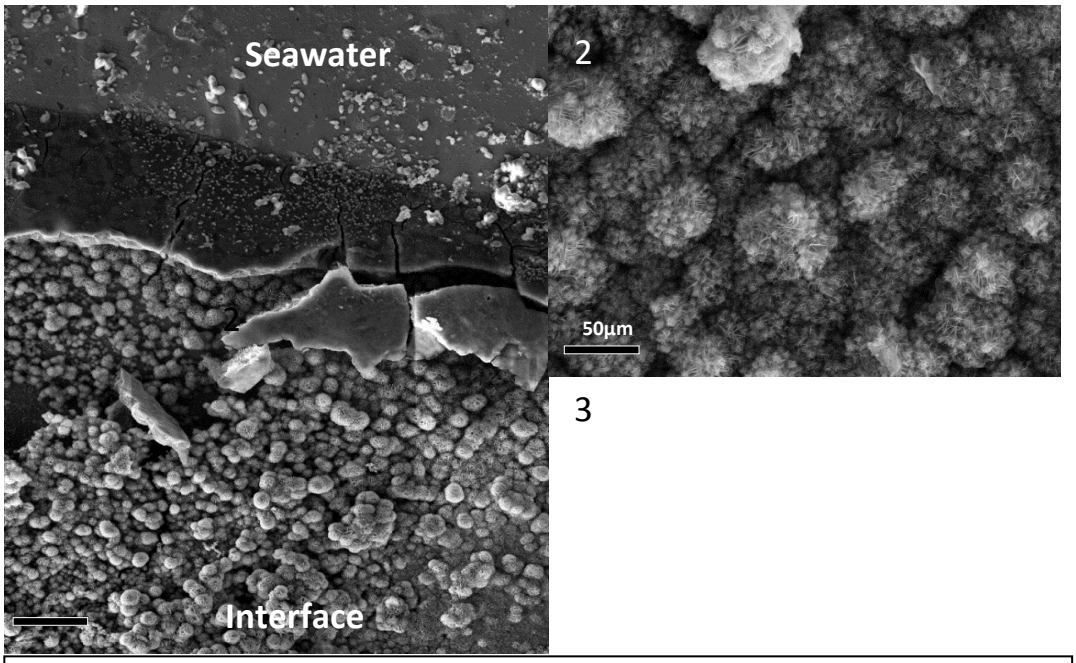

Figure 64. 1) FEM Image taken of the FT-F76 Fuel/seawater interface after 10 days in reaction vessel. 2)Higher magnification image of the seawater side of the interface showing iron-oxide and iron sulfide crystals 3) EDS spectra verifying presence of oxides and sulfides.

presence of a mixed microbial system with F76 as the fuel creates corrosion deposits made of both iron-sulfide and iron oxides. These deposits can take on forms anywhere from thin films to polyp-like shapes, often with varying amounts of oxygen, sulfide, and iron present within them. The images shown in Figure 65 reveal the shapes of the corrosion products, and the difference in density of globular polyps that were often seen on the surfaces of the samples in the portion exposed to seawater.

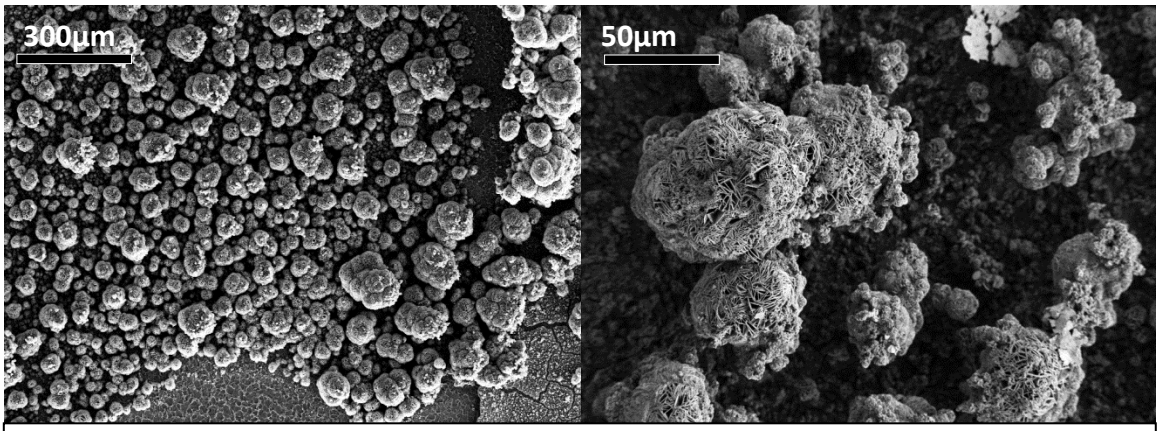

Figure 65. FEM image taken of corrosion deposits formed in the seawater portion of the corroding coupon after exposure to a mixed-culture organisms in an F76/seawater environment.

Electrochemistry in Fuel-Seawater Corrosion

To apply mechanochemical principles to corrosion taking place in fuel seawater environments, the electrochemical values of the system were obtained through open circuit potential and Tafel plots. The system analyzed was comprised of JP5-Camelina as a fuel source, with *Marinobacter aq.* a fuel degrading aerobic organisms in a syntropic relation with the anaerobic *D. indonesiensis* as the SRB in a F76/fuel environment.

An electrochemical cell was setup similarly to vials described in previous procedures. However, a modification was made for this experiment and electrochemical connections are made with the sample as well as with a counter and reference electrode to carry out Tafel plots. A needle with a 0.02 μm filter was placed through the Teflon cap of the system to allow for oxygen diffusion into the system. This scenario most accurately represents the fuel-seawater experiments performed with the various types of fuel.

Open-circuit potentials were measured using at three different depth parameters for the 1018 steel working electrode in the cell. The first parameter was measured with the entire 1018 steel electrode submerged in the seawater, the second parameter was measured with half of the working electrode in the seawater and half of the electrode in the fuel, the third parameter was measured with only one quarter of the 1018 electrode submerged in the seawater and rest of the electrode exposed to the fuel. Open circuit potentials for these scenarios are shown in Table 4, while polarization measurements shown in Figure 66 provide information about the corrosion resistivity and current densities of the sample for the three depth settings for the 1018 steel electrode by means of resistivity measurements. The open circuit potentials represent an average of the potential for each depth after three repeated measurements taken at that depth.

Location in Vessel	Open Circuit Potential (Volts. Vs. SHE)	Initial Current Density (Amps/cm²)
Fully Submerged in Seawater	-0.437	$2.717*10^{-6}$
Submerged ½ in Seawater	-0.428	$3.354*10^{-6}$
Submerged ¼ in Seawater	-0.411	$8.033*10^{-6}$

Table 6. Open circuit potential measurements taken using a Ag/AgCl reference electrode in a fuel-seawater mixed microbe corrosion environment using JP5-Camelina, *Marinobacter* and *Indonesiensis* (center) and the calculated corrosion current density based on the measured resistance (right).

The polarization resistance curves in Figure 66 also reveal the change in equilibrium potential of the three different depth scenarios for the 1018 steel coupon.

At a depth primarily characterized by the oxygen rich fuel the electrode potential increases. Corrosion current density is highest when the electrode is characterized primarily by its location in the oxygen rich fuel, while the coupon exhibits the lowest current density when exposed equally to only the sulfide rich saltwater. The value for the half submerged coupon will be used to perform mechanochemical analysis on the coupon due to the similarity of the electrode's environment to that of the corroding coupons, though there would still be areas of the sample that were also exposed to the fuel environment.

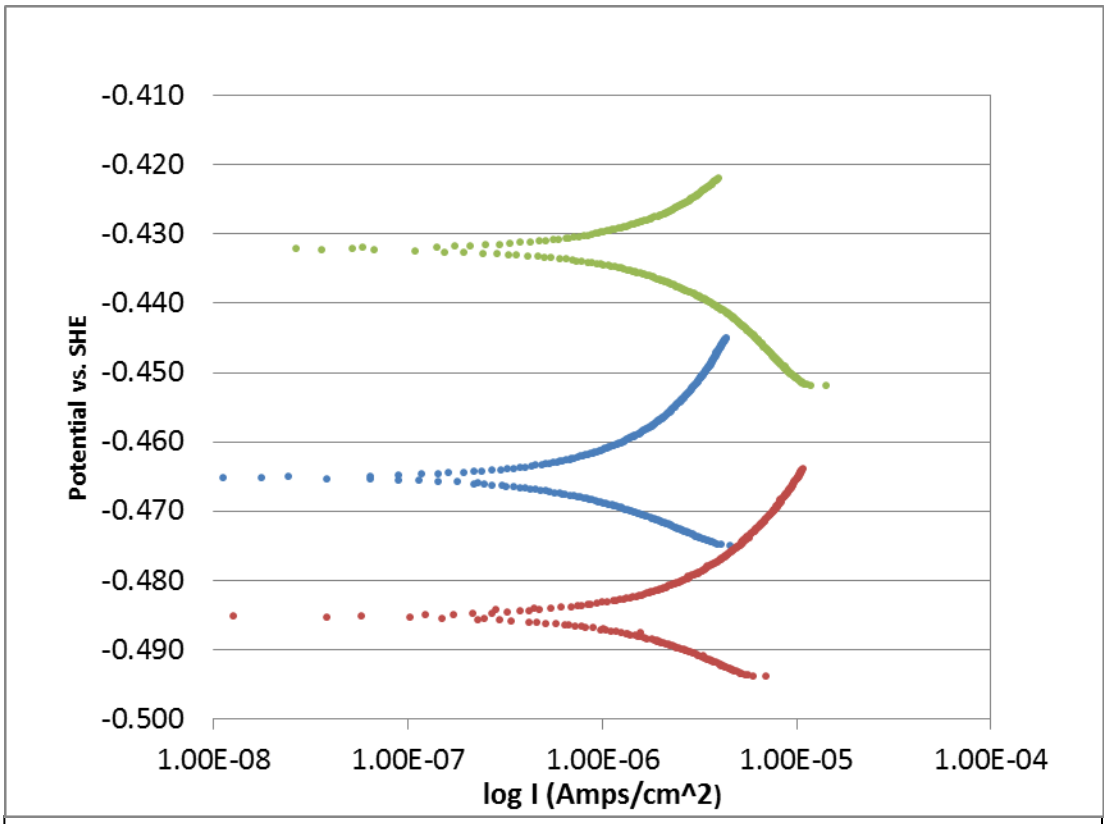

Figure 66. Polarization resistance measurements taken at the three different depth parameters for the 1018 steel working electrode; fully submerged in seawater (red), half submerged in seawater and half submerged in JP5-Camelina fuel (blue) and one quarter submerged in seawater and three-quarters submerged in JP5-Camelina fuel (green).

To further quantify the interfacial effects on the corrosion of 1018 steel coupons exposed to this type of system a parallel cut coupon and a longitudinal cut coupon were analyzed using EBSD and AFM, and then allowed to corrode in a mixed microbe fuel-seawater system setup using the same components as the electrochemical experiment described above.

Corrosion Products

FEM analysis using EDX line-scans reveal the change in oxygen and sulfur content as a function of location above and below the fuel-seawater interface. The results for this analysis performed on a parallel cut coupon exposed for 7 days in a mixed microbe fuel-seawater environment are shown in Figure 67. The EDX line-scan reveals an increase in sulfur intensity as depth increases below the interface, and little to no sulfur at locations above the interface. Oxygen concentration is;ljkh high at locations above the interface and low at or below the interface, which is also supported by the oxygen profiles taken of the various mixed microbe fuel-seawater systems at various exposure times.

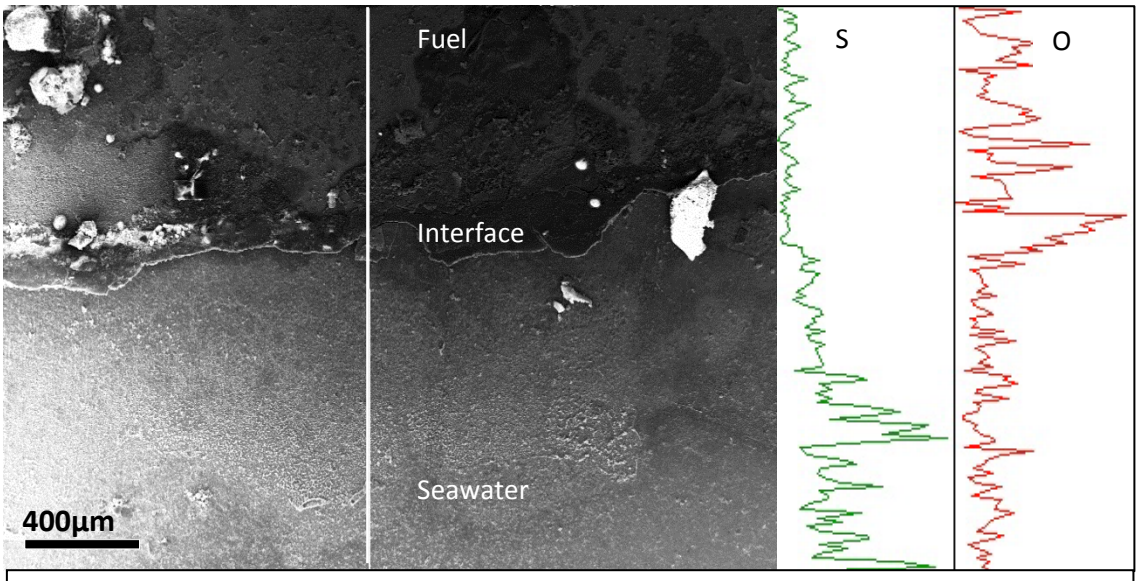

Figure 67. FEM image taken at 20kV of the corrosion deposits on the surface of a 1018 steel coupon after 7 days exposure in a mixed culture JP5-Camelina and seawater experiment. The white line represents the location of a line-scan taken across the surface of the coupon, while the two plots on the right represent sulfur intensity (green) and oxygen intensity (red) as a function of position along that line.

Mechanochemical Analysis

Highly strained areas of a parallel cut coupon were established using EBSD analysis, shown in Figure 68, and the original AFM surface topography of this location revealed an original surface roughness of less than 100 nm. Due to the roughness of the sample after corrosion, obtaining AFM data over large areas of sample proved extremely difficult and provided results with high amounts of noise and inconsistencies in surface topography. In light of this fact a specific area was selected from the EBSD image that was smaller in size, yet showed high changes in lattice orientation. This selected area, shown as the white box in Figure 68, was then analyzed using mechanochemical analysis through the Matlab *StrainedMarIndo.m* file attached in the appendix of this thesis.

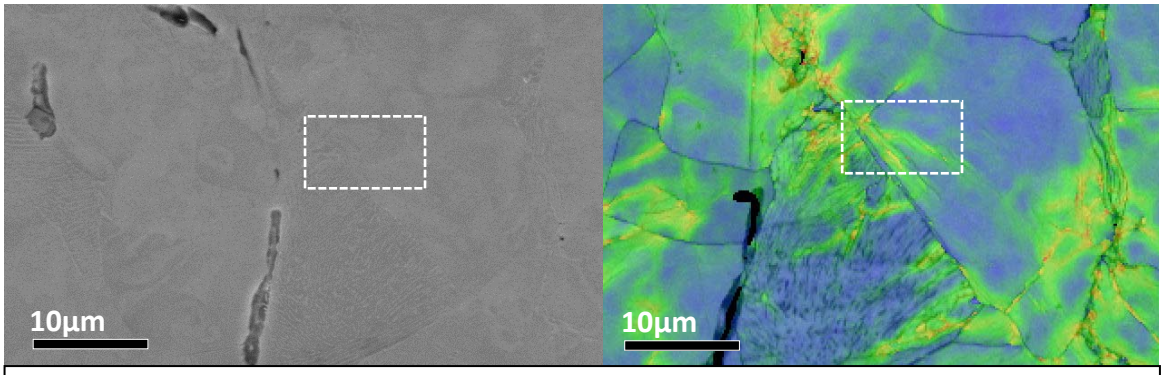

Figure 68. FEM image (left) of a parallel cut 1018 steel coupon that has been polished to 0.04µm colloidal silica, and its accompanying EBSD local-misorientation map. The white box shown in the EBSD image represents the area that was analyzed using mechanochemical analysis.

Application of mechanochemical equations to the strained areas shows an increase in current density in highly strained areas, as well as a decrease in anodic equilibrium potential in these areas. Figure 69 highlights this trend in the top two images. Dissolution of iron on the surface of the steel is illustrated in the bottom two images, which show a correlation between the areas predicted to corrode the fastest and those which actually did corrode the fastest. Just as with the sub-oxic and the anaerobic environments examined earlier, areas showing higher strain through plastic deformation resulted in a decrease in the anodic equilibrium potential, which further

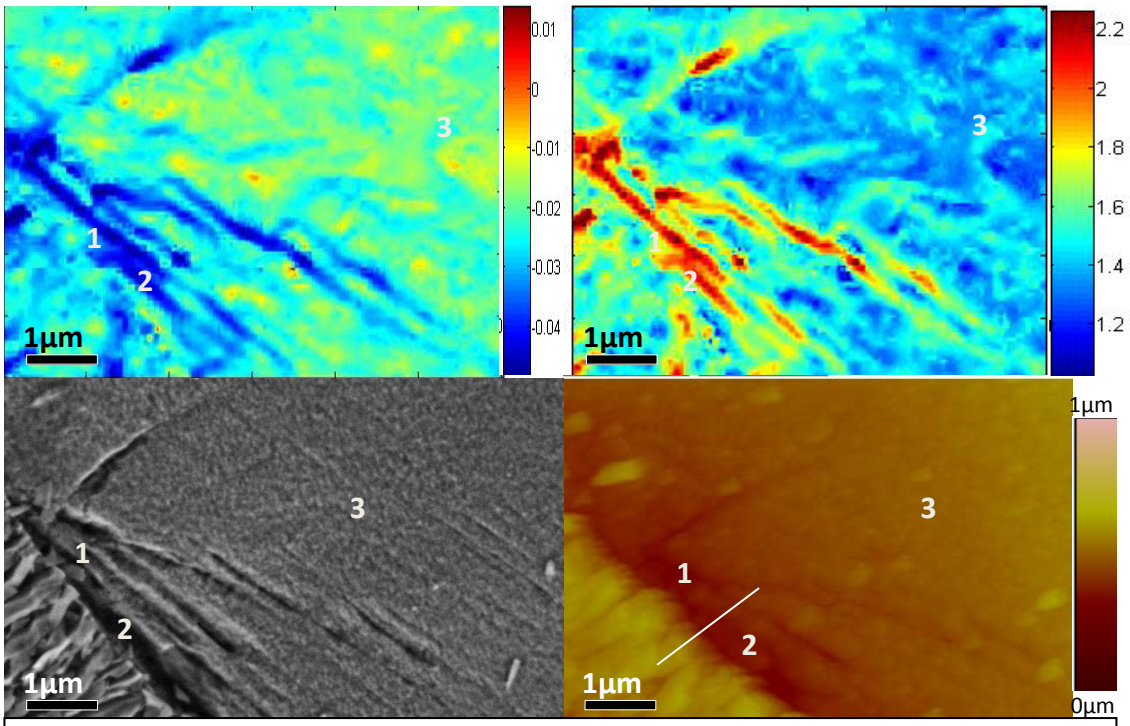

Figure 69. Prediction of the change in current density as a ratio of $\Delta I/i_o$ (top-right) and the change in anodic equilibrium potential measured in volts (top-left) resulting from mechanochemical analysis using EBSD local misorientation data of a 1018 steel coupon. The associated area after corrosion in a mixed culture JP5-Camelina and seawater environment is shown in the FEM image and AFM image on the bottom-left and bottom-right respectively. Numbers 1,2, and 3 correspond to the same locations in each image.

resulted in an increase in corrosion current density at those locations.

Comparison of predicted corrosion rates based on EBSD strain data and AFM measurements were made using depth profiles along the white line shown in the AFM image of Figure 70. AFM data along this line revealed a change in depth from the highest point to the lowest point of approximately 0.2409 µm, while mechanochemical analysis predicted a change in depth of 0.2794 µm. This gives an error of 15.9 %.

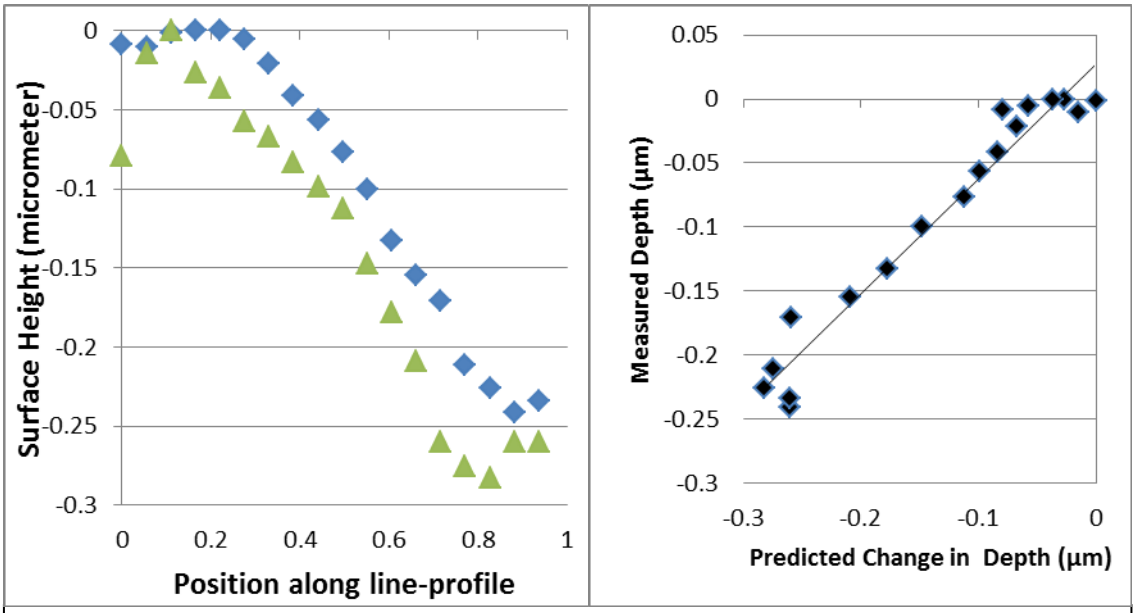

Figure 70. Left)Plot of the predicted change in depth along the white line shown in the AFM image of Figure 63 (green) and the measured AFM depth along the same line (blue). Right) Plot of AFM depth compared to predicted depth with added trend line to show the correlation of the two data sets.

Fitting a linear regression to the plot given on the right side of Figure 71 yields regression curve given as:

Measured Depth (µm) = 0.8962*(Predicted Depth µm) + 0.0278

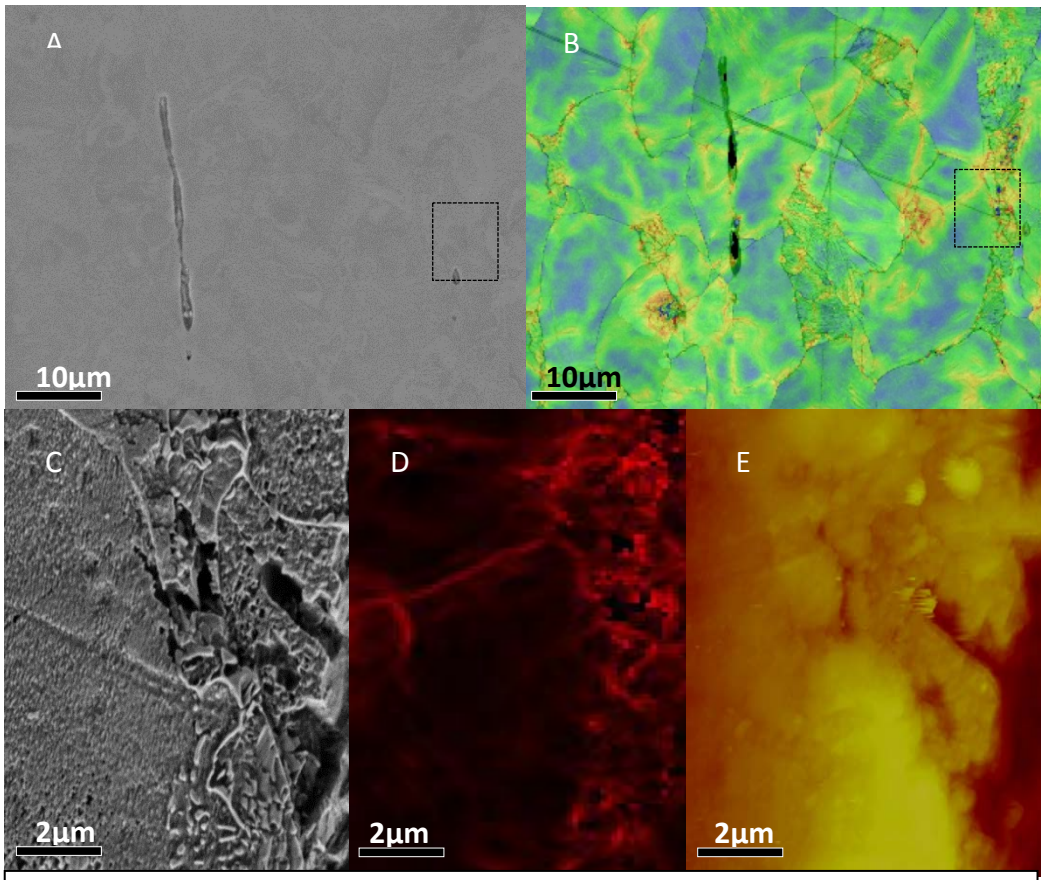

Figure 71. Images showing the comparison of FEM imaging (A,C), EBSD mapping (B,D), and AFM analysis (E) of the same area before and after corrosion. Images C,D, and E are the enlarged images marked by the rectangle on the FEM and EBSD images shown in A and B.

This equation essentially provides a tool that can be used to establish the percent changes that need to be multiplied to the predicted depth to achieve the measured By multiplying the predicted depth by a factor of 0.8926 the measured depth would be expected. This essentially says that the average error along the line is approximately 10.2 %, or that the model predicts all points along this step (not only the final depth), to a value within this much error. This transformation could be applied at any number of

places, with the most logical place of application being the initial corrosion current. As it was mentioned earlier, the technique used to calculate this current can produce errors of up to 25%. Therefore, by applying an 11% correction factor through the linear regression curve above, we stay well within the original 25% error, and provide a means to better calibrate the model.

Due to the nature of this corrosion, it is very possible that any number of factors could have reduced the rate of corrosion of the sample from the predicted value. The most likely possible explanation is that there was a development of a passivation layer on the surface that would have reduced the ability of the metal to corrode at the predicted rate. This is supported by the decreased corrosion rate in many of the different sulfide systems as a function of time. Since the corrosion current density selected for use in the model was the initial corrosion rate of the system, it is likely this will change with time, which is supported by passivation theory. The process is still valuable in locating those areas that are most likely to undergo an accelerated change in corrosion rate.

Another location was analyzed using the same methodology and corrosion parameters to verify the repeatability of the trend seen previously. In this location there is an unstrained area, seen on the left side of Figure 71.C,D, and E that is located directly next to a strained band located on the right side of the same images.

Here, visual analysis confirms the increased dissolution of the metal on the right side of the images.

This trend is further illustrated in Figure 72 where the predicted and measured higher part of a line-scan taken across this area is located towards the left, and then an increase in corrosion depth occurs towards the right side of the plot.

The maximum predicted change in depth from mechanochemical analysis is 0.725 µm along the line shown in Figure 72, while the measured AFM results give a change in depth of 1.143 µm. In this instance, as opposed to the other situations, the AFM produced depth results much larger than the predicted depth, resulting in an error of 36%. Despite the larger error, the regions predicting low dissolution rates do in fact demonstrate less change on the AFM scan, while those areas predicted to have higher dissolution rates also demonstrate greater change on the AFM scan.

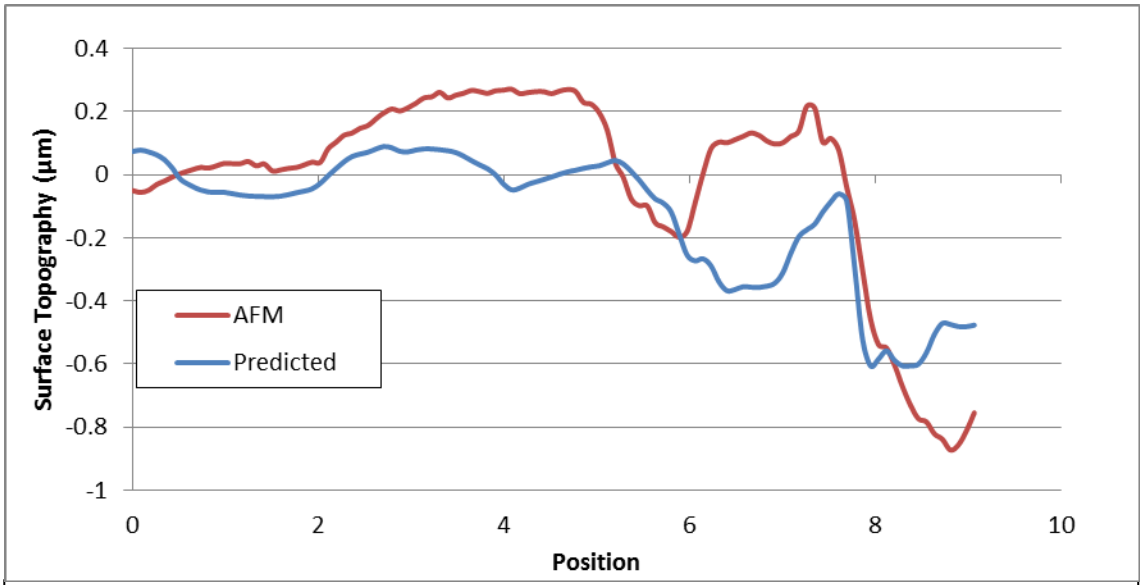

Figure 72. Plot showing surface topography as a function of position for the data predicted by mechanochemical analysis (blue-line) and the AFM surface measurements (red-line).

Further Material Analysis of 1018 Steel Coupons

Manganese Sulfide Inclusion Locations

EBSD analysis has been used to show the correlation between strain and corrosion. Another important benefit of the use of EBSD is in analysis of the environment in close proximity of MnS inclusions for two reasons: (1) Immediate surroundings of these inclusions usually are the seeds of pit initiation and development and (2)because of the presence of MnS inclusions the immediate surroundings of these inclusions would be expected to be highly strained and would be more active (anodic) relative to the unstrained areas. Figure 73 shows an FEM image of a MnS stringer located within an iron environment. The verification of the chemical compositions of the components of this image is shown in the EDX spectra on the right side of Figure 75.

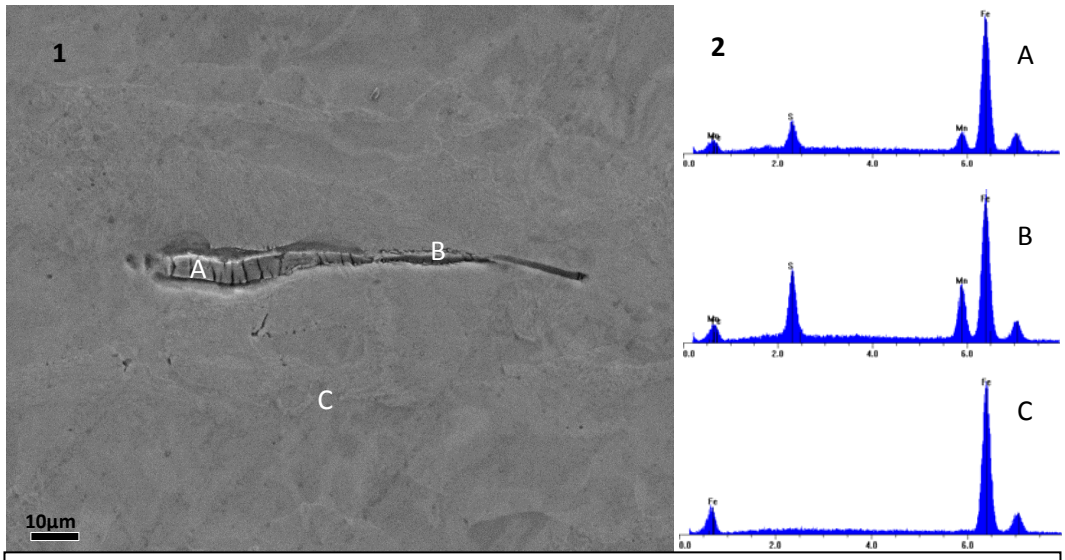

Figure 73. 1) FEM image of a MnS Stringer on a coupon cut parallel to rolling direction. 2)EDS spectra corresponding to points A,B and C respectively from image A. Note the Presence of MnS in spectra A and B while spectra C shows only Fe.

Visual analysis of the inclusion from the FEM image alone yields very little information about the material characteristics surrounding the inclusion. EBSD analysis is required in order to identify the material nature of the steel structure surrounding the inclusion. Figure 74 shows the accompanying local misorientation map on the left, and the inverse pole figure map on the right for the location shown in Figure74. The local misorientation map reveals that the MnS stringer is clearly located in a region of high strain. The inverse pole figure map shows the orientation directly around the stringer varies in direction from 001 to 101, indicating that surrounding orientation has little effect on the formation of the stringer. Further analysis of the inverse pole figure map reveals a decrease in grain size in the region surrounding the inclusion, as well as an increase in deformation of the grain shape in this region. Corrosion of the sample revealed that the inclusion is located in a pearlite band that was formed due to rolling of the sample during post processing, which can be seen as the striations in the FEM image of Figure

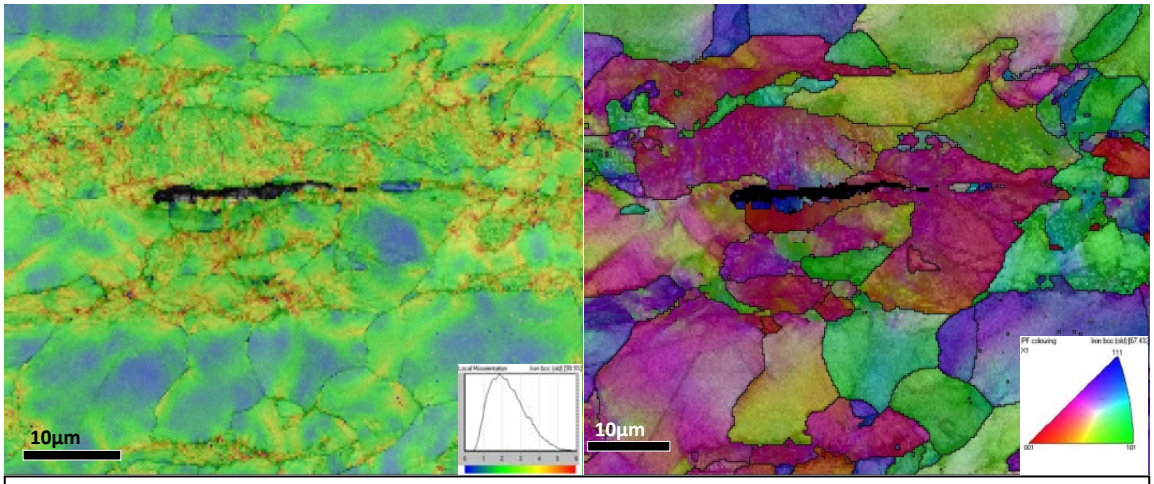

Figure 74. Left) EBSD local misorientation map, and Right) Inverse pole figure map of the same area shown in Figure 71.

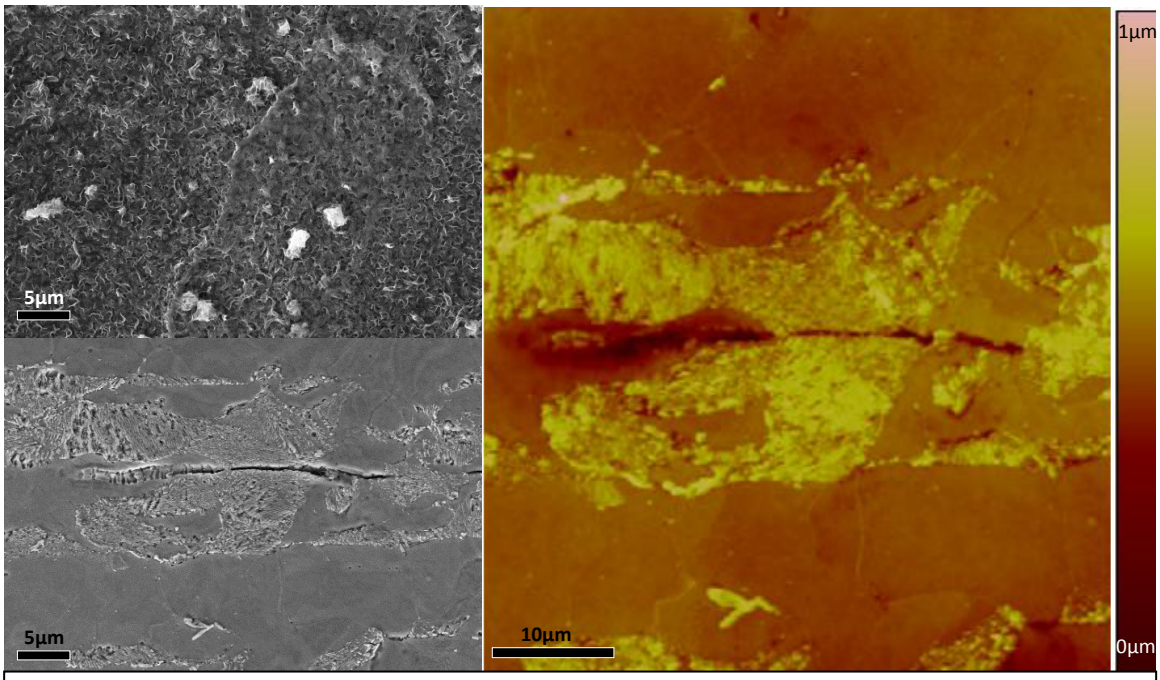

Figure 75. Top left) FEM image of Iron Sulfide corrosion deposits after 21 days corrosion in Biyotrapped SRB environment. Bottom Left) FEM image of the same location after removal of the corrosion deposits. Right) AFM surface topography of the same location after removal of the corrosion deposits.

75, as well as the non-corroded regions in the AFM image.

Bulk Orientation and Misorientation of Samples

In order to categorize the type of orientation and also the type and amount of misorientation of the perpendicular cut compared to the parallel cut sample, the use of pole figures is necessary. For the coupons cut parallel to the rolling direction, there is a clear indication of orientation density preferred in the 101 direction (Figure 76). The majority of misorientation (not to be confused with local misorientation) occurs at misorientation angles between 40-60 degrees, and a lower density of misorientation occurring at angles below 40 degrees. Analysis of the inverse pole figure suggests that

there is a wide array of crystalline orientations possible in the parallel cut coupons. Further analysis reveals that despite the large range of orientation, there is little to no lattice orientation in the 001 and 111 crystalline directions, as seen in both images of Figure 76.

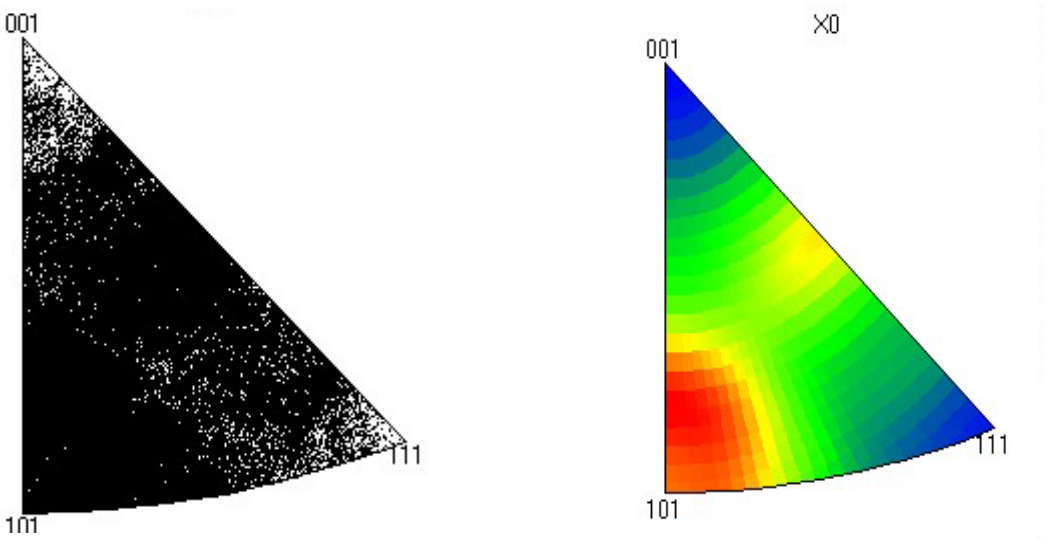

Figure 76. The Inverse Pole Figure giving orientation density (black dots) for a parallel cut coupon is given in the figure on the left, and the density of points (shown as black on the left) are given as a gradient on the right. In the figure on the right, red corresponds to high density while blue corresponds to low density.

The misorientation figures shown in Figure 77, reveal that despite the low number of indexed points directly oriented in the 111 direction; the highest degree of misorientation seems to be present in the lattices oriented in this direction. This suggests that there is a potential link between 111 crystalline orientation, and strain induced in this direction. Cold rolling of steels results in deformation along the rolling direction (111)[50]. This suggests that crystals deform in the rolling direction, which helps

to explain the corrosion which occurs parallel to the rolling direction in bands of strained areas. By comparing the pole figure with the misorientation figures, the low relative amount of grain area accompanied by the 111 orientation, with the high amount of misorientation in the 111 direction, suggests that these locations are less likely to form during the crystallization process, however when they do form they do so under conditions that result in high amounts of strain due to lattice misorientation.

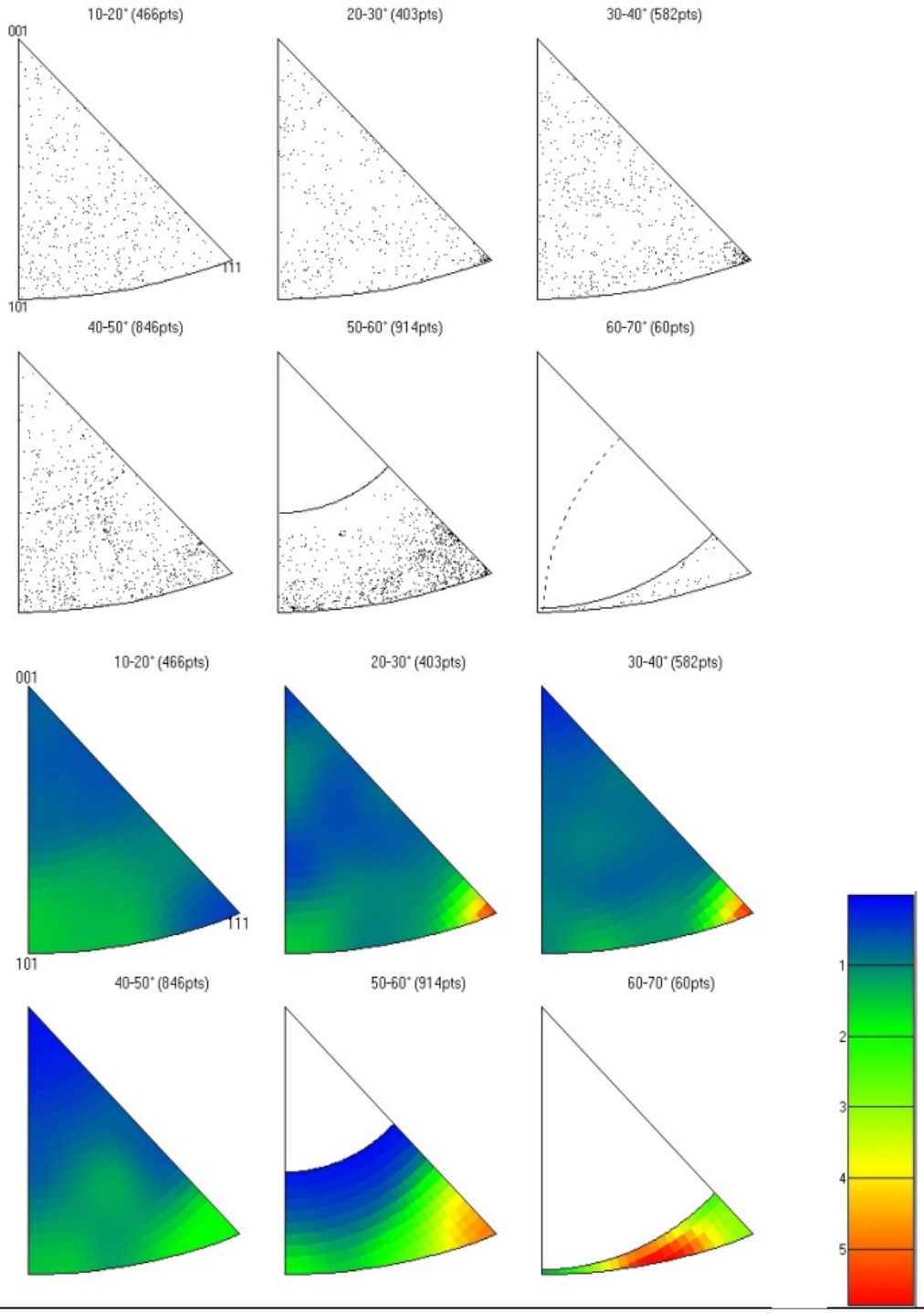

Figure 77. The misorientation density (black dots) as a function of orientation, and amount for a parallel cut coupon is seen in the top set of images. The set of images below shows the density of these points as a color gradient with red corresponding to high density while blue corresponds to low density.

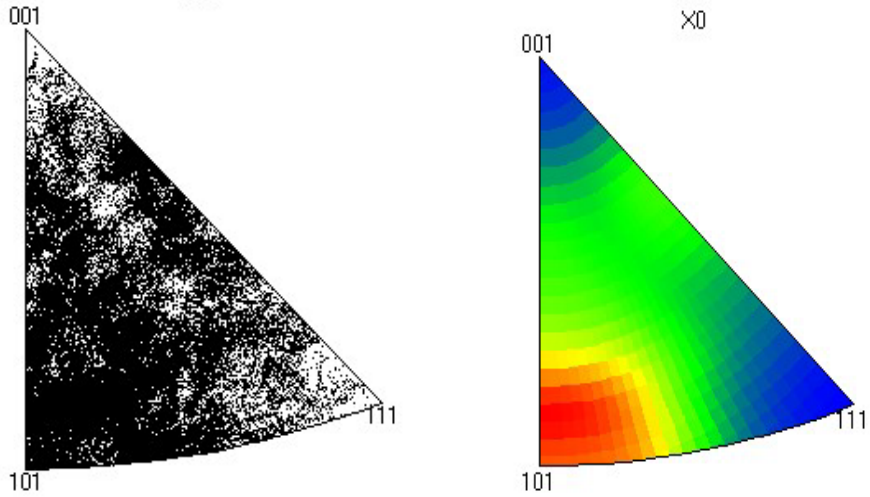

Figure 78. The Orientation density (black dots) for a perpendicular coupon is given in the figure on the left, and the density of points given as a color gradient on the right. In the figure on the right, red corresponds to high density while blue corresponds to low density.

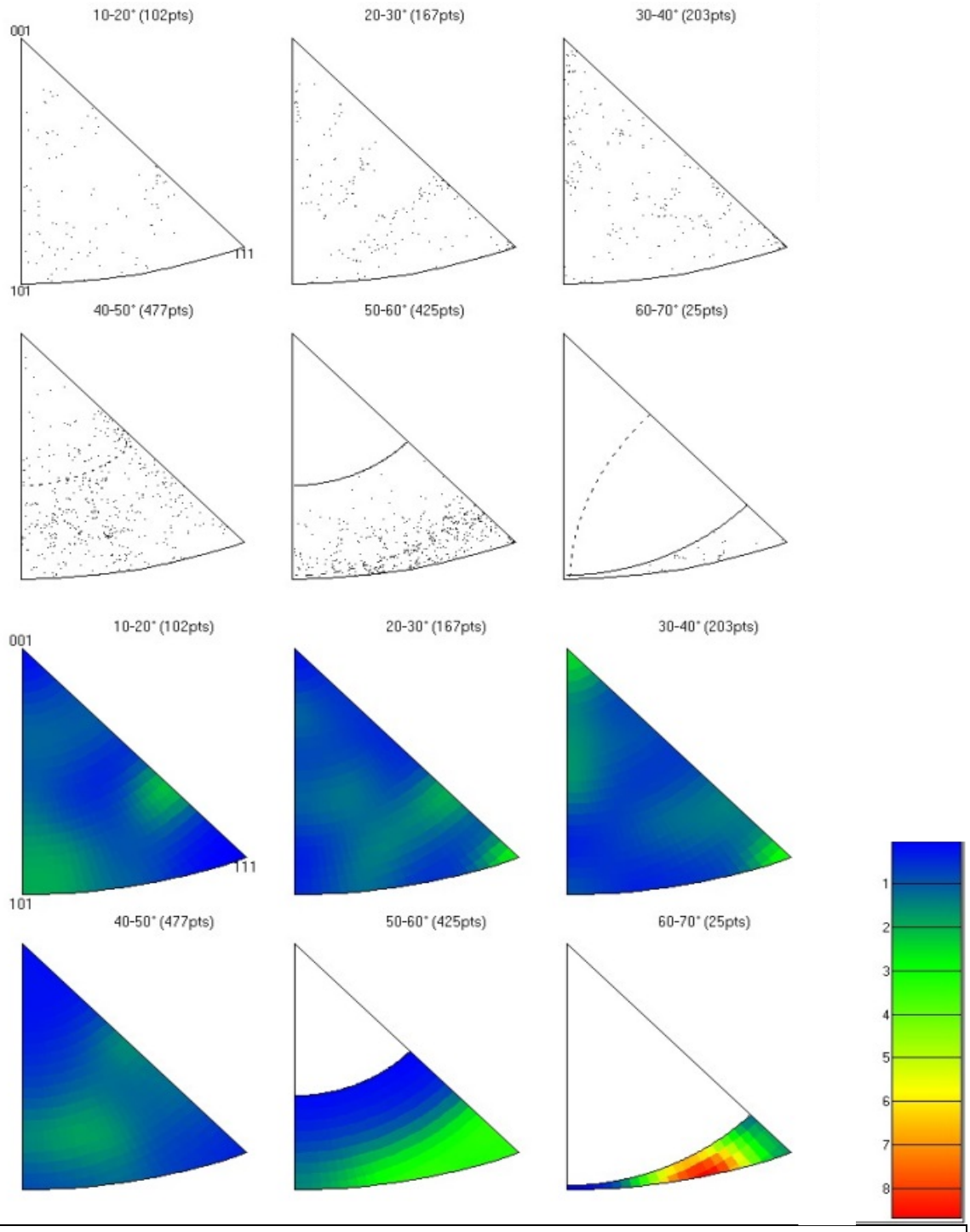

Figure 79. The misorientation density (black dots) as a function of orientation, and amount for a perpendicular cut coupon is seen in the left image. The right image shows the density of these points as a gradient with red corresponding to high density while blue corresponds to low density.

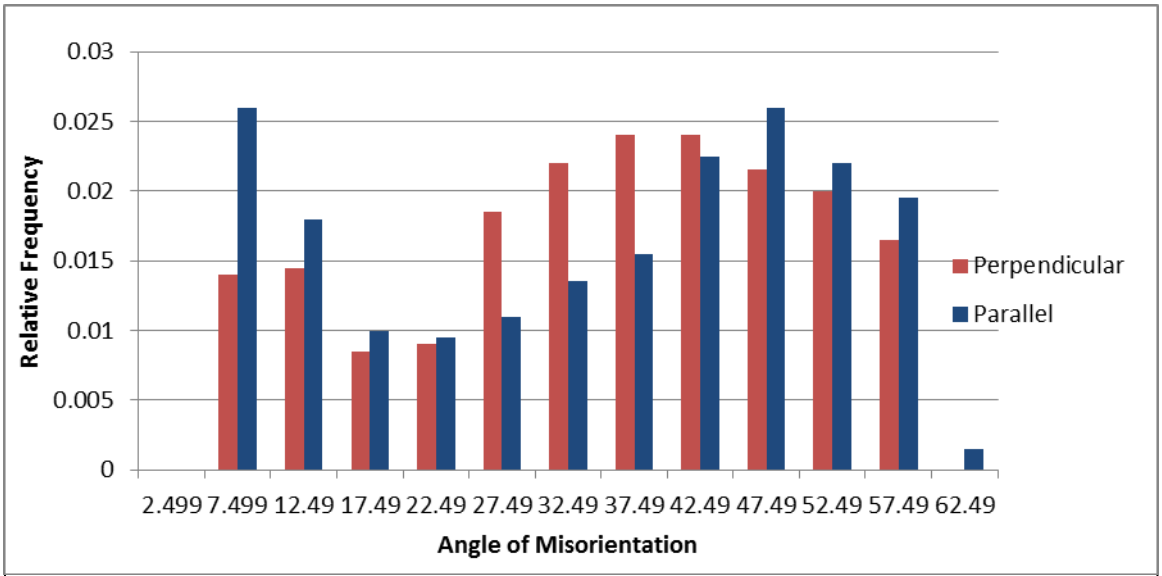

Figure 80. The plot shows the average misorientation from multiple locations for a parallel cut coupon and a perpendicular cut coupon.

The misorientation distribution shown for the parallel cut coupon in Figure 80 shows a higher average misorientation angle frequency compared to that of the perpendicular cut coupon. This means that the overall average change in orientation, i.e. texture, is higher for the parallel coupon than for the perpendicular coupon. Local misorientation (strain) histograms shown in Figure 81 show a similar trend. For the perpendicular cut coupon there is a sharp peak around 1.5 degrees of local misorientation. For the parallel cut coupon there is a broader peak centered around 2.1 degrees of local misorientation. There is also a higher relative frequency of points for local misorientation values for the parallel cut coupon. Applying this information to the mechanochemical concepts for strain, it is reasonable to infer from this information that the coupons cut parallel to the rolling direction would likely have a tendency to undergo more rapid anodic dissolution, and ultimately corrosion at a quicker rate.

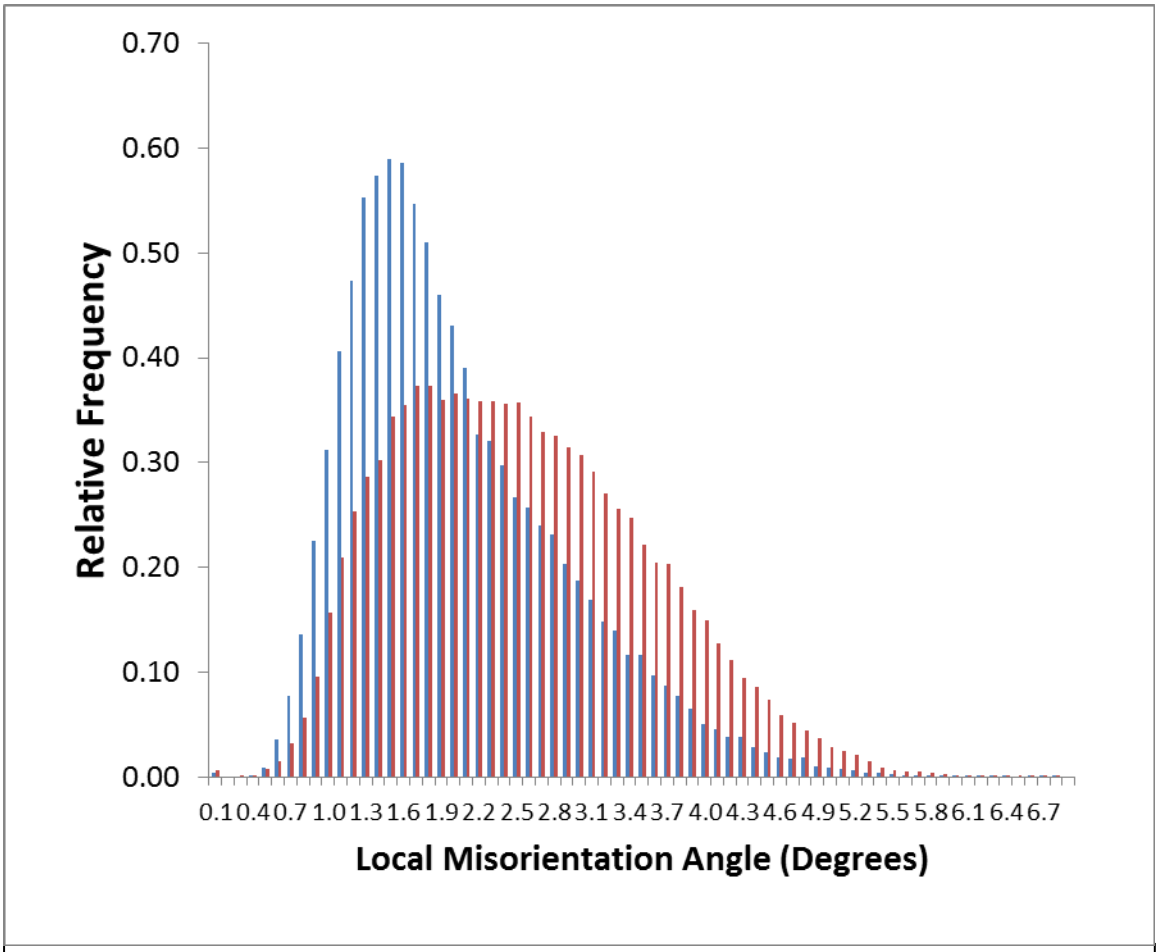

Figure 81. Local misorientation histograms taken from EBSD data for a parallel cut coupon (red) and a perpendicular cut coupon (blue) at the same magnification.

Taking the average of the two data sets yields a mean value of approximately 1.9 degrees misorientation for the perpendicular cut coupon, and 2.5 degrees for the parallel cut coupon. Using mechanochemical analysis, the change in anodic dissolution rate for the two coupons would yield a higher dissolution rate of the iron for the parallel cut coupon when compared to the perpendicular cut coupon under identical environmental

conditions. This is confirmed[40] by mass loss measurements taken for several of the experiments presented in this thesis. Although the direct microscopic correlation for the two coupons is often hard to achieve when corrosion rates are low, such as in the corrosion due to purely anaerobic indonesiensis culture, as well as the Biyotrapped indonesiensis experiment, the overlying average strain of the two types of coupons correlates to their macroscopic corrosion rates. It is, however, worth mentioning here that even though general corrosion is higher in the parallel cut coupons corrosion on perpendicular cut coupons is still dangerous in that localized corrosion in the immediate surroundings of MnS stringers lead to serious pits developing and growing around the stringers which go deeper into the carbon steel metal.

SUMMARY

The results of this study demonstrate the link between localized plastic deformation of the iron crystalline lattice and the increased rate of corrosion that occurs at these locations when exposed to corrosive environments containing mixed cultures of aerobic and anaerobic species in a sub-oxic sulfidogenic environment in the presence of fuel/seawater interfaces.

Results from systems containing three levels of oxygen concentrations including strictly anaerobic, sub-oxic, and with oxygen diffusing continuously into the system all revealed a correlation between residual strain and accelerated corrosion. Experiments performed in the presence of oxygen showed drastically greater corrosion of the 1018 steel coupons supported by electrochemical measurements, mass loss data, and by comparison of AFM surface analysis taken before and after corrosion.

Mechanochemical theories were used as a tool to provide a means of predicting the surface topography of the sample based on lattice deformation. These theories often predicted values for surface measurements within 30% error or better when compared to measured depths obtained from AFM analysis. An important result obtained from use of these equations was their consistency in predicting general corrosion rates despite the varying initial corrosion rates obtained during the study. For example, electrochemical values obtained for purely anaerobic experiments revealed much lower corrosion rates than for experiments with higher oxygen concentrations present. The predicted mechanochemical corrosion rates were based on the

electrochemical results from the actual environments, and therefore correlated to the changes in measured values. Higher measured electrochemical corrosion rates resulted in higher predicted mechanochemical corrosion rates. These results correlated to AFM measurements that also indicated higher corrosion rates for these circumstances. The opposite was also true; when electrochemical measurements gave results indicating low corrosion rates, predicted mechanochemical corrosion rates due to strain were also lower, which were further confirmed by AFM surface analysis.

Visual analysis of the areas of increased plastic deformation are also characterized by the presence of carbides, either in band form as seen in the parallel cut coupons, or in globular form as seen in the perpendicular cut coupons. Past work has shown an increase of the iron dissolution in these regions as primarily due to the galvanic effect between the highly-strained ferrite in between pearlite lamellar banded interfaced with cementite layers and the bulk iron that is not strained[51]. Increasing strain has been demonstrated in areas surrounding the pearlite microstructure in carbon steel, and it is believed that there is an increase in strain between the ferrite phase and the cementite phase in lamellar layers of pearlite structures[52,53]. The buildup of strain around hard precipitates during cold working is not exclusively limited to steel. Wilkinson has demonstrated the increase of strain in the areas directly surrounding carbides in other materials as well[54].

Although the evidence shown on these experiments does not directly dispute the idea of galvanic acceleration of iron dissolution, it does provide evidence towards

the concept that strain accelerated dissolution of steel near carbides is likely due to galvanic coupling between the strained and unstrained ferrite distributed throughout the steel.

CONCLUSIONS

The primary objective of this thesis was to determine the role that the metallurgical history of carbon steel plays in its rate of corrosion. This objective was achieved successfully through careful design of experiments conducted on carefully cut and polished carbon steel 1018 surfaces. We have demonstrated experimentally, and supported with model calculations that those areas of carbon steel that are strained (residual strain) during its metallurgical preparation corrode at a higher rate than those that are not strained. This conclusion was supported experimentally regardless of the environment that the coupons were subjected to: be it a strictly anaerobic, or suboxic or microbially influenced corrosive environment. The great advantage of this conclusion is that one can in principle predict where the most rapid corrosion is going to occur ahead of time. Through advancements in electron backscatter spectroscopy (EBSD) it is now possible to map out the strained areas of a polished carbon steel surface before subjecting it to a corrosive environment. It turns out that what makes carbon steel hard and strong also makes it more prone to corrosion. It is the pearlite phases of carbon steel that gives the steel its strength thanks to the lamellar cementite (Fe_3C) phases interspaced with the ferrite bands forming the pearlite phase which are disturbed throughout whole volume of the steel. Because of the lattice mismatch between the bcc cubic of ferrite and orthorhombic structure of cementite there are vast amount of cementite/ferrite interfaces which are severely strained and distributed throughout the carbon steel after cold rolling. These strains shift the corrosion potential of these ferrite

areas to a more active potential through $\Delta\varphi = -\frac{TR}{nF}\ln\left(\frac{\nu\alpha}{N_o}\varepsilon_p+1\right)$ where ε_p is the strain introduced due to dislocations and lattice mismatch.

Another important impurity in the iron matrix is the MnS stringers: Immediate surroundings of these stringers affect the surrounding ferrite matrix due to lattice mismatch, dislocations, surface tension and other interfacial surface tensions generating residual strain in these surroundings. Hence, these areas, too, become more anodic relative to the rest of the unstrained Fe matrix. The importance of these inclusions in corrosion is that when MnS dissolves in the acidic environments it produces abiotic H_2S which fuels the cathodic processes without the need of SRBs. This then accelerates the corrosion in these areas causing initiation and propagation of the pits.

The presence of strain distributed throughout the Fe suggests a revised view of corrosion. One can imagine a network of micro-galvanic cells distributed throughout the Fe matrix and the strained parts of Fe, such as ferrite layers in pearlite phases, acting as sacrificial anodes. In a corrosive environment these micro-galvanic cells fuel the overall corrosion process. This process cannot be stopped unless the strains are alleviated through further metallurgical processing.

A second important conclusion that can be drawn from our observations is that a strictly anaerobic corrosion process is self-limiting, in that a thin and hard protective layer of Fe sulfide forms on the surface initially and this prevents the anodic and cathodic processes, hence stopping or reducing the rate of the corrosion process. However, the presence of trace amount of O_2 in solution disrupts the formation of this

protective layer. Once this happens the corrosion will continue as long as sulfide is present in solution there is no other mechanisms that will limit the anodic and cathodic processes. If the corrosive medium also has some trace O_2 in solution, creating a suboxic/sulfidogenic environment, then a complicated corrosion process aided by hydrogen evolution and oxygen reduction develops. These promote the cathodic processes, while at the same time increasing the corrosion rates, causing deposition of a complex sulfides and oxides on the surface. Regardless of the MIC environment, the underlying strain-induced galvanic processes distributed at the microscopic scale throughout the metal matrix drives the corrosion process until either the anodic or cathodic processes are stopped. This view of corrosion is the most important discovery of this thesis.

As a final remark, I would just like to emphasize that the research presented in this thesis has major implications for the way in which we move forward in approaching the study of corrosion. It is not only the macroscopic characteristics of a material, as well as the environment that the material is exposed to, but also the microscopic characteristics that drive the macroscopic processes. As technology advances, and better analysis techniques continue to increase the resolution of our analysis equipment, a better understanding of exactly how strain influences corrosion down to the atomic level will become clear. This thesis bridges the gap between macroscopic and microscopic corrosion, a major leap that was only possible through the use of EBSD, and

AFM. I hope that it will act as a foundation to further the advancement of materials analysis, and ultimately to help in the continuous and costly fight against corrosion.

REFERENCES CITED

1. Hamilton, W. A., <Sulphate reducing bacteria and anaerobic corrosion.pdf>. *Ann. Rev. Microbiol.* **1985,** *39*, 195-217.

2. Suflita, J. M.; Aktas, D. F.; Oldham, A. L.; Perez-Ibarra, B. M.; Duncan, K., Molecular tools to track bacteria responsible for fuel deterioration and microbiologically influenced corrosion. *Biofouling* **2012,** *28* (9), 1003-1010.

3. Aktas, D. F.; Lee, J. S.; Little, B. J.; Ray, R. I.; Davidova, I. A.; Lyles, C. N.; Suflita, J. M., Anaerobic Metabolism of Biodiesel and Its Impact on Metal Corrosion. *Energ Fuel* **2010,** *24*, 2924-2928.

4. Galvan-Martinez, R.; Garcia-Caloca, G.; Duran-Romero, R.; Torres-Sanchez, R.; Mendoza-Flores, J.; Genesca, J., Comparison of electrochemical techniques during the corrosion of X52 pipeline steel in the presence of sulfate reducing bacteria (SRB). *Mater. Corros.* **2005,** *56* (10), 678-684.

5. McCafferty, E., *Introduction to Corrosion Science*. Springer Science Business Media: New York, NY 2010.

6. Lewandowski, Z.; Beyenal, H., Mechanisms of Microbially Influenced Corrosion. In *Marine and Industrial Biofouling*, Flemming, H.-C.; Murthy, P. S.; Venkatesan, R.; Cooksey, K., Eds. Springer Berlin Heidelberg: 2009; Vol. 4, pp 35-64.

7. Tester J.W. , M. M., *Thermodynamics and its Applications 3rd. Ed*. Prentice Hall: Upper Saddle River, New Jersey, 1997.

8. Lee, W.; Lewandowski, Z.; Nielsen, P. H.; Hamilton, W. A., Role of sulfate-reducing bacteria in corrosion of mild steel: A review. *Biofouling* **1995,** *8* (3), 165-194.

9. Videla, H., An overview of mechanisms by which sulphate-reducing bacteria influence corrosion of steel in marine environments. *Biofouling* **2000,** *15*, 37-47.

10. Videla , H., *Manual of Biocorrosion*. CRC Press, Inc.: Boca Raton, Florida, 1996.

11. Horvath, J.; Novak, M., Contributions to Mechanism of Anaerobic Microbiological Corrosion .2. Correlations between Ph Values, Oxidation Reduction Potentials and Composition of Solid Corrosion Products. *Acta Chim Hung* **1962,** *33* (2), 221-&.

12. Hamilton, W. A., Sulfate-Reducing Bacteria and Anaerobic Corrosion. *Annu Rev Microbiol* **1985,** *39*, 195-217.

13. Hamilton, W. A., Microbially influenced corrosion as a model system for the study of metal microbe interactions: A unifying electron transfer hypothesis. *Biofouling* **2003,** *19* (1), 65-76.

14. Dinh, H. T.; Kuever, J.; Mussmann, M.; Hassel, A. W.; Stratmann, M.; Widdel, F., Iron corrosion by novel anaerobic microorganisms. *Nature* **2004,** *427* (6977), 829-832.

15. Melchers, R., Pitting Corrosion of Mild Steel under Marine Anaerobic Conditions—Part 1: Experimental Observations. *Corrosion Science* **2006,** *62*, 981.

16. Krawiec, H.; Vignal, V.; Oltra, R., Use of the electrochemical microcell technique and the SVET for monitoring pitting corrosion at MnS inclusions. *Electrochem. Commun.* **2004,** *6* (7), 655-660.

17. Schmuki, P.; Hildebrand, H.; Friedrich, A.; Virtanen, S., The composition of the boundary region of MnS inclusions in stainless steel and its relevance in triggering pitting corrosion. *Corrosion Science* **2005,** *47* (5), 1239-1250.

18. Vignal, V.; Ba, D.; Zhang, H.; Herbst, F.; Le Manchet, S., Influence of the grain orientation spread on the pitting corrosion resistance of duplex stainless steels using electron backscatter diffraction and critical pitting temperature test at the microscale. *Corrosion Science* **2013,** *68*, 275-278.

19. Kunikova, T.; Wendrock, H.; Wetzig, K.; Hrivnakova, D., EBSD investigation of intergranular corrosion attack on low interstitial stainless steel. *Mater. Corros.* **2004,** *55* (6), 437-443.

20. Kelly, R. G., *Electrochemical Techniques in Corrosion Science and Engineering*. Marcel Dekker, Inc: New York, 2003.

21. Ning, J., A Thermodynamic Study of Hydrogen Sulfide Corrosion of Mild Steel. In *Nace International Corrosion Conference & Expo 2013*, 2013.

22. Kiss, L., *Kinetics of Electrochemical Metal Dissolution*. Elsevier Science Publishing Company Inc.: New York, NY 1988.

23. Brett, C. a. B., M, *Electrochemistry Principles, Methods, And Applications*. Ocford University Press: New York, 1993.

24. Hoar, T. P., mechano-chemical anodic dissolution *Nature* **1958**, 835.

25. K, H., Novel Technique for Measuring the Mechanochemical Anodic Dissolution of Metallic Electrodes in Aqueous Solutions. *SPIE-Practical Holography* **1990,** *1212*, 357-371.

26. Hoar, T. P., Mechano-Chemical Anodic Dissolution of Austenitic Stainless Steel in Hot Chloride Solution. *Proceedings of the Royal Society of London. Series A, Mathematical and Physical Sciences* **1962,** *268*, 304-315.

27. Gutman, E., Thermodynamics of the Mechanico-Chemical Effect. *Fiziko-Khimicheskaya Mekhanika Materialov* **1967,** *3*, 264-272.

28. Johnston, W. G., *J Appl Phys* **1962,** *33* (9).

29. Weismann, A. S. K. a. S., . *Proceeding of the Conf. on Electron Microscopy and Strength of Materials* **1963.,** *Interscience Publishers Inc., N.Y. 231*.

30. Gutman, E., *Mechanochemistry of Materials*. Cambridge International Science Publishing: Cambridge, UK, 1998; p 211.

31. Xu, L. Y.; Cheng, Y. F., Development of a finite element model for simulation and prediction of mechanoelectrochemical effect of pipeline corrosion. *Corrosion Science* **2013,** *73*, 150-160.

32. Arafin, M. A.; Szpunar, J. A., A new understanding of intergranular stress corrosion cracking resistance of pipeline steel through grain boundary character and crystallographic texture studies. *Corrosion Science* **2009,** *51* (1), 119-128.

33. Zhang, G. A.; Cheng, Y. F., Micro-electrochemical characterization of corrosion of pre-cracked X70 pipeline steel in a concentrated carbonate/bicarbonate solution. *Corrosion Science* **2010,** *52* (3), 960-968.

34. Tang, X.; Cheng, Y. F., Micro-electrochemical characterization of the effect of applied stress on local anodic dissolution behavior of pipeline steel under near-neutral pH condition. *Electrochimica Acta* **2009,** *54* (5), 1499-1505.

35. Nishikawa, S.; Kikuchi, S., Diffraction of cathode rays by mica. *Nature* **1928,** *121*, 1019-1020.

36. Callister, W. D., *Materials Scuebce abd Engineering an Introduction*. Wiley Hoboken, NJ, 2010.

37. Wilkinson, A. J., Methods for determining elastic strains from electron backscatter diffraction and electron channelling patterns. *Materials Science and Technology* **1997,** *13* (1), 79-84.

38. Wilkinson, A. J.; Clarke, E. E.; Britton, T. B.; Littlewood, P.; Karamched, P. S., High-resolution electron backscatter diffraction: an emerging tool for studying local deformation. *J Strain Anal Eng* **2010,** *45* (5), 365-376.

39. Ben Britton, T.; Jiang, J.; Karamched, P. S.; Wilkinson, A. J., Probing Deformation and Revealing Microstructural Mechanisms with Cross-Correlation-Based, High-Resolution Electron Backscatter Diffraction. *Jom-Us* **2013,** *65* (9), 1245-1253.

40. Kamaya, M., Measurement of local plastic strain distribution of stainless steel by electron backscatter diffraction. *Mater Charact* **2009,** *60* (2), 125-132.

41. Xu, L. Y.; Cheng, Y. F., Corrosion of X100 pipeline steel under plastic strain in a neutral pH bicarbonate solution. *Corrosion Science* **2012,** *64*, 145-152.

42. Shintani, T.; Murata, Y., Evaluation of the dislocation density and dislocation character in cold rolled Type 304 steel determined by profile analysis of X-ray diffraction. *Acta Materialia* **2011,** *59* (11), 4314-4322.

43. Avci, R.; Davis, B. H.; Suo, Z.; Lucas, K.; Beech, I. B.; Sunner, J. A.; Hammond, J.; Paul, D., Initiation of nanopits at MnS nano-inclusions on carbon steel exposed to anaerobic sulfate-reducing bacterium Desulfoglaeba alkanexedens. *Microscopy and microanalysis : the official journal of Microscopy Society of America, Microbeam Analysis Society, Microscopical Society of Canada* **2012,** *18 Suppl 2*, 4-5.

44. Avci, R.; Davis, B. H.; Wolfenden, M. L.; Beech, I. B.; Lucas, K.; Paul, D., Mechanism of MnS-mediated pit initiation and propagation in carbon steel in an anaerobic sulfidogenic media. *Corrosion Science* **2013,** *76*, 267-274.

45. Melchers, R. E., Pitting corrosion of mild steel under marine anaerobic conditions - Part 1: Experimental observations. *Corrosion* **2006,** *62* (11), 981-988.

46. Houyi, M., The influence of hydrogen sulfied on corrosion of iron under different conditions. *Corrosion Science* **1999,** *42*.

47. Kuang, F.; Wang, J.; Yan, L.; Zhang, D., Effects of sulfate-reducing bacteria on the corrosion behavior of carbon steel. *Electrochimica Acta* **2007,** *52* (20), 6084-6088.

48. Cetin, D.; Aksu, M. L., Corrosion behavior of low-alloy steel in the presence of Desulfotomaculum sp. *Corrosion Science* **2009,** *51* (8), 1584-1588.

49. R.C., N., The Electrochemistry of SRB Corrosion and Related Inorganic Phenomena. *ISIJ International* **1991,** *31*.

50. *Concise Encyclopedia of The Structure of Materials*. Elsevier: Oxford, UK, 2007.

51. Luo, J. H.; Xu, C. M., The Influence of Microstructures on the Corrosion Properties of X80 Pipeline Steel in Near-Neutral pH Soil. *New Materials and Processes, Pts 1-3* **2012,** *476-478*, 212-217.

52. Ohashi, T.; Roslan, L.; Takahashi, K.; Shimokawa, T.; Tanaka, M.; Higashida, K., A multiscale approach for the deformation mechanism in pearlite microstructure: Numerical evaluation of elasto-plastic deformation in fine lamellar structures. *Mat Sci Eng a-Struct* **2013,** *588*, 214-220.

53. Tanaka, M.; Yoshimi, Y.; Higashida, K.; Shimokawa, T.; Ohashi, T., A multiscale approach for the deformation mechanism in pearlite microstructure: Experimental measurements of strain distribution using a novel technique of precision markers. *Mat Sci Eng a-Struct* **2014,** *590*, 37-43.

54. Karamched, P. S.; Wilkinson, A. J., High resolution electron back-scatter diffraction analysis of thermally and mechanically induced strains near carbide inclusions in a superalloy. *Acta Materialia* **2011,** *59* (1), 263-272.

APPENDICES

APPENDIX A

MATLAB FILES USED FOR MECHANOCHEMICAL AND ELECTROCHEMICAL CALCULATIONS

StrainedMarIndo.m

```
clc, clear
% To Obtain the size of the image to be calculated
box_title = 'Enter the Step Size of your map';
entries = { 'microns'};
z = inputdlg(entries, box_title);
n = str2num(z{1});
[filename] = ...
    uigetfile({'*.*'},'Select The EBSD Local Misorientation File');
figure
imshow(filename);
box_title2 = 'Enter the Time of Exposure (days)';
entries2 = { 'Days'};
z2 = inputdlg(entries2, box_title2);
Time = str2num(z2{1});
pl=imread(filename);
x=im2uint16(pl); %Image to 16 bit for better analysis
xgray=rgb2gray(x); %Convert to grayscale to eliminate descrepenceies
   %of contributing RGB content
st=imresize(xgray,[300 300]);
ST=im2double(st);
figure
imshow(ST);
STR=flipud(ST);
%applying a scaling factor to convert image data into local misorientation
%degree
misorientation=40.*STR;
misorientation(misorientation>6)=6;%the maximum misorientation value given on the
map is 6 degrees at grain boundaries
%plotting the data
figure
surf(misorientation,'Edgecolor','none')
colormap jet
colorbar
title('Local Misorientation Angle (Degrees')
%Calculating local strain according to Kamaya paper where epsilon=Q/W
Q=misorientation-.1;
W=(-.0027*(n^2))+(.041*n);%n=stepsize
%Percent Local Strain
eppercent=Q./W;
%local plastic strain (similar to that in Cheng Paper)
epsilon=eppercent./100;
```

```
T=300;%temperature
R=8.314;%gas constant
v=.45;% from the cheng paper
alpha=1.402*10^11;
zz=2;%atomic charge
F=96485;%faradays constant
No=1.078*10^10;%dislocation density of bulk
p=-(T*R)/(zz*F);
po=((epsilon.*(v*alpha/No))+1);
pota = po - min(0.000001, min(po(:))); %Setting all negative strain values to 0
pot=log(pota);%Equation 6 Cheng Corrosion of x100 steel
potentialchange=p.*pot;%the change in potential as a function of plastic strain
potentialchangeinv=(potentialchange);
figure
subplot(211),
surf(potentialchange,'Edgecolor','none')
colorbar;
title('Change in Anodic Equilibrium Potential')
subplot(212),imagesc(potentialchange)
axis xy
title('Change in Anodic Equilibrium Potential')
b=0.060; %Tafel slope (Volts/decade) of steel from Polarization Resistance (69.7mv)
iao=3.354*10^-6; %corrosion rate of unstressed steel cm2/s Anodic Oxidation from tafel
slope
potentialchangeabs=abs(potentialchange); %Absolute value of potential change, which
is the same as
   %saying nu=phi-(-delphieq)=phi+phieq=|delphieq|
q=potentialchangeabs./b;% Eqn 4 Cheng
I=iao*exp((q));%Current density as a function of strain eqn 4 cheng
delI=I; %Change in current density
figure
subplot(211),
surf(delI,'Edgecolor','none')
colorbar
title('Change in Current Density (A/cm2)')
subplot(212),imagesc(delI)
axis xy
title('Change in Current Density (A/cm2)')
%Converting to mm/yr
AtomicMassFe=55.845;
DensityFe=7.87;
delImm=delI.*(3.27*AtomicMassFe/(zz*DensityFe))*1000;%mmYr using K from ASTM
```

```
figure
subplot(211),
surf(delImm,'Edgecolor','none');
colorbar
subplot(212),imagesc(delImm)
axis xy
colorbar
title('Change in Corrosion Rate (mm/yr)')
%converting to Meters/yr
AFMsurface=1-((delImm)./1000);%Predicted Plot of AFM surface after 1 yr (meters)
figure
subplot(211),
surf(AFMsurface,'Edgecolor','none');
colorbar
title('Predicted AFM Surface Topography After 1 Year (meters)');
subplot(212),
imagesc(AFMsurface)
axis xy
colorbar
%Adjusting for Exposure time of 14 Days
exposure=Time/365;
ExposureAFM=(AFMsurface.*exposure);
figure
surf(ExposureAFM,'Edgecolor','none')
colorbar
title('AFM Surface Prediction After Exposure Time (meters)')
delIratio=delI./iao;

figure
subplot(211),
surf(delIratio,'Edgecolor','none')
colorbar
title('Ratio of Current Density to Initial Current Density')
subplot(212),imagesc(delI)
axis xy
title('Ratio of Current Density to Initial Current Density')


% OPTIONAL
% df=ExposureAFM.*10^6;%Converting Meters to Microns
% depth=(df);
% figure
```

```
% plot(depth(:,70))
% [x4,y4]=ginput(6);
% title('Surface Topography Along Line')
% % depth=interp2(AFMsurface)
% changeindepth1=y4(2)-y4(1);
% disp('The change in depth in microns of your at the first location is ')
% disp(changeindepth1);
% changeindepth2=y4(4)-y4(3);
% disp('The change in depth in microns of your at the second location is ')
% disp(changeindepth2);
% changeindepth3=y4(6)-y4(5);
% disp('The change in depth in microns of your at the third location is ')
% disp(changeindepth3);

figure
imshow(ExposureAFM)
df=improfile.*10^6;%Converting Meters to Microns
depth=(df);
figure
plot(depth)
[x4,y4,]=ginput(2);
title('Surface Topography Along Line')
% depth=interp2(AFMsurface)
changeindepth=y4(2)-y4(1);
disp('The change in depth in microns of your surface along the line you chose is ')
disp(changeindepth);
```

Strained.m

```
clc, clear
% To Obtain the size of the image to be calculated
box_title = 'Enter the Step Size of your map';
entries = { 'microns'};
z = inputdlg(entries, box_title);
n = str2num(z{1});
[filename] = ...
    uigetfile({'*.*'},'Select The EBSD Local Misorientation File');
figure
imshow(filename);
box_title2 = 'Enter the Time of Exposure (days)';
entries2 = { 'Days'};
z2 = inputdlg(entries2, box_title2);
Time = str2num(z2{1});

pl=imread(filename);
x=im2uint16(pl); %Image to 16 bit for better analysis
xgray=rgb2gray(x); %Convert to grayscale to eliminate descrepenceies
   %of contributing RGB content
st=imresize(xgray,[219 219]);
ST=im2double(st);
figure
imshow(ST);
STR=flipud(ST);
%applying a scaling factor to convert image data into local misorientation
%degree
misorientation=40.*STR;
misorientation(misorientation>6)=6;%the maximum misorientation value given on the
map is 6 degrees at grain boundaries
%plotting the data
figure
surf(misorientation,'Edgecolor','none')
colormap jet
colorbar
title('Local Misorientation Angle (Degrees')
%Calculating local strain according to Kamaya paper where epsilon=Q/W
Q=misorientation-.1;
W=(-.0027*(n^2))+(.041*n);%n=stepsize
%Percent Local Strain
eppercent=Q./W;
```

```
%local plastic strain (similar to that in Cheng Paper)
epsilon=eppercent./100;
T=300;%temperature
R=8.314;%gas constant
v=.45;% from the cheng paper
alpha=1.402*10^11;
zz=2;%atomic charge
F=96485;%faradays constant
No=1.078*10^10;%dislocation density of bulk
p=-(T*R)/(zz*F);
po=((epsilon.*(v*alpha/No))+1);
pota = po - min(0.000001, min(po(:))); %Setting all negative strain values to 0
pot=log(pota);%Equation 6 Cheng Corrosion of x100 steel
potentialchange=p.*pot;%the change in potential as a function of plastic strain
potentialchangeinv=(potentialchange);
figure
subplot(211),
surf(potentialchange,'Edgecolor','none')
colorbar;
title('Change in Anodic Equilibrium Potential')
subplot(212),imagesc(potentialchange)
axis xy
title('Change in Anodic Equilibrium Potential')
b=0.06; %(mv)
iao=1.602*10^-6; %corrosion rate of bulk steel cm2/s Anodic Oxidation from tafel slope
potentialchangeabs=abs(potentialchange); %Absolute value of potential change, which
is the same as
   %saying nu=phi-(-delphieq)=phi+phieq=|delphieq|
q=potentialchangeabs./b;% Eqn 4 Cheng
I=iao*exp((q));%Current density as a function of strain eqn 4 cheng
delI=I; %Change in current density
delIratio=delI./iao;
figure
subplot(211),
surf(delIratio,'Edgecolor','none')
colorbar
title('Ratio of Current Density to Initial Current Density')
subplot(212),imagesc(delI)
axis xy
title('Ratio of Current Density to Initial Current Density')

figure
```

```
subplot(211),
surf(delI,'Edgecolor','none')
colorbar
title('Change in Current Density (A/cm2)')
subplot(212),imagesc(delI)
axis xy
title('Change in Current Density (A/cm2)')

%Converting to mm/yr
AtomicMassFe=55.845;
DensityFe=7.87;
delImm=delI.*(3.27*AtomicMassFe/(zz*DensityFe))*1000;%mmYr using K from ASTM
figure
subplot(211),
surf(delImm,'Edgecolor','none');
colorbar
subplot(212),imagesc(delImm)
axis xy
colorbar
title('Change in Corrosion Rate (mm/yr)')

%converting to Meters/yr
AFMsurface=1-((delImm)./1000);%Predicted Plot of AFM surface after 1 yr (meters)
figure
subplot(211),
surf(AFMsurface,'Edgecolor','none');
colorbar
title('Predicted AFM Surface Topography After 1 Year (meters)');
subplot(212),
imagesc(AFMsurface)
axis xy
colorbar

%Adjusting for Exposure time of 14 Days
exposure=Time/365;
ExposureAFM=(AFMsurface.*exposure);
figure
surf(ExposureAFM,'Edgecolor','none')
colormap autumn
colorbar
title('AFM Surface Prediction After Exposure Time (meters)')
```

```
df=ExposureAFM.*10^6;%Converting Meters to Microns
depth=(df);
figure
plot(depth(:,70))
[x4,y4]=ginput(8);
title('Surface Topography Along Line')
% depth=interp2(AFMsurface)
changeindepth1=y4(2)-y4(1);
disp('The change in depth in microns of your at the first location is ')
disp(changeindepth1);
changeindepth2=y4(4)-y4(3);
disp('The change in depth in microns of your at the second location is ')
disp(changeindepth2);
changeindepth3=y4(6)-y4(5);
disp('The change in depth in microns of your at the third location is ')
disp(changeindepth3);
changeindepth4=y4(8)-y4(7);
disp('The change in depth in microns of your at the third location is ')
disp(changeindepth4);

% OPTIONAL
% figure
% imshow(ExposureAFM)
% df=improfile.*10^6;%Converting Meters to Microns
% depth=(df);
% figure
% plot(depth)
% [x4,y4,]=ginput(2);
% title('Surface Topography Along Line')
% % depth=interp2(AFMsurface)
% changeindepth=y4(2)-y4(1);
% disp('The change in depth in microns of your surface along the line you chose is ')
% disp(changeindepth);


%calculating average strain
% figure
% surf(epsilon,'Edgecolor','none')
% imshow(epsilon)
% dt=improfile
% % plot(epsilon(:,70))
% strainer=(dt);
```

```
% plot(strainer)
% [x4,y4]=ginput(8);
% title('Surface Topography Along Line')
% % depth=interp2(AFMsurface)
% changeindepth1=y4(2)-y4(1);
% disp('The strain of your at the first location is ')
% disp(changeindepth1);
% % changeindepth2=y4(4)-y4(3);
% % disp('The strain of your at the second location is ')
% % disp(changeindepth2);
% % changeindepth3=y4(6)-y4(5);
% % disp('The strain of your at the third location is ')
% % disp(changeindepth3);
% % changeindepth4=y4(8)-y4(7);
% % disp('The strain of your at the third location is ')
% % disp(changeindepth4);
```

StrainedIndo.m

```
clc, clear
% To Obtain the size of the image to be calculated
box_title = 'Enter the Step Size of your map';
entries = { 'microns'};
z = inputdlg(entries, box_title);
n = str2num(z{1});
[filename] = ...
    uigetfile({'*.*'},'Select The EBSD Local Misorientation File');
figure
imshow(filename);
box_title2 = 'Enter the Time of Exposure (days)';
entries2 = { 'Days'};
z2 = inputdlg(entries2, box_title2);
Time = str2num(z2{1});

pl=imread(filename);
x=im2uint16(pl);
xgray=rgb2gray(x);
st=imresize(xgray,[219 219]);
ST=im2double(st);
figure
imshow(ST);
STR=flipud(ST);
%applying a scaling factor to convert image data into local misorientation
%degree
misorientation=40.*STR;
misorientation(misorientation>6)=6;%the maximum misorientation value given on the
map is 6 degrees at grain boundaries
%plotting the data
figure
surf(misorientation,'Edgecolor','none')
colormap jet
colorbar
title('Local Misorientation Angle (Degrees')
%Calculating local strain according to Kamaya paper where epsilon=Q/W
Q=misorientation-.1;
W=(-.0027*(n^2))+(.041*n);%n=stepsize
%Percent Local Strain
eppercent=Q./W;
%local plastic strain (similar to that in Cheng Paper)
epsilon=eppercent./100;
```

```
T=300;%temperature
R=8.314;%gas constant
v=.45;% from the cheng paper
alpha=1.402*10^11;%from the cheng paper
zz=2;%atomic charge
F=96485;%faradays
No=1.078*10^10;%dislocation density of bulk
p=-(T*R)/(zz*F);
po=((epsilon.*(v*alpha/No))+1);
pota = po - min(0.000001, min(po(:)));
pot=log(pota);
potentialchange=p.*pot;%the change in potential as a function of plastic strain
potentialchangeinv=(potentialchange);
figure
subplot(211),
surf(potentialchange,'Edgecolor','none')
colorbar;
title('Change in Anodic Equilibrium Potential')
subplot(212),imagesc(potentialchange)
axis xy
title('Change in Anodic Equilibrium Potential')
b=0.06 %Tafel slope of steel from Tafel Plot for Indo Culture
iao=1.687*10^(-6); %corrosion rate of unstressed steel cm2/s Anodic Oxidation from
tafel slope
potentialchangeabs=abs(potentialchange); %Absolute value of potential change
nu=potentialchangeabs./b;
I=iao*exp((nu));%Current density as a functino of strain
delI=I; %Change in current density
figure
subplot(211),
surf(delI,'Edgecolor','none')
colorbar
title('Change in Current Density (A/cm2)')
subplot(212),imagesc(delI)
axis xy
title('Change in Current Density (A/cm2)')
%Converting to mm/yr
AtomicMassFe=55.845;
DensityFe=7.87;
delImm=delI.*(3.28*AtomicMassFe/(zz*DensityFe))*1000;
figure
subplot(211),
```

```
surf(delImm,'Edgecolor','none');
colorbar
subplot(212),imagesc(delImm)
axis xy
colorbar
title('Change in Corrosion Rate (mm/yr)')

delIratio=delI./iao;

figure
subplot(211),
surf(delIratio,'Edgecolor','none')
colorbar
title('Ratio of Current Density to Initial Current Density')
subplot(212),imagesc(delI)
axis xy
title('Ratio of Current Density to Initial Current Density')

%converting to Meters/yr
AFMsurface=1-((delImm)./1000);%Predicted Plot of AFM surface after 1 yr (meters)
figure
subplot(211),
surf(AFMsurface,'Edgecolor','none');
colorbar
title('Predicted AFM Surface Topography After 1 Year (meters)');
subplot(212),
imagesc(AFMsurface)
axis xy
colorbar
%Adjusting for Exposure time of 14 Days
exposure=Time/365;
ExposureAFM=(AFMsurface.*exposure);
figure
surf(ExposureAFM,'Edgecolor','none')
colorbar
title('AFM Surface Prediction After Exposure Time (meters)')

% OPTIONAL
% df=ExposureAFM.*10^6;%Converting Meters to Microns
% depth=(df);
% figure
% plot(depth(:,70))
```

```
% [x4,y4]=ginput(6);
% title('Surface Topography Along Line')
% % depth=interp2(AFMsurface)
% changeindepth1=y4(2)-y4(1);
% disp('The change in depth in microns of your at the first location is ')
% disp(changeindepth1);
% changeindepth2=y4(4)-y4(3);
% disp('The change in depth in microns of your at the second location is ')
% disp(changeindepth2);
% changeindepth3=y4(6)-y4(5);
% disp('The change in depth in microns of your at the third location is ')
% disp(changeindepth3);

figure
imshow(ExposureAFM)
df=improfile.*10^6;%Converting Meters to Microns
depth=(df);
figure
plot(depth)
[x4,y4,]=ginput(2);
title('Surface Topography Along Line')
changeindepth=y4(2)-y4(1);
disp('The change in depth in microns of your surface along the line you chose is ')
disp(changeindepth);
```

ButlerVolmer.m

```
%This program will calculate the needed tafel slope and alpha values
%given the measured slope of the polarization resistance for the linear
%portion of the graph
clc, clear
ohms=input('Enter the Slope of the Linear Portion of the E vs. I Graph ');
A=input('Enter the Area of Your Sample (square centimeters) ');
k=3.272*10^-3; %Conversion constant provided by ASTMG102-89
Time=input('Enter the Time (days) of exposure');
c=(8.314*298)/(2*96846);
alpha=.5;
ba=0.118/2; % ba=2.303*((8.314*298)/(2*96846))*1/alpha
bc=ba;
B=((ba*bc)/(2.303*(ba+bc))); %The stern geary coefficient
io=(B./ohms);
disp('The tafel slope in v/decade is ')
disp(ba)
disp('The Stern-Geary Coefficient for this system is ')
disp(B)
disp('The corrosion current density of the system (A/cm^2) is ')
disp(io)
 MW=55.845; %Molecular weight of Iron
n=2; %Number of electrons transferred in the process
F=96486;
EW=MW/n; %Equivalent weight of Iron
rho=7.87; %Density of solid iron
icorr=io*10^6;%Converting to microamps
icorry=io*10000;%Converting to Amps/m2
CR=k*(icorr/rho)*EW;
disp('The corrosion rate in mmYr is ')
disp(CR)
disp('The mass (mg) loss after your exposure period at this rate is ')
Rater=io*EW/F;%g/cm2s
Rate=Rater*1000*2.4*(60*60*24*Time);
disp(Rate)
```

APPENDIX B

ADDITIONAL TABLES AND FIGURES

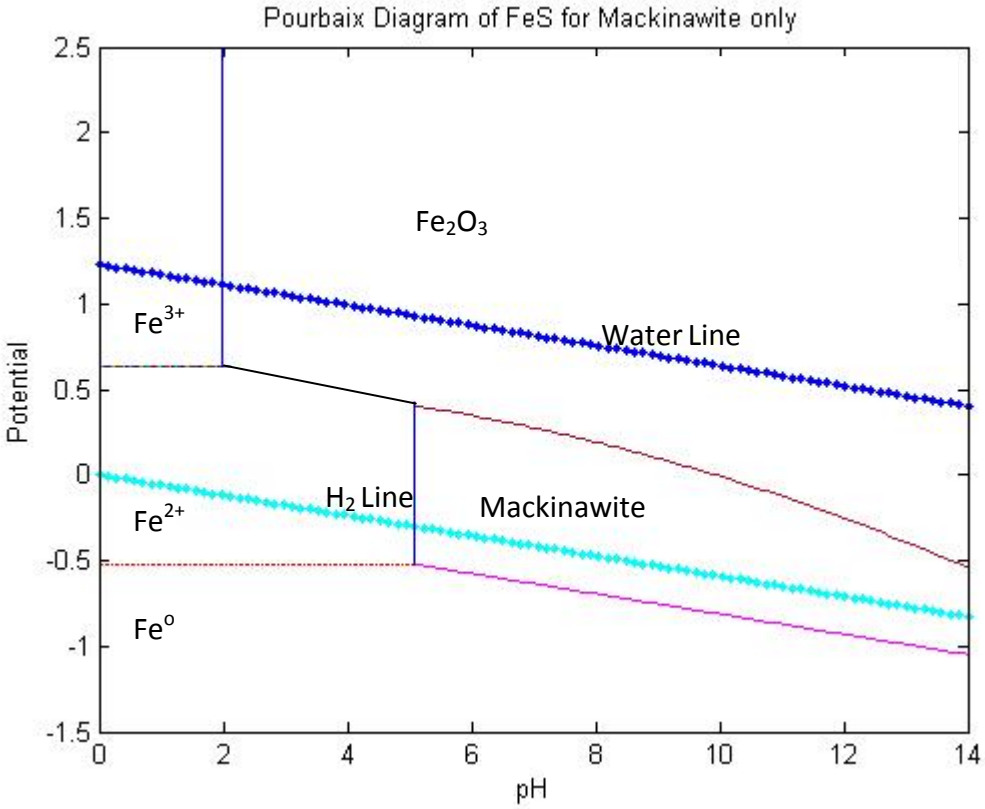

Appendix Figure 1. Pourbaix diagram of FeS for Mackinawite